Spin transfer torques in the heavy metal/ferromagnet/oxide hetero-structure Ta/CoFeB/MgO

Dissertation

zur Erlangung des Grades
"Doktor der Naturwissenschaften"
am Fachbereich Physik, Mathematik und Informatik
der Johannes Gutenberg-Universität
in Mainz

Tomek Schulz

geb. in Berlin (Germany)
Mainz, 2018

JOHANNES GUTENBERG
UNIVERSITÄT MAINZ

Tomek Schulz
AG Kläui
Institut für Physik
Staudingerweg 7
Johannes Gutenberg-Universität Mainz
D-55128 Mainz
Tomek.Schulz@gmail.com

Datum der Prüfung: 08.11.2018

Eidesstattliche Erklärung

Hiermit erkläre ich an Eides statt, dass ich meine Dissertation selbständig und ohne fremde Hilfe verfasst und keine anderen als die von mir angegebenen Quellen und Hilfsmittel zur Erstellung meiner Dissertation verwendet habe. Die Arbeit ist in vorliegender oder ähnlicher Form bei keiner anderen Prüfungsbehörde zur Erlangung eines Doktorgrades eingereicht worden.

Tomek Schulz

Abstract

Spin-orbit interaction based spin transfer torque promises ultra-efficient magnetization switching used for modern information storage devices based on emergent quasi-particles such as domain walls and skyrmions. Recently, spin structure dynamics, materials, and systems with tailored spin-orbit torques are being developed.

A method, which allows to detect the acting torques in a given system as a function of the magnetization direction is the torque magnetometry method, which is based on a higher harmonics analysis of the anomalous Hall effect.

So far it has not been shown that the spin-orbit torques measured with this torque magnetometry method for homogeneous spin-textures are consistent with results of effective collective torques acting on more complex spin-textures such, as domain walls and skyrmions.

In this thesis, we address this issue by measuring both the torques for homogeneous spin-textures with the torque magnetometry method, as well as the effective collective torques for domain walls within domain wall depinning experiments, on the same sample.

We show that the effective fields acting on magnetic domain walls that govern the efficiency of their dynamics require a sophisticated analysis taking into account the full angular dependence of the torques.

Using a one-dimensional model, we compare the spin-orbit torque efficiencies by depinning measurements and spin torque magnetometry.

We show that the effective fields can be accurately determined with both methods individually, but find good agreement only when first, one takes into account a geometrical conversion factor of $\pi/2$ and second, one neglects, that the measurement results for the domain wall depinning show the maximum torque efficiency in a direction not expected from the simple spin-orbit torque model.

However, our method allows us now to rapidly screen materials by using the fast torque magnetometry method and to predict the resulting quasi-particle dynamics. Finally, we discuss the validity of this approach and give recommendations on how to eliminate given uncertainties.

Zusammenfassung

Spin-Bahn Wechselwirkung basierte Spin-Drehmoment-Übertragung verspricht höchst-effiziente Schaltvorgänge der Magnetisierung für neuartige Datenspeichertechnologien zu ermöglichen, welche auf Quasiteilchen wie Domänenwänden und Skyrmionen basieren. Seit kurzem werden Spin-Strukturen, Materialien und Systeme mit maßgenschneiderten Spin-Bahn Drehmoment-Eigenschaften entwickelt.

Eine effektive Methode, die es erlaubt die wirkenden Drehmomente in einem gegebenen System als Funktion der Magnetisierungsrichtung zu messen, ist die sogenannte Drehmoment-Magnetometrie. Sie basiert auf einer Analyse der höheren Harmonischen des anormalen Hall-Effekts.

Bisher konnte noch nicht gezeigt werden, dass Spin-Bahn Drehmomente für homogene Spin-Strukturen, die mit der Methode der Drehmoment-Magnetometrie gemessen wurden auch mit den Ergebnissen der effektiven kollektiven Drehmomente, welche für kompliziertere Spin-Strukturen, wie Domänenwände oder Skymionen wirken, konsistent sind.

In dieser Arbeit beschäftigen wir uns mit dieser Frage und messen beide Größen an derselben Probe. Die Drehmomente für homogene Spin-Strukturen, gemessen mit der Drehmoment-Magnetometrie und die effektiven kollektiven Drehmomente für Domänenwände gemessen mit Hilfe von Domänenwand-Depinning Experimenten an einem Hall-Kreuz.

Wir zeigen, dass die effektiven Felder, welche auf die Domänenwände wirken und die Effizienz der Domänenwanddynamik bestimmen, eine winkelabhängige Betrachtung der Drehmomente benötigen.

Um die Spin-Bahn Drehmoment-Effizienzen von den Domänenwand-Depinning Messungen mit den Spin-Bahn Drehmomenten der Magnetometrie Messungen zu vergleichen, benutzen wir ein eindimensionales Model für die Domänenwand.

Wir können zeigen, dass die effektiven Felder zwar einzeln genau bestimmt werden können, eine gute Übereinstimmung allerdings nur gegeben ist, wenn man zum einen einen geometrischen Übersetzungs-Faktor von $\pi/2$ berücksichtigt und wir zusätzlich vernachlässigen, dass die maximale Drehmoment-Effizienz bei unseren Domänenwand-Depinning Messungen eine unerwartet gedrehte Richtungsabhängigkeit aufweist, die sich so nicht aus dem einfachen Spin-Bahn Wechselwirkung basierten Drehmoment-Übertrags-Modell ergeben würde.

Nichtsdestotrotz erlaubt uns unsere Methode in Zukunft Materialien schneller mit Hilfe der Drehmoment Magnetometrie zu vermessen und so die Quasi-Teilchen-Dynamik vorhersagen zu können, wenn auch bisher nur mit den genannten Einschränkungen.

Zuletzt geben wir noch Handlungsempfehlungen, wie man die Unsicherheit über die Gültigkeit unseres Ansatzes in zukünftigen Domänenwand Depinning Messungen beseitigen könnte.

Inhaltsverzeichnis

Abbreviations

2DEG	2 dimensional electron gas
AD	Anti-damping
AHE	Anomalous Hall effect
CIDWM	Current-induced domain wall motion
DFT	Density functional theory
DMI	Dzyaloshinskii-Moriya interaction
DW	Domain wall
EHE	Extraordinary Hall effect
EBL	Electron beam lithography
ESD	Electrostatic discharge
FM	Ferromagnet
FL	Field-like
GMR	Giant magneto resistance
HAMR	Heat assisted magnetic recording
HDD	Hard disk drive
HM	Heavy metal
IMA	In-plane magnetic anisotropy
ISGE	Inverse spin galvanic effect
ISHE	Inverse spin Hall effect
LLG	Landau-Lifshitz-Gilbert
NM	Non-magnetic
Oe	Oersted
OHE	Ordinary Hall effect
PHE	Planar Hall effect
PID	Proportional-integral-derivative
PMA	Perpendicular magnetic anisotropy
RAM	Random access memory
RTMD	Racetrack memory device
SEM	Scanning electron microscope
SGE	Spin galvanic effect
SHA	Spin Hall angle
SHE	Spin Hall effect

SIA	Structural inversion asymmetry
SIMS	Secondary ion mass spectroscopy
SO	Spin-orbit
SOC	Spin-orbit coupling
SOT	Spin-orbit torque
SQUID	Superconducting quantum interference device
SSD	Solid state drive
STT	Spin transfer torque
TEM	Lorentz-transmission electron microsope
TMR	Tunnel magneto resistance
VTI	Variable temperature insert

1 Introduction

1.1 Motivation

Today's increasing demand of computational power in all aspects of modern life catalysts the continuous development of novel concepts improving processing speed, storage capacity and the efficient use of energy and material resources.

The established storage device technologies on the consumer and professional market today are most prominently the hard disk drive (HDD), the random access memory (RAM) and more recently the solid state drive (SSD) (Fig. 1.1). Each of these technologies has their particular advantages, but also conceptual limitations, balancing the above mentioned aspects of device properties in a different way.

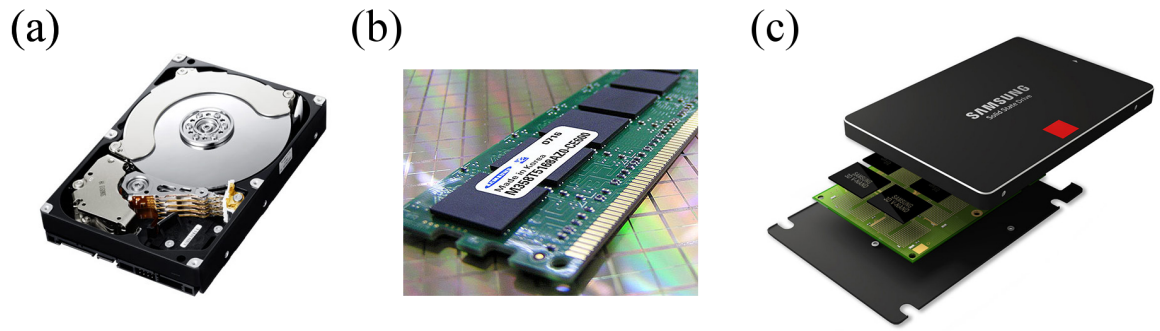

Abbildung 1.1: Today's established storage device technologies on the consumer market. (a) Magnetic hard disk drive (HDD), (b) dynamic random access memory (DRAM) and (c) solid state drive (SSD). (Pictures courtesy of Seagate and Samsung).

Advantages of the HDD are e.g. very large storage capacities in the order of TBytes per single device. In modern HDDs, which are using e.g. the giant magneto resistance (GMR) effect[1] and heat-assisted magnetic recording (HAMR), the storage capacities for a single device reach up to 20 TBytes[2] and can provide reliable retention of the data after the devices power is turned off. Hereby, the industry standard of the guaranteed retention time of stored data on a HDD is typically $\approx$ 10 years. However, best practice in magnetic disk systems indicate that data should be migrated between three to five years, since the failure rate of the devices considerably increases over time.[3]

Disadvantages of the HDD, compared to the other technologies, are e.g. its relatively slow information reading and writing times, which are typically in the order of a few milliseconds, a relatively high energy consumption (a few Watts/GB in the operating mode), and the generic sensitivity of the HDD device due to its mechanically moving parts. The combination of these

disadvantages together with the additional large size factor of a HDD (typically 2.5" or 3.5"), makes this technology for example inappropriate for modern mobile devices like smart phones, wearables or smart sensors, which are used e.g. in consumer electronics or in typical internet of things applications.

Controversially to the HDD, RAM for example, has much faster access times (in the range of sub-nanoseconds). It is therefore typically used as a cache memory operating in synchronization with the computers processing units, which operate typically at GHz frequency. Since information in a conventional RAM device is stored in the form of electrical charges inside of field-effect-transistors, leakage currents become increasingly relevant when the transistors size is shrunk down to a few nanometers[4]. For the gain of storage capacity this leads to the data volatility of transistor based RAM devices within a millisecond time-frame. In order to keep stored information in the fast operating RAM still available over time, it has to be continuously rewritten, even if the data is not needed for some time period. This is obviously not only very energy consumptive, but also a quite energy inefficient. Additionally, the price per GB RAM is still very high ($\approx$ 10 €/GB), which is because of the relatively complex nano-fabrication and manufacturing processes involved in the RAM production.

In the last decades several new RAM concepts have been proposed and are subject to intense research activities worldwide. Most of these new RAM concepts circumvent the volatility issue discussed above, while simultaneously achieving comparable speeds like static RAM (SRAM) and storage densities like dynamic RAM (DRAM). These new device concepts are e.g. the resistive RAM (RRAM) like phase-change (PC-RAM) or programmable metallization cell RAM (PMC-RAM), the ferroelectric RAM (FeRAM), magnetic RAM (MRAM) and spin-transfer torque RAM (STT-MRAM)[5]. In this thesis we focus on the development of magnetic RAM technology, more specifically on one particular device concept, which is called *racetrack memory device*[6] .

1.2 Racetrack memory device concept

The racetrack memory device (RTMD) was originally proposed in 2008 by S. Parkin et al.[6] and is illustrated in Fig. 1.2. Since its proposal the concept has attracted an extraordinary amount of attention in the spintronics community, additionally empowered through a couple of major scientific breakthroughs in the area of magnetization dynamics and current-induced magnetic domain wall motion. We will discuss these breakthroughs in more detail in the literature review part of this thesis (see chapter 2).

Simplified, a (random access) memory device consists of three elementary parts. First a medium, where the information is stored, second & third a mechanism to write and read the information (individually), respectively.

For the RTMD, the information carrier is typically an arbitrarily long magnetic stripe of nanometer size in width and height, which is typically abbreviated as a *magnetic nanowire* or just *nanowire*. The magnetic nanowire contains the encoded information as a series of magnetic domains, with their individual magnetization directions pointing typically in one of the magnetically stable equilibrium states. In case of a 2-state system, these states are then used as binary

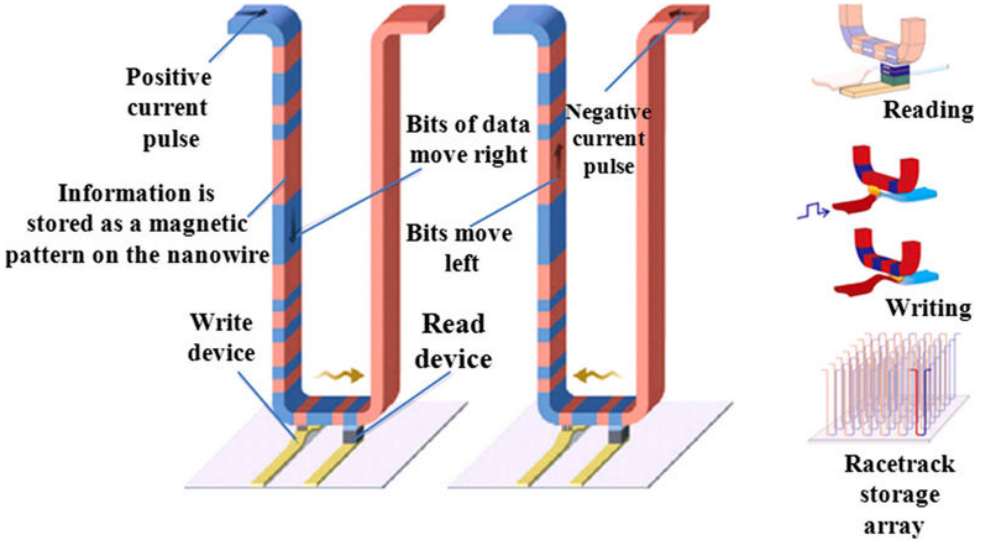

Abbildung 1.2: Racetrack memory device (RTMD) concept. A RTMD consists of three main elements: First, a magnetic stripe, where the information (highlighted in red and blue color blocks) is stored. Second and third, a reading and a writing element to read and write information (typically located below the magnetic stripe). The writing and reading process, as well as a concept for mass integration on a chip are illustrated on the right. (Courtesy of IBM and Ref. [5]).

information bits, normally seen as a logical '0', or '1' in the framework of information technology. In Fig. 1.2 a typical 3D-RTMD design is illustrated. The two bit states of the magnetic nanowire are highlighted in red and blue color coding, respectively.

The fundamental idea of the RTMD is to shift the bit pattern (e.g. 10010...) embedded as a series of magnetic domains (red, blue, blue, red, blue, red,....) along the nanowire. Thou, in contrast to other magnetic storage device technologies (e.g. floppy disk, HDD, and tape drives), the RTMD contains of no macroscopic mechanically moving parts, but instead the internal magnetization texture itself is moved.

One very promising feature of the RTMD concept is that it can be implemented not only in 2D, but (eventually) also as a 3D storage device, as already illustrated in Fig. 1.2. This design results in very promising ultra-high storage densities, which makes the RTMD concept extremely attractive from an industrial point of view.

Another advantage of the RTMD concept is its a priori non-volatility. Due to the use of magnetic domains as information carriers, the magnetic states remain even if the devices power is off. However, this can only be achieved, if the magnetic material is chosen to be magnetically stable enough against influences from the environment such as thermal fluctuations or external magnetic fields.

The shifting of magnetic domains and their confining boundaries, which are called magnetic *domain walls* (DWs), can be achieved in various ways. E.g. one can apply an external magnetic field to manipulate the domain pattern. This would grow all domains being aligned parallel to the external magnetic field and shrink these being anti-parallel, as illustrated in Fig. 1.3 (a)-(f).

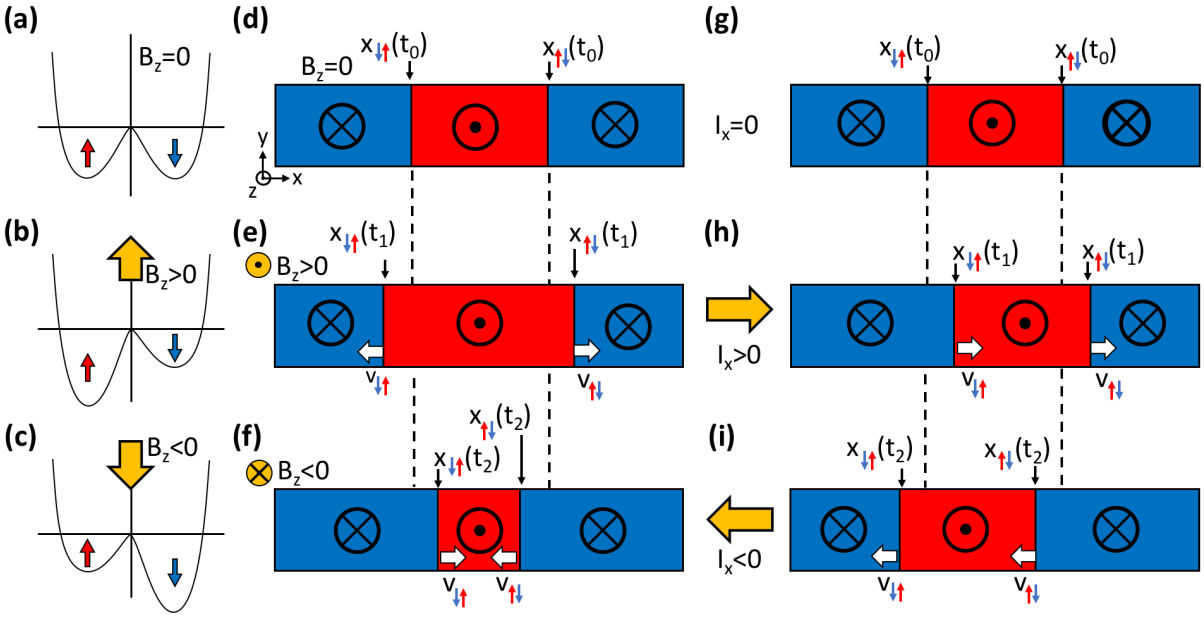

Abbildung 1.3: Illustration of field- & current-induced DW motion in a magnetic nanowire system with perpendicular magnetic anisotropy. On the left (Fig. (a) - (c)), the energy bands for the ↑- and ↓-magnetization states are schematically illustrated. (a) shows the equilibrium state, (b) and (c) show the cases when an external magnetic field is applied in the positive or negative z-direction, respectively. In the middle (Fig. (d) - (f)), field-induced DW motion is illustrated. Here, a series of alternating states is shown, representing a particular bit series (0, 1, 0) embedded into the magnetization texture of the magnetic nanowire. (d) If no external magnetic field is applied to the system, both magnetic states are energetically degenerated and the magnetic system is in its equilibrium state. The ↑↓- and ↓↑-DWs are at rest. (e) If a magnetic field, $B_z > 0$, is applied to the system, the ↑-state becomes energetically favorable, which results in a growth of the ↑-domain (red). Accordingly, the ↓-domains (blue) shrink in size. (f) shows the reversed case for $B_z < 0$, resulting in a reversed effect, respectively. On the right (Fig. (g) - (i)), current-induced DW motion is illustrated. Here, synchronous motion of the DWs can be achieved, meaning the ↑↓- and ↓↑-DWs can be moved in the same direction (here parallel to the current), without a change of the individual domain sizes. $x_{\uparrow\downarrow}(t)$ and $x_{\downarrow\uparrow}(t)$ indicate the position of the ↑↓- and ↓↑-DWs before and after the indicated fields or currents are applied, respectively. Equivalently, $v_{\uparrow\downarrow}$ and $v_{\downarrow\uparrow}$ (white arrows) indicate the corresponding DW velocity directions.

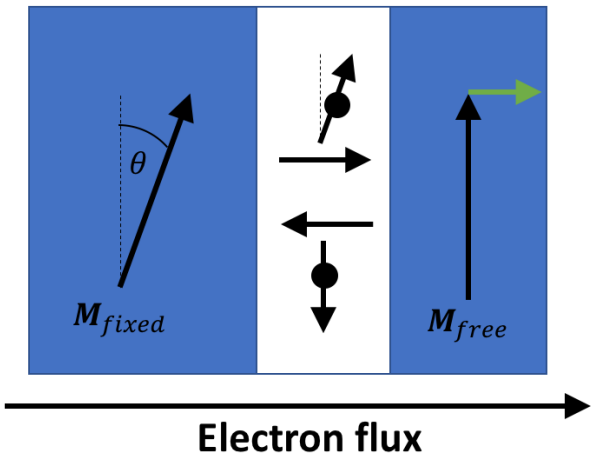

Abbildung 1.4: Simplified illustration of the STT effect proposed by J. C. Slonczewski[8] and L. Berger[9]. If current is applied to a trilayer system consisting of two ferromagnets (FMs), separated by a NM layer in between, polarized spins in the direction of the magnetization, $\boldsymbol{M}_{\text{fixed}}$, in the thicker FM layer, transfer spin angular momentum to the thinner FM layer, acting on its magnetization vector, $\boldsymbol{M}_{\text{free}}$. Effectively, the STT (green arrow) causes both magnetization vectors to align parallel into the direction of $\boldsymbol{M}_{\text{fixed}}$.

Key to the original RTMD-proposal was that the domain pattern can also be shifted synchronously along the nanowire by using *current-induced DW motion* (CIDWM) (Fig. 1.3 (g) - (i)). Here, the individual domain sizes are unchanged during the motion. This feature is particular important because a change in domain size could result in an annihilation of two neighboring domains and therefore eventually in a loss of stored information. Even though a synchronous motion of a domain pattern has been shown to be also possible by using a local external magnetic field with a special field pulse shape[7], the most potential of the RTMD-concept lays in its design as an all-electrical device using the CIDWM, because of its better scaling behavior compared to field-driven motion[6]. The underlying driving mechanism of CIDWM is the so-called *spin-transfer torque* (STT)-effect.

Originally proposed in 1996 by J. C. Slonczewski[8] and L. Berger[9], the STT describes the current-induced transfer of spin angular momentum between two non-collinear ferromagnetic layers, which are separated by a third non-magnetic (NM) layer, as illustrated in Fig. 1.4. However, spin angular momentum can also be transfered between two neighboring domains within a single ferromagnetic layer, e.g. if the neighboring domain's magnetization direction is slightly misaligned. Then, the STT generates effectively a shift of the DW separating the two domains. We will discuss the STT effect and CIDWM in more detail in chapter 2.

One of the key challenges in order to design an efficient RTMD based on the (classical) STT effect is that one has to apply very high current densities, $j_c \approx 1 \times 10^{11} - 1 \times 10^{12}$ A/m^2, in order to be able to unpin and move DWs. The resulting DW velocities when driven by the (classical) STT have been found to be only moderate.

In recent years, much faster DW motion has been observed in a particular class of material systems, consisting of a heavy-metal / ferromagnet / oxide (HM/FM/Oxide) hetero-structure. This led to the discovery of the so-called *spin-orbit torques* (SOTs), as well as certain chiral

effects associated to the symmetry breaking in those dissimilar multilayer stacks exhibiting naturally a structural inversion-asymmetry (SIA).

In order to find suitable material systems for the application in a RTMD, a key task is to understand the driving mechanism of the DW motion, which means to understand the current-induced STTs and SOTs present in a particular system.

1.3 Goal of this thesis

In the perspective of a possible application in a DW-based memory device such as the RTMD, the overall goal of this thesis is to study the acting torques in the high-anisotropy HM/FM/Oxide multilayer system, Ta/CoFeB/MgO.

Recently, ultra-efficient DW motion has been observed in similar multilayer nano-structures and led to the development of the state-of-the art SOT model in order to explain the observations.

It was found that the torques present in such systems are typically present as a mixture of multiple SOT contributions, originating e.g. from the so-called *spin Hall effect* (SHE) and from the *inverse spin galvanic effect* (ISGE), which we will introduce in more detail in chapter 2.

Following this model, one expects a maximum spin-torque efficiency acting on the DW, when the SOTs generated in the HM-layer of the multilayer stack are acting on a Néel type DW, if the current is flowing perpendicular to the DW profile. If the current instead is applied parallel to the DW, the SOTs should be maximized for a Bloch type DW and vanish for a Néel wall.

Recently, a novel measurement method, i.e. the torque magnetometry method, has been developed. This method allows to measure the acting SOTs of a system by using a higher harmonics analysis of the AHE. However, the technique allows only to measure the torques acting on homogeneous macro-spin structures.

Before this thesis it has not experimentally been confirmed, that the net action of the SOTs, measured for a macro spin-structure with the torque magnetometry method is actually consistent with the net effective torque acting on complex spin structures such as DWs, which consists of spins pointing in various directions. The main goal of this thesis is to verify this connection and to test the predictive power of the spin torque magnetometry method for DW motion properties.

In order to test this assumption, we perform both, torque magnetometry, as well as DW depinning measurements on the same sample and on the same nano-patterned Hall cross geometry. Using the current-field equivalence the net action of the SOTs can then be determined in the form of an effective torque efficiency and both methods can be compared.

Next to this main question we are also interested in the material properties of our multilayer stack itself, in particular in the size of the so-called *field-like*(FL) and *anti-damping-like* (AD) SOTs and the classical STT, which we will introduce in more detail in chapter 2. Additionally, we wanted to test the predicted symmetry of the SOTs.

1.4 Outline of this thesis

The remaining of this thesis is structured as follows:
First, we give in chapter 2 a brief introduction into the fundamental theoretical concepts of magnetism in condensed matter thin films and current-induced magnetization dynamics. Then we introduce in more details the recently discovered SOTs and certain chiral effects emerging in HM/FM/Oxide multilayer systems. Both together are found to be responsible for the ultra-efficient DW motion in those systems.

In chapter 3, we characterize in more details the material system we study in this thesis, namely Ta/CoFeB/MgO. Next, we describe the nano-patterning process that we use to build magnetic nanowire structures with Hall-bar geometry out of an initially grown thin film. Finally, we introduce the experimental setup, that we use to study the current-induced torques.

The outline of the experimental part of this thesis is to study first in chapter 4 the angular dependence of the SOTs in our material system for a simple homogeneous magnetic texture. Then we use these results to calculate the expected effective torques on more complex magnetic textures, such as Néel type magnetic DWs (see section 4.4).

Next, we test the validity of the model, which we use to calculate the effective torques for DWs. For that we first establish a measurement procedure to reliably create DWs in chapter 5. Then we measure the current-induced effects acting on the DWs during the DW depinning experiments, where the DWs are pushed through a Hall-bar geometry pinning site. To study the symmetry of the torques and validate the SOT model, we perform the depinning experiments, while we simultaneously manipulate the internal spin-profile of the pinned DW with an external in-plane magnetic field (see chapter 6). Furthermore, we repeat the DW depinning experiment for current applied parallel and perpendicular to the DW.

Technically, the current-induced spin torques acting on a DW structure are determined by using the current-field-equivalence Ansatz during the DW depinning experiments, as we will introduce in chapter 6. The analysis method following this Ansatz has been established previously [10] and allows us to quantify the current-induced depinning process of a DW from a pinning site in terms of an effective DW depinning field.

Using these two methods, the torque magnetometry method and the DW depinning measurement, it is possible to compare two fundamentally different techniques for the evaluation of current-induced spin-torque effects on magnetic structures (see chapter 7).

This kind of comparison connecting the torques present in macro-spin dynamics with the torques acting on more complex spin-textures, such as DWs has not been addressed in the literature before this thesis.

2 Background and literature review

2.1 Introduction

This chapter is intended to give the reader a brief overview over the physics involved in this thesis. We will first give a short introduction into ferromagnetism in general and then focus on the characteristics of magnetic thin film multi-layer systems, that are patterned into nanostructures, as we will use them later in the experimental part. The engineering of artificial thin film magnetic systems is compared to the research of general magnetism a relatively novel topic, which became advanced together with the ability to deposit ultra-thin material layers in a controllable manner on top of each other by using e.g. molecular beam epitaxy, thin film sputtering or evaporation techniques[11].

In this thesis we will focus on the sub-field of CIDWM and its related spin-orbit coupling (SOC) phenomena involved in state-of-the-art magnetic multilayer systems, which are relevant e.g. for novel magnetic storage device concepts, such as the above mentioned RTMD[6].

First, we start in section 2.2 by introducing the involved interactions present in a general magnetic system. Most dominantly is the quantum mechanical exchange interaction between multiple electrons. For the description of patterned magnetic thin film hetero-structures further interactions and corresponding energy terms are relevant. These are e.g. the Zeeman energy, the uniaxial anisotropy energy, the dipolar energy and the Dzyaloshinskii-Moriya energy.

Having established a basic understanding of the present interactions, we discuss second in section 2.3, the formation of magnetic domains and the occurrence of different possible DW types in inversion symmetric (see subsection 2.3.1) and asymmetric magnetic systems (subsection 2.3.2) as a consequence of the competition between the involved energy contributions.

Third, we discuss in section 2.4 the field- and current-driven magnetization dynamics and the controlled motion of magnetic DWs in confined ferromagnetic nanostructures driven by an external magnetic field and via the current-induced STT effect.

Next, we introduce in section 2.5 the concepts of in-plane and perpendicular magnetic anisotropy.

Then, we discuss in section 2.6 recent theoretical concepts and experimental observations concerning SOT driven phenomena and chiral DW motion in HM/FM/Oxide systems. This will allow us to review recent work addressing the angular dependence of the acting SOTs in such systems, which we want to investigate experimentally in this thesis at the example of a Ta/CoFeB/MgO multilayer nanostructure.

Since all of our main experimental methods used in this thesis rely on the use of the Hall effect in magnetic systems, we will give in section 2.7 also a short introduction to the physics of the Hall effect, with a focus on the anomalous Hall effect.

2.2 Magnetic interactions

Central to the modern microscopic picture of magnetism in condensed matter systems is the electron. Here, magnetism has basically two main origins: First the orbital magnetic moment of the electron, μ_l, which is related to the orbital motion of the electron around the core of an atom and second the spin-magnetic moment, μ_s, which is related to the intrinsic spin angular momentum, $\boldsymbol{S}$, of the electron via $\mu_s = \gamma\mu_B\boldsymbol{S}$. Here, γ is the gyromagnetic ratio and $\mu_B = e\hbar/2m_e$ is the Bohr magneton, whereby e is the electron's charge, $\hbar$ is the Planck constant and m_e is the mass of an electron. In the quantum mechanical picture μ_l and μ_s are coupled together to a total magnetic moment of the spin system, μ_j, which combines the orbital and spin magnetic moment to an effective spin-orbit (SO) magnetic moment of the electron in its specific environment following Hund's rules[12,13].

Considering a many body system of electrons, e.g. a metallic solid, the superposition of various possible interactions between the electrons can lead to quite complex forms of magnetic phenomena and spin textures. In this thesis we are in particular interested in HM/FM/Oxide multilayer systems with the FM layer, being composed of e.g. Fe & Co constituents.

At the heart of the so-called itinerant ferromagnets, Fe, Co & Ni, is the quantum-mechanical (symmetric) exchange interaction between the electron spins, causing two neighboring spins to point in a parallel direction, leading to the standard form of ferromagnetism as we know it from day-to-day magnetic objects.

The spin-dependent part of the effective Hamiltonian, $\mathcal{H}$, describing such systems can be written as:[12,13]

$$\mathcal{H} = -2\mathcal{J}_{12}\mathbf{S}_1\mathbf{S}_2, \tag{2.1}$$

where $\mathcal{J}_{12}$ is the exchange integral, and $\mathbf{S}_1$ and $\mathbf{S}_2$ are the spin-vectors of two interacting electrons. For ferromagnetic systems $\mathcal{J}_{12} = \int \psi_1^*(\boldsymbol{r}')\psi_2^*(\boldsymbol{r})\mathcal{H}(\boldsymbol{r},\ \boldsymbol{r}')\psi_1(\boldsymbol{r})\psi_2(\boldsymbol{r}')d\boldsymbol{r}^3d\boldsymbol{r}'^3 = \frac{1}{2}(E_s - E_t) > 0$, with $\psi_{1,2}$ being the wavefunctions of two interacting electrons indicated with indices 1 & 2 and E_s and E_t being the energies for the singlet and triplet states of the hybridized wave function of these electronic states, respectively.

In order to describe magnetism in condensed matter many-body systems, the exchange interaction between two electrons can be generalized for the case of a large number of electrons, yielding:[12,13]

$$\mathcal{H} = -\sum_{ij}\mathcal{J}_{ij}\mathbf{S}_i \cdot \mathbf{S}_j. \tag{2.2}$$

This Hamiltonian is commonly known as Heisenberg Hamiltonian or the Heisenberg model[12].

In order to describe such a many-particle system effectively, one can apply e.g. a mean-field approximation, modeling the $N \times N$-interaction terms in the Heisenberg model to a simpler recursive model, where each electron i out of N electrons interacts with the average effective (mean-)field given by the residual electrons[14].

Another approach to deal with those multi-electron systems effectively is e.g. to describe them not individually anymore, but instead introduce charge- and spin-density distributions, which leads to the theoretical framework of density functional theory (DFT)[15]. However, within this thesis we do not want to go in detail into this broad topic and continue with the other relevant interactions of the electrons.

Next to the already discussed symmetric exchange interaction between spins, there exist also an anti-symmetric form. A few materials with low symmetry can exhibit an anti-symmetric coupling, i.e. the so-called Dzyaloshinskii-Moriya interaction (DMI)[16,17]. The DMI leads to a coupling where energy is saved when two neighboring spins are pointing perpendicular to each other. This can be represented by the Hamiltonian:[12,13]

$$\mathcal{H} = -\mathcal{D}_{ij} \cdot (\boldsymbol{S}_i \times \boldsymbol{S}_j), \tag{2.3}$$

whereby $\mathcal{D}_{ij}$ is the DMI vector pointing along the high-symmetry axis. Typically the DMI is much smaller compared to the symmetric exchange interaction: $|\mathcal{D}/\mathcal{J}| \approx 10^{-2}$[13]. However, as we will discuss in section 2.3.2, the DMI can have a significant effect in multilayer systems leading e.g. to homo-chiral spin textures[18,19] and chiral damping[20,21] causing certain asymmetries in typical observables such as the DW velocities with respect to a applied magnetic in-plane field under current[22,23].

When a magnetic spin, $\boldsymbol{S_i}$, is placed in a magnetic field $\boldsymbol{B}$, the electromagnetic interaction between both forces the spin to align parallel to the field in order to save energy. This interaction can be described in the Hamiltonian as a simple dot-product and is usually called Zeeman energy term or Zeeman interaction:[12,13]

$$\mathcal{H}_{Zeeman} = -g\mu_B \boldsymbol{S_i} \cdot \boldsymbol{B}, \tag{2.4}$$

with g being the Landé-factor of the electron. The Zeeman interaction allows us later to manipulate the magnetic spins of a system with an applied external magnetic field. We will discuss this further in the DW motion section 2.4.

In confined and crystalline magnetic systems there are typically certain directions, where it takes more energy to magnetize the system into, than into others. The origin of this is the SOC, which links the electron's orbits to the crystallographic structure and by their interaction with the spins makes them align along the preferred crystallographic axes[24]. The preferred axis is typically called as the *easy axis* of the system, contrary to the not preferred *hard axis*, where it is typically much harder to align the magnetization into. The special case of magnetocrystalline anisotropy in magnetic crystals can usually be represented as an expansion of powers of the magnetization vector direction cosines or sines. Due to time reversal symmetry only even powers of the cosines (sines) are allowed. The non-zero terms depend on the specific crystal structure. Typically, the anisotropy of the magnetization can be represented by an anisotropy energy density:[12,13]

$$\epsilon_a = K_1 \sin^2\theta + K_2 \sin^4\theta + ... \approx K_1 \sin^2\theta \tag{2.5}$$

Here, θ is the angle between the magnetization vector, $\boldsymbol{M}$, and the anisotropy axes. K_1 & K_2 are the corresponding anisotropy constants, with units J/m^3. Possible higher terms are not further discussed here. For uni-axial systems, in which the energy density depends on the angle to only a single axis, Eq. (2.5) can be approximated by only the K_1-term. However, in cubic systems for example, the appropriate expression becomes more complex, leading to also more complex anisotropy terms. A sufficient introduction to this topic can be found e.g. in [12,13,24] and is not discussed further here.

Another source for anisotropic magnetism can be the physical shape of a magnetic system, which gives rise to the so-called *shape anisotropy* energy, E_s. This is because whenever spins point perpendicular to a surface of a sample, the resulting dipolar stray field can not be compensated by their neighboring magnetic moments leading to an overall energy penalty. For a thin film, this can be formally modeled with: [12,13]

$$E_s = \frac{1}{2}\mu_0 M^2 \cos^2\theta. \tag{2.6}$$

The shape anisotropy is typically part of the internal demagnetizing energy of a magnetic system. However in sample systems, as we will use them in this thesis, the magnetic thin films are patterned into low-dimensional nanowires, where the magnetic anisotropy and dipolar energy is described in effective energy equations, as we will see later in the perpendicular magnetic anisotropy section 2.5.

Materials with high magnetic anisotropy usually also exhibit a high coercivity, thus they are hard to magnetize. These are for example the rare earth metal alloys. Soft magnets in contrast have typically a low coercivity, thus are relatively easy to magnetize and also fast to switch. This makes them for example ideal for transformers and inductors.

The challenge in fine-tuning the anisotropy of a magnetic material, e.g. when it is used as the recording medium in a storage device, is to find a trade-off between fast and energetically easy switchable (writable) materials and a high stability of the written magnetic states against e.g. external disturbances, which can cause unintended switching events and the loss of information, accordingly.

Techniques like heat-assisted switching, where during the switching event the coercivity is artificially lowered by a heating of the otherwise high coercive magnetic material, are common in the field of magnetic recording [25,26] and become also relevant for current-induced DW nucleation and depinning processes, which we investigate within this thesis in chapter 5 and 6.

2.3 Magnetic domains and domain walls

In the last section we have introduced all the relevant magnetic interactions present in our material system. It is natural that the magnetic system, as any physical system, tends to be in its most energetically favorable state. Since the different interactions would lead to competing favored magnetization directions a compromise state will be the result of the energy minimization process. As a simple example, the ferromagnetic exchange interaction leads to parallel alignment of the electron spins at short distance. Even though this state can be locally the energetic minimum, it

can be energetically unfavorable for a large number of spins to be in that state, because it can in finite geometry maximize the resulting stray field, which is the dominant term for long distances because of its $\propto r^{-3}$ scaling behavior. In order to minimize the energy of the whole system, the magnetic state therefore splits naturally into multiple magnetic subsystems, which are called *magnetic domains*. In each domain all the spins are pointing in a uniform direction forming a macro magnetization vector, whose direction differs from domain to domain. If the neighboring domain's stray field will be such that they cancel each other, it effectively reduces the overall energy of the system[12,13].

At the boarder of the domains the spins do not change abruptly, e.g. form the ↑-state in one domain into the ↓-state in the neighboring domain, which would cost a huge exchange energy penalty. Instead, a smooth and continuous transition region is formed. This transition region is called a *magnetic domain wall*[12,13].

The width of a DW is typically determined by the competition between the exchange energy ϵ_{ex} and the dipolar energy ϵ_d of the system. The characteristic length scale is the exchange length $\lambda_{ex} = \sqrt{\frac{A}{\mu_0 M_s^2}}$. It is the shortest length scale on which the magnetization can be twisted in order to minimize the dipolar interaction. Hereby, A is the magnetic exchange stiffness. In our thin film samples the DW width, Δ, is effectively given by $\Delta = \sqrt{\frac{A}{K_{\text{eff}}}}$, with K_{eff} the effective magnetic anisotropy constant of the magnet. Typically, DW widths are between $\approx 1 - 10$ nm for harder magnets (e.g. Co or Fe) to > 100 nm for softer magnets (e.g. Py)[13].

2.3.1 Néel- and Bloch-walls

If the magnetization angle rotates from e.g. the ↑-state in one domain into the ↓-state in the neighboring domain, one can speak of a 180° wall. The most common types of 180° walls are the *Bloch wall*[27] and the *Néel wall*[28]. Fig. 2.1 illustrates the profiles of both wall types.

In case of a Bloch wall the magnetization rotates in a plane parallel to the plane of the wall (indicated with grey color in Fig. 2.1 (a)). The Bloch wall has the property that it creates no divergence of the magnetization. Since $\boldsymbol{\nabla} \cdot \boldsymbol{M} = 0$, there is no magnetic charge and no source of demagnetizing field inside the wall, since $\boldsymbol{\nabla} \cdot \boldsymbol{H_d} = -\boldsymbol{\nabla} \cdot \boldsymbol{M}$[12,13].

In case of a Néel wall the magnetization rotates in a plane perpendicular to the plane of the wall (also indicated with grey color in Fig. 2.1 (b). The Néel wall has normally a higher energy than the Bloch wall because of the stray field it creates by the nonzero divergence of $\boldsymbol{M}$. But unlike the Bloch wall, the Néel wall creates no surface charges. Accordingly, there is no associated stray field. Therefore Néel walls are only stable in films thinner than the wall width[13].

To rotate the magnetic moments from the Bloch into the Néel type configuration, an in-plane anisotropy, K_D, has to be overcome. This can be expressed as $K_D = {}^1\!/_2 N_x \mu_0 M_s^2$, where N_x is the demagnetizing factor, which depends on the DW width, Δ, and the film thickness, t. In PMA systems this can be achieved either by applying an external magnetic field, $\boldsymbol{H}_x$, in the film plane, which lifts the DW out of its Bloch type ground state, or, for suitable material layers below or above the magnetic layer, which break the inversion symmetry of the multilayer system, the ground state can be changed to Néel type by a fictitious magnetic field representing the effects of

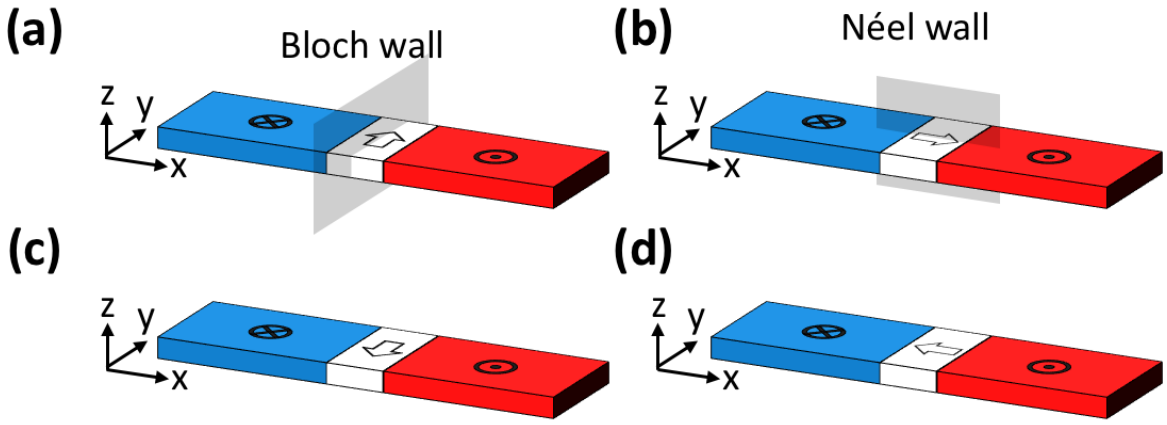

Abbildung 2.1: Illustration of Bloch and Néel type DWs in a thin magnetic film exhibiting perpendicular magnetic anisotropy. (a) & (c) show Bloch walls, with the moments of the walls pointing in the $\pm\hat{y}$-direction, reflecting both different chiral versions of the wall. (b) & (d) show the same, but for a Néel wall, which is pointing in the $\pm\hat{x}$-direction, respectively.

the DMI[18,19,29]. This will lead to the so-called homo-chiral DWs, which we will discuss in the next subsection.

2.3.2 Homochiral domain walls

In general both, the Bloch and the Néel wall, can exist in two chiral versions each. One version with a clockwise and the other with a counter-clockwise rotational sense. In an ideal inversion symmetric system, where no defects and no external influences, such as e.g. external magnetic fields are applied to a sample, both chiral versions of the ground state type DW would be generated in average equally often, since they are energetically equivalent and their formation relies only on spontaneous processes.

However, in material systems, where inversion symmetry is broken, e.g. in certain bulk inversion asymmetric crystals or at interfaces between dissimilar stacked materials, such as HM/FM bilayer systems, where the HM exhibits a strong SOC, the anti-symmetric exchange interaction at the interface can lift the energetic degeneracy of the two chiral versions of the DW. As a result, one rotational sense will become energetically favored. This will effectively lead to homochiral DWs, which all rotate with the same chirality, as depicted in Fig. 2.2.The rotational sense of the chiral wall is given by the sign of the DMI vector, $\mathcal{D}_{ij}$. The effective DMI field for a given $\mathcal{D}_{ij}$ reads[19]

$$\boldsymbol{H}_{\mathrm{DMI}} = \frac{\mathcal{D}_{ij}}{\mu_0 M_s \Delta}, \tag{2.7}$$

with $\boldsymbol{H}_{\mathrm{DMI}}$ pointing along the $\pm\hat{x}$-direction when $\mathcal{D}_{ij}$ is pointing along the $\pm\hat{y}$ direction for an $\uparrow\downarrow$-DW. For a $\downarrow\uparrow$-DW the symmetry would be the same, but with the opposite signs. Fig. 2.2 (a) shows an illustration of such homochiral $\uparrow\downarrow$- and $\downarrow\uparrow$-DWs, where the magnetization direction is

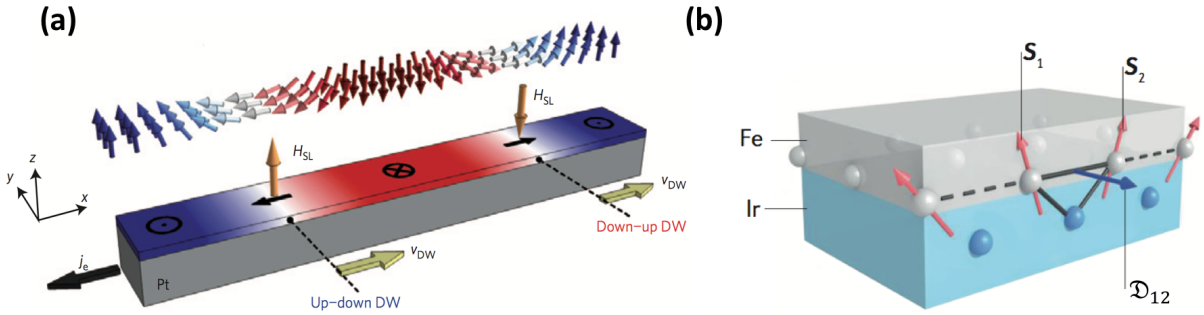

Abbildung 2.2: (a) Illustration of synchronous motion of homo-chiral DWs driven by the current-induced anti-damping SOTs. DWs in Pt move in the direction of current-flow. The effective DMI-field originating from the structural inversion asymmetry is illustrated at the position of the DW's center in black color (Courtesy of Ref[18]). (b) Illustration of the inversion asymmetric bilayer composing of a HM/FM bilayer, (Fe/Ir), where the strong SOC of the HM layer, together with the ultra-thin FM, results in a non-collinear spin chirality determined by the interfacial DMI vector $\mathcal{D}_{12} \neq 0$. (Courtesy of Ref.[30]).

rotating anti-clockwise, when looking to the positive $\hat{x}$-direction. The black arrows at the center position of the DW indicate the corresponding orientations of $\boldsymbol{H}_{\mathrm{DMI}}$.

The existence of interfacial DMI was first demonstrated by the observation of spiral-like spatial modulations of the spin orientation with a winding periodicity related to the magnitude of the DMI in single atomic layers of manganese on tungsten (110)[31]. This paper represents the first identified observation of interfacial DMI-induced spin modulations in ultra-thin magnetic films. Recently, homochiral DWs have been also discovered in HM/FM/Oxide systems[18] and are since then subject to intense research efforts. This is partially because a chain of DWs, all with the same rotational sense, have the property, that they can be moved with current in the same direction and as discovered recently for Néel type DWs with ultra-high velocities. This is due to the interaction of the SOTs, acting on the homochiral DWs. We will discuss them further in section 2.6, after we have introduced the classical spin transfer torques and the basics of the DW motion.

2.4 Magnetization and domain wall dynamics

So far, we have introduced the different interactions present in a magnetic thin film system and have discussed the formation of static magnetic DWs as a consequence of energy minimization. Next, we want to discuss the field- and current-induced motion of the DWs. For that, we start by first looking into the dynamics of a single magnetization vector, $\boldsymbol{M}$, which is slightly misaligned with its equilibrium position in the presence of an effective magnetic field. This will give rise to a precessional motion and an effective damping towards the equilibrium direction[32]. Having this, we discuss the scenario when a current is applied to a magnetic sample. This will generate additional current-induced torques acting on the magnetization vector, the STT[32]. This lays the foundation to understand the collective field- and current driven motion of inhomogeneous spin-textures, such as magnetic DWs.

The following discussion and understanding is mostly adapted from the review paper by O. Boulle et al.[32] and also from A. Thiaville et al.[33]. All other references used, are mentioned at there occurrence.

In order to describe magnetization dynamics, we consider for a moment a local uniform magnetization texture in a solid, which is described by the magnetization macro-vector, $\boldsymbol{M}$, which is pointing out-of its natural equilibrium direction (e.g. due to thermal fluctuations in the system). This situation is depicted in Fig. 2.3 (a). Since $\boldsymbol{M}$ is not aligned parallel anymore to the effective

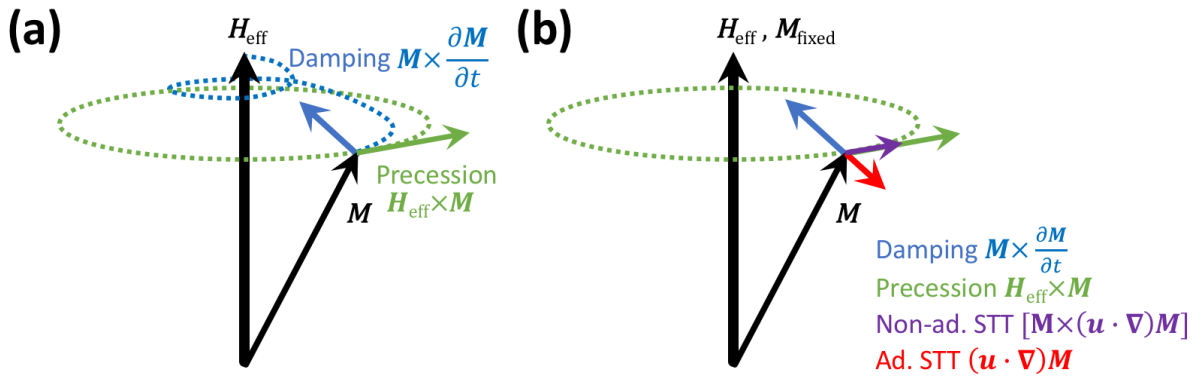

Abbildung 2.3: (a) Illustration of a misaligned magnetization vector, $\boldsymbol{M}$, in the environment of an effective magnetic field, $\boldsymbol{H}_{\text{eff}}$, leading to precession of $\boldsymbol{M}$ around $\boldsymbol{H}_{\text{eff}}$. The symmetric exchange energy in a ferromagnetic system forces the magnetization vector to align parallel to the magnetic field, which is reflected by the effective damping perpendicular to the precession motion pointing from $\boldsymbol{M}$ towards $\boldsymbol{H}_{\text{eff}}$. (b) Illustration of the forces on a magnetization vector when additionally a current is applied to the sample, giving rise to an adiabatic (ad.) and non-adiabatic (non-ad.) STT, which are highlighted in red and purple color, respectively. Depending on the sign of the applied current, the STT can have a stabilizing or destabilizing effect on $\boldsymbol{M}$. Once $\boldsymbol{M}$ is pointing into the negative hemisphere, the damping mechanism forces it into the down-direction. This happens e.g. during a magnetization switching event.

magnetic field

$$\boldsymbol{H}_{\text{eff}} = -\frac{1}{\mu_0 M_s}\frac{\delta E}{\delta \boldsymbol{M}}, \tag{2.8}$$

with δE being the Landau free energy of the system, a torque

$$\tau_{pre} = \boldsymbol{M} \times \boldsymbol{H}_{\text{eff}} \tag{2.9}$$

is acting on the magnetization leading to precession of $\boldsymbol{M}$ about $\boldsymbol{H}_{\text{eff}}$, with $\omega = -\gamma H_{\text{eff}}$ the so-called *Lamor frequency*.

Since the system tends to be naturally in its state of minimum energy one can expect an effective damping mechanism towards the equilibrium direction. This damping has been modeled phenomenologically first by L. Landau and J. M. Lifshitz[34] and then modified by T. L. Gilbert[35],

leading to the so-called Landau-Lifshitz-Gilbert (LLG) equation. It describes the time variation of the magnetization vector $\boldsymbol{M}$. Its classical form reads[36]:

$$\frac{d\boldsymbol{M}}{dt} = -\gamma \boldsymbol{M} \times \boldsymbol{H}_{\text{eff}} - \frac{\alpha}{M_s} \boldsymbol{M} \times \frac{d\boldsymbol{M}}{dt}, \tag{2.10}$$

where the first term on the right side describes the magnetization precession due to an effective field and the second term the damping of the magnetization, with α being the so-called Gilbert damping parameter.

Two decades ago L. Berger[9] and J. C. Slonczewski[8] discussed the electrical manipulation of magnetic structures using STTs. Similar to an electrical current, carried by moving electrons, moving spins in a condensed matter system, associated with the conduction electrons, carry a spin current. If the spin current passes a spacial varying magnetic structure, e.g. a magnetic DW, the spins of the conduction electrons in the ferromagnet (in our case the $4s$ electrons in the CoFeB layer), interact with the spins of the electrons forming the local magnetization structure (in our case the $3d$ electrons in the CoFeB layer), by exchanging spin angular momentum (see Fig. 1.4).

As we will see in the following, there can be multiple sources for current-induced torques in a magnetic system. We start with the so-called adiabatic STT. It describes the idealized situation, where spin angular momentum is exchanged from the conduction electrons adiabatically towards the local magnetization texture. In a simple model, this can only be realized if the gradient of the magnetization texture in the drift direction of the conduction electron flow is much smaller than the spin precession length

$$\lambda_L = \hbar \frac{v_F}{J_{\text{sd}}}, \tag{2.11}$$

with v_F being the Fermi drift velocity of the electron and J_{sd} the s-d-exchange interaction. λ_L is the length that an electron travels during one precession[37].

Therefore, the adiabatic case is typically only given for systems with large DW widths, realized typically in soft magnetic materials such as Permalloy. In this case the conduction electrons have enough time to exchange their spin angular momentum, being all along the DW sufficiently fast aligned to the local spin texture while traveling across it. The adiabatic STT can be described for a current density j applied e.g. in the $+\hat{x}$-direction as[32]:

$$\boldsymbol{\tau}_{\text{ad}} = \frac{jP\hbar}{2e} \frac{\partial \boldsymbol{M}}{\partial x}, \tag{2.12}$$

where P is the effective spin-polarization of the charge current and the term $\frac{\partial \boldsymbol{M}}{\partial x}$ describes the local directional change of the incoming spins. $\boldsymbol{\tau}_{\text{ad}}$ can be converted into a time derivative of the magnetization $\boldsymbol{M}$ by multiplying Eq. (2.12) by $-\gamma/M_s = -g\mu_B/(\hbar M_s)$. Typically one introduces here the so-called spin drift velocity

$$\boldsymbol{u} = \frac{jPg\mu_B}{2eMs}, \tag{2.13}$$

which is a vector directed along the direction of electron motion and which is defined as positive for $P > 0$, i.e. for carriers polarized along the majority spin direction density. It is also actually the maximum velocity, that the DW can reach in the adiabatic limit when the conduction electron spin moments are fully converted into DW displacement. The velocity of the DW can be defined by[32]

$$\boldsymbol{v}_{\mathrm{DW}} = \frac{\Delta \boldsymbol{l}}{\Delta t} \equiv \boldsymbol{u}, \tag{2.14}$$

with $\Delta \boldsymbol{l}$ being the DW displacement within the time interval Δt. The generalized time derivative version of Eq. (2.12) then reads[32]:

$$\frac{\partial \boldsymbol{M}}{\partial t} = -(\boldsymbol{u} \cdot \boldsymbol{\nabla})\boldsymbol{M}. \tag{2.15}$$

As mentioned above, beside the adiabatic STT there can exist also other current-induced torques. After the adiabatic STT was not sufficient to explain some experimental observations of CIDWM[38–42] the model had to be extended. S. Zhang and Z. Li[43] & A. Thiaville et al.[33] proposed an additional non-adiabatic STT contribution based on spin-relaxations processes via spin-flip scattering events of the conduction electrons with e.g. impurities, phonons, etc.[32]. These can be described phenomenologically e.g. by a term[33]:

$$\frac{\partial \boldsymbol{M}}{\partial t} = \frac{\beta_{sf}}{M_s} \left[\boldsymbol{M} \times (\boldsymbol{u} \cdot \nabla)\, \boldsymbol{M}\right], \tag{2.16}$$

with β_{sf} being the dimensionless non-adiabaticity parameter, which is independent of the current density, j, and can be directly linked to the exchange energy, J_{sd} and the spin relaxation time, τ_{sf}, with $\beta_{sf} = \hbar / J_{sd}\tau_{sf}$. β_{sf} is estimated to be typically of the order of 10^{-2} comparable to the Gilbert damping parameter, α[33,43,44]. This torque acts perpendicular to the adiabatic torque and has the same symmetry as a torque generated by a magnetic field applied in the easy-axis direction of the magnetic system. Therefore, the non-adiabatic STT is also sometimes called as a FL-torque, contrary to the adiabatic torque, which is sometimes called as a damping or anti-damping torque, depending on the sign of the current direction and the sign of the majority charge carriers.

Beside the already described contribution to a non-adiabatic torque because of spin-relaxation, also other contribution have been discussed[32]. One other, that we want to discuss here, relies on the width of the DW. In the case that the DW width is sufficiently small, such that the adiabatic limit is not fulfilled, the incoming spins can not adapt perfectly to the local magnetization texture anymore. In the 1D model, this mismatch gives rise to a linear momentum transfer, when the electrons are reflected by the spatially fast varying spin texture, as elaborated e.g. by G. Tatara & H. Kohno[45]. Taking into account these two contributions, β can be written e.g. as $\beta \equiv \beta_{\mathrm{sf}} + \beta_{\mathrm{mismatch}}$.

Both, the adiabatic and non-adiabatic torque can be added to the right side of Eq. (2.10) leading to the following extended LLG equation including the current-induced terms[36]:

$$\frac{d\boldsymbol{M}}{dt} = -\gamma \boldsymbol{M} \times \boldsymbol{H}_{\mathrm{eff}} - \frac{\alpha}{M_s}\boldsymbol{M} \times \frac{d\boldsymbol{M}}{dt} - (\boldsymbol{u} \cdot \nabla)\, \boldsymbol{M} + \frac{\beta}{M_s}\left[\boldsymbol{M} \times (\boldsymbol{u} \cdot \nabla)\, \boldsymbol{M}\right]. \tag{2.17}$$

All the terms are illustrated in Fig. 2.3 (b).

The LLG equation describes only the dynamics of individual spins. In order to describe DW dynamics effectively, one can write the LLG equation in a more simple analytical form, by assuming a rigid DW profile. Here, the dynamics of a whole spin-texture can then be described by only two independent collective variables: First, the center position of the DW, q, and second, its conjugate momentum, the DW magnetization angle, ψ, as shown in Fig. 2.4. This

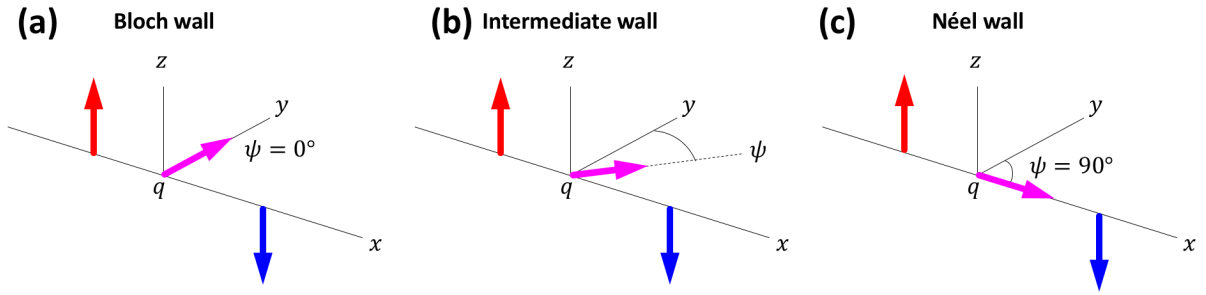

Abbildung 2.4: Definition of collective coordinates in the 1D model for a (a) Bloch wall and (b) Néel wall. (From Ref.[32].)

so-called one dimensional (1D) model (assuming the DW being sufficiently described by only its collective coordinates, $(q,\ \psi)$) can be applied for both, perpendicular and in-plane magnetic anisotropy materials and also applies to more complex spin-textures, such as Vortex walls[46] or skyrmions[47]. The differential equations of motion for the DW are then the following[32]:

$$\dot{\psi} + \alpha\frac{\dot{q}}{\Delta} = \gamma\mu_0 H_z + \beta\frac{u}{\Delta} - \frac{\gamma}{2M_s}\frac{\partial V_{\text{pin}}}{\partial q} \tag{2.18}$$

$$\frac{\dot{q}}{\Delta} - \alpha\dot{\psi} = \frac{\gamma\mu_0 H_k}{2}\sin(2\psi) + \frac{u}{\Delta} \tag{2.19}$$

with $H_k = 2K_d/(\mu_0 M_s)$ the demagnetizing field, where K_d is the demagnetizing energy. H_z is the applied field along the easy axis and V_{pin} is a spatially slowly varying pinning potential compared to the DW width[48].

One can note that the non-adiabatic torque enters Eq. (2.18) similar to the external out-of-plane field, H_z. Therefore one can speak of the non-adiabatic torque as an effective out-of-plane field directly proportional to the applied current density, j. It can be finally written in the form:

$$\mu_0 H_z^{\text{eff}} = \frac{\beta}{\Delta\gamma}u = \epsilon j \tag{2.20}$$

with $\epsilon = \frac{\beta P\hbar}{2eM_s\Delta}$ the non-adiabatic torque efficiency[33]. Using this current-field-equivalence, ϵ can directly be detected experimentally e.g. by performing DW depinning experiments[10,49,50], as we do in chapter 6.

Using this simple 1D model one can deduce e.g. the critical current for DW motion and the DW velocity in a system semi-quantitatively. As an example from the literature Fig. 2.5 shows the

typical behavior of the DW velocity as a function of (a) an applied external magnetic out-of-plane field and (b) under current.

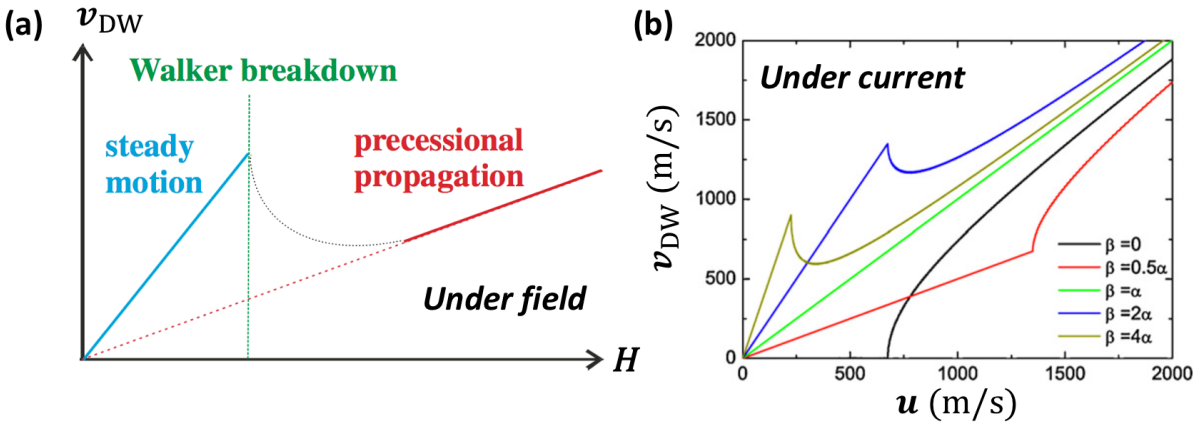

Abbildung 2.5: Sketch of a 180° DW's velocity as a function of (a) an external magnetic field $\boldsymbol{H}$ and (b) the spin drift velocity u, which relates to the applied current density, j. The DW motion can be separated into three typical regimes: First, for a small driving field (or current), the steady DW motion regime, where the DW profile stays constant and the velocity scales linearly with the applied driving force. Second, for an intermediate driving field (or current), the Walker breakdown regime, where the 1D model DW magnetization angle, ψ, starts to oscillate periodically, leading to a reduced or enhanced non-linear DW velocity behavior, depending on the ratio between β vs. α, respectively. Third, for a large driving field (or current), the precessional motion regime, where the DW velocity becomes linearly dependent on the driving force again. (b) shows how the DW dynamics transforms for various ratios β vs. α. Adapted from Refs.[32,51].

First, we discuss the purely field driven DW motion. Here, the DW will move in such a way so that the Zeeman energy is minimized. Accordingly, the domain with spins parallel to the external magnetic field will grow in size, as illustrated in Fig. 1.3 (d) - (f). If a single DW is present, the direction of the DW motion can be controlled by changing the direction of the external magnetic field. For weak external magnetic fields, the DW velocity will first increase linearly (blue solid line in Fig. 2.5 (a)), with a velocity $v_{\mathrm{DW}} = \mu H$, where $\mu = \gamma\Delta/\alpha$ is the DW mobility, until a critical field, the so-called Walker breakdown (WB) field, $\boldsymbol{H}_{\mathrm{WB}} = \frac{\alpha}{2} H_k$, is reached (green mark in Fig. 2.5 (a))[32]. For fields larger than the WB field the DW structure starts to change periodically. This is due to a precession of the internal magnetization around the effective field direction. The internal precession will effectively lead to an oscillatory back and forth motion, which results in an effective decreased average forward velocity, with a reduced mobility $\mu = \gamma\Delta/(\alpha + \alpha^{-1})$, as illustrated in Fig. 2.5 (a) (red solid line).

Next, we discuss the CIDWM. First, for an ideal nanowire, without pinning ($V_{\mathrm{pin}} = 0$) and with only the adiabatic STT being present ($\beta = 0$). Here, the DW is intrinsically pinned until a critical current density, j_c, is reached. In terms of the spin drift velocity, $\boldsymbol{u}$, this happens at $u_c = \gamma\mu_0 H_k \Delta/2$, which can be calculated by finding the stationary solutions to the 1D model equations of motion Eq. (2.18) & (2.19), with $\dot{\psi} \equiv 0$, $\dot{q} \equiv 0$ & $\sin 2\psi \equiv 1$. For the adiabatic case this critical current happens to be also the critical WB current, $u_{WB} \equiv u_c$. Here, the current-

induced torque is strong enough to overcome H_k. In the WB regime the average velocity can be described by

$$\langle v_{\mathrm{DW}} \rangle = \frac{\sqrt{u^2 - u_c^2}}{1 + \alpha^2}, \tag{2.21}$$

with $\langle v_{\mathrm{DW}} \rangle$, the average DW velocity (see black curve ($\beta = 0$) in Fig. 2.5 (b)).

Next, we include the non-adiabatic STT ($\beta \neq 0$). One crucial feature then is, that the DW is no longer intrinsically pinned anymore, as for the adiabatic STT and directly starts to move for low, but finite applied current densities with a velocity in the constant flow regime of[32]

$$v_{DW} = \frac{\beta}{\alpha} \cdot u. \tag{2.22}$$

However, this is only valid for idealized systems without pinning. In real systems one usually has additional extrinsic pinning, e.g. due to edge roughness, defects or the geometry of the sample[52]. It enters the 1D model via the pinning potential, V_{pin}. This leads to a finite measurable critical spin drift velocity, u_c.

Similar to the field-induced motion behavior, the velocity increases for the non-adiabatic STT linearly until the WB is reached at the velocity[32]

$$u_{\mathrm{WB}} = u_c \frac{\alpha}{\beta - \alpha}. \tag{2.23}$$

For larger $\mathbf{u}$, the velocity drops ($\beta > \alpha$) or increases ($\beta < \alpha$) again, until the velocity converges to the final average velocity[32]

$$\langle v_{\mathrm{DW}} \rangle = \frac{1 + \alpha\beta}{1 + \alpha^2} u. \tag{2.24}$$

Later, in chapter 6 we will perform combined field- and current-induced DW depinning experiments, where additionally also a fixed in-plane field will be applied to the sample in order to change the DW's internal spin-texture. This will again change the DW dynamics. In particular it will shift the WB towards higher current values, as studied by e.g. O. Boulle et al. and A. Thiaville et al.[19,53]. We will elaborate more on this in the next section, after we have introduced the concept of the SOTs. We want to mention here, that given the large pinning potential of the Hall cross that we will later use for the depinning experiments in chapter 6, we are typically always in the high-current regime ($u > u_{\mathrm{WB}}$), which is also sometimes called as the flow-regime.

However, as discussed above, the non-adiabatic STTs significantly alter the dynamics of the DW. In particular, the critical current density and the velocity of the DW may depend strongly on its amplitude (see Fig. 2.5 (b)). Therefore many research group were looking in the last decade for material systems exhibiting high values of β, since these were thought to be good candidates for fast DW motion. It was found, that especially systems with high perpendicular magnetic anisotropy (PMA) and large SOC usually also have large β values. We will introduce these two concepts in more details in the following two sections.

2.5 Perpendicular magnetic anisotropy

In large magnetic thin films the magnetization lays usually inside the film plane of the system, which is due to the minimization of dipolar energy (see Fig. 2.6). For these systems, exhibiting

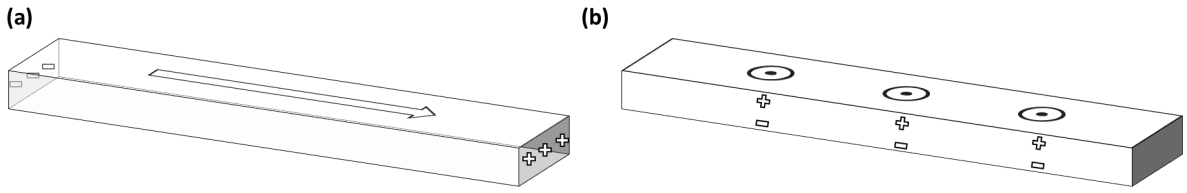

Abbildung 2.6: Illustration of a magnetic system exhibiting (a) in-plane and (b) out-of-plane magnetic anisotropy. The arrows indicate the magnetization inside the sample. + and − indicate positive and negative surface charges, respectively.

in-plane magnetic anisotropy (IMA), the DW widths are typically relatively large.

In the past there was a growing interest in systems where the magnetization is pointing out of the film plane exhibiting a PMA[54]. In these systems the width of the DW, Δ, is typically between of 1 and 10 nm. This is about one or two orders of magnitude smaller compared to systems with IMA ($\Delta \approx 100$ nm). Additionally, observables, such as the DW motion velocity have been found to be much faster for similar applied magnetic fields or current densities and the motion it self is more stable compared to DW motion in IMA systems. All these attributes make PMA materials very attractive for a potential application in e.g. racetrack memory type storage device technology, given their potentially larger storage density, faster reading and faster writing times combined with a in general more deterministic behavior.

The physical reason of an out-of-plane anisotropy in e.g. FM/Oxide systems such as Fe/MgO[55] or CoFeAl/MgO[56] bi-layers is attributed to hybridization of the Fe or Co 3*d*-orbitals withe the O 2*p*-orbitals, respectively.

Although earlier experimental studies also indicated the presence of a PMA at the interface in Pt/Co/MOx (M = Al, Mg, Ta and Ru) trilayer structures[57,58] and in Pt/CoFeB/MgO[59], these structures always contained Pt in direct contact with ferromagnetic transition metals to stabilize the perpendicular anisotropy, which means the origin of the anisotropy is still unclear.[60]

To attain perpendicular anisotropy, a number of material systems have been explored as electrodes. A good review can be found e.g. in[54]. However, it is a challenge to find a material that satisfy in parallel high thermal stability at a reduced dimensionality, efficient current-induced magnetization switching[61] and a high tunnel magnetoresistance (TMR) ratio[62–64], all at once. If realized, it would be very promising for the application in RTMDs.

In this thesis, we investigate the HM/FM/Oxide multilayer stack, Ta/CoFeB/MgO, which has been found to be a good candidate exhibiting all the stated attributes and additionally exhibits also PMA[60,65–68]. The anisotropy of PMA systems is typically described phenomenologically

by an effective (uni-axial) anisotropy, which combines the bulk, interface and shape anisotropy energy densities, as[67]:

$$K_{\text{eff}} = K_b + \frac{K_i}{t_{\text{FM}}} - \frac{1}{2}\mu_0 M_s^2. \tag{2.25}$$

Here, K_b is the bulk anisotropy energy density, K_i represents interface anisotropy energy per unit area and t_{FM} represents the thickness of the FM layer. The last term models the shape anisotropy due to the demagnetizing field. One can see from Eq. 2.25, that depending on the thickness of the FM layer, K_{eff} can become either positive or negative. In the case of large interface anisotropy, which occurs for very thin layers, K_{eff} becomes positive and exhibits PMA. On the other hand, if t_{FM} is very thick, K_{eff} can become negative, which describes a system with IMA.

2.6 Spin-orbit torques

In the last years, beginning with the publication by Miron et al. in 2011[69] and Liu et al. in 2012[65], ultra-fast CIDWM and ultra-efficient current-induced magnetization switching has been observed in several PMA-HM/FM/Oxide systems.

Two main current-induced effects are considered to explain these observations in these systems, namely the ISGE[70–73] and the SHE[74–76].

Both, are relativistic effects and are generated when a charge current is applied to materials exhibiting a strong SOC. Due to their dissimilar multilayer stacking, HM/FM/Oxide systems naturally exhibit SIA. In particular, the magnetic layer, typically only about a nanometer thick, is then in contact with a non-magnetic heavy metal layer, which exhibits a strong SOC due to its high atomic number[18,20,65,77–80].

In the following we will explain the ISGE and the SHE in more details and discuss how they generate the SOTs.

2.6.1 Inverse spin-galvanic effect

Rashba spin-orbit coupling

In systems with a high symmetry axis an energy term in the Hamiltonian linear with the electron momentum, $\boldsymbol{p} = \hbar\boldsymbol{k}$, with $\boldsymbol{k}$ being the wave-vector of the electron inside a solid, can be generated. This has first been shown by Y. A. Bychkov & E. I. Rashba[70] for two-dimensional electron gases (2DEGs) in non-magnetic semiconductor crystals, but also applies for magnetic multilayer metallic systems with SIA, such as our HM/FM/Oxide multilayer system. Considering first a single electron in a simple Rashba model, the so-called Rashba Hamiltonian then reads[73]:

$$\mathcal{H}_{SO} = \alpha_R(\boldsymbol{k} \times \hat{\boldsymbol{z}}) \cdot \boldsymbol{\sigma}, \tag{2.26}$$

where α_R is the Rashba SOC constant and $\boldsymbol{\sigma} = (\sigma_x, \sigma_y, \sigma_z)$ represents the Pauli spin-matrices. Eq. (2.26) describes the locking of the electron's spin to its momentum vector, being always

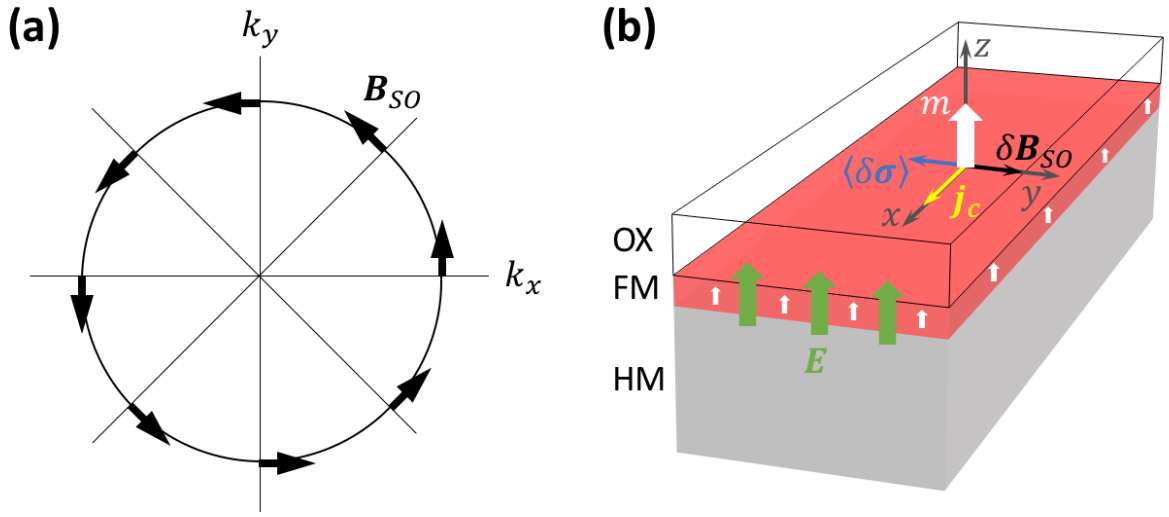

Abbildung 2.7: (a) Illustration of the Rashba SO effective field in k-space, $\boldsymbol{B}_{SO}(\boldsymbol{k})$. (b) Illustration of the resulting inverse spin galvanic effect in a HM/FM/Oxide multilayer system. (Adapted from Ref.[73]).

perpendicular to the direction of motion. The Rashba Hamiltonian can also be seen as describing a Zeeman-like interaction between the spin and an effective SO magnetic field $\boldsymbol{B}_{SO}$[73]:

$$\mathcal{H}_{SO} = -\boldsymbol{m} \cdot \boldsymbol{B}_{SO} = \mu_B \boldsymbol{\sigma} \cdot \boldsymbol{B}_{SO}, \tag{2.27}$$

whereby $\boldsymbol{m} = -g\mu_B \boldsymbol{S} \approx -\mu_B \boldsymbol{\sigma}$ is the magnetic momentum operator of the electron and $\boldsymbol{B}_{SO} = \boldsymbol{B}_{SO}(\boldsymbol{k})$ is always oriented perpendicular to the electron's wave-vector, as illustrated in Fig. 2.7 (a).

This effect can be understood e.g. by considering that the SIA generates a non-centro-symmetric crystal-field potential, V, which leads to a static electric field, $\boldsymbol{E} = -\boldsymbol{\nabla} V$, that points in the direction of high symmetry (as shown in Fig. 2.7 (b) in case of a HM/FM/Oxide multilayer system).

If the electrons move in a direction perpendicular to that high-symmetry axis (e.g. in the $-\hat{\boldsymbol{x}}$ direction in Fig. 2.7 (b)), the electric field can be transformed in the rest frame of the moving electron into the above mentioned effective SO magnetic field. When transforming back into the laboratory's reference frame, this yields[73]

$$\boldsymbol{B}_{SO} = -\frac{\boldsymbol{v} \times \boldsymbol{E}}{2c^2} = \frac{\hbar \boldsymbol{k} \times \boldsymbol{\nabla} V}{2m_e c^2}, \tag{2.28}$$

whereby c is the speed of light, and m_e is the mass of the electron.

In the case of SIA, the conduction electrons experience next to electrostatic nuclear potential, V_{nuc}, additionally a macroscopic interface potential, V_{int}. By combining Eq. (2.27) and (2.28), the SO Hamiltonian can then be written more explicitly as[73]

$$\mathcal{H}_{SO} = \frac{e\hbar^2}{4m_e c^2} \boldsymbol{\sigma} \cdot [\boldsymbol{k} \times \boldsymbol{\nabla}(V_{\text{nuc}} + V_{\text{int}})]\,. \tag{2.29}$$

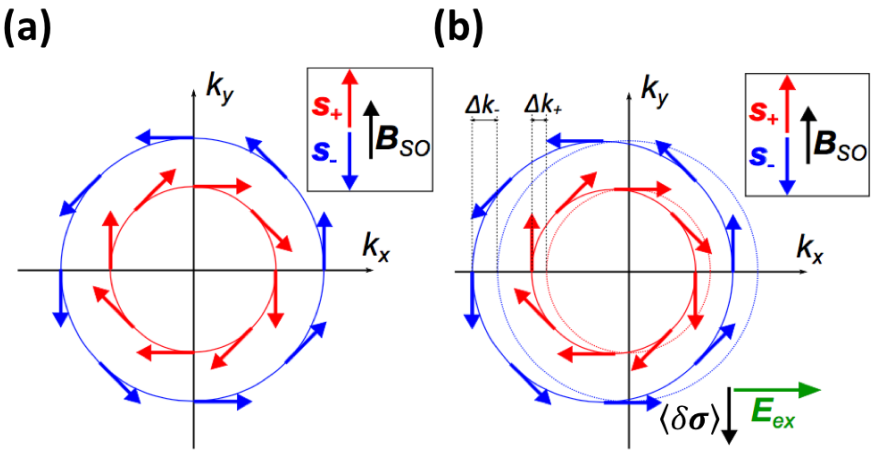

Abbildung 2.8: (a) Illustration of a shifted Fermi contour in a 2DEG Rashba system due to an externally applied electric field, E_{ex}. (Adapted from Ref.[72,73,81]).

In this sense, the Rashba Hamiltonian can be maximized either by using materials with large atomic numbers, leading to a large nuclear potential V_{nuc} or otherwise, for systems consisting e.g. of very dissimilar materials to high potential differences at the interface(s), leading to a large V_{int}.

Inverse spin-galvanic effect

In the previous subsection we have discussed how SOC in a system with SIA can lead to a term linear in $\boldsymbol{k}$ in the system's Hamiltonian and that this can be interpreted as an effective SO magnetic field, $\boldsymbol{B}_{SO}$, acting on the electron's spins. Now we discuss the consequences of this on transport properties.

First, we consider a non-magnetic 2DEG with Rashba SOC. The Hamiltonian reads[73]

$$\mathcal{H} = \frac{\hbar^2 k^2}{2m_e^\star} + \alpha_R(\boldsymbol{k} \times \hat{\boldsymbol{z}}) \cdot \boldsymbol{\sigma}, \tag{2.30}$$

with $m_e^\star$ being the effective electron mass. The eigenvalues of this Hamiltonian then yields[73]

$$\epsilon_{\pm,\,\boldsymbol{k}} = \frac{\hbar k^2}{2m_e^\star} \pm \alpha_R |k|, \tag{2.31}$$

which is a typical quadratically shaped energy dispersion, that is linearly shifted in opposite directions for spins parallel (+) or anti-parallel (-) to the SO magnetic field, $\boldsymbol{B}_{SO}$, due to the Rashba SOC. The splitting of the two spin-subbands leads to a different Fermi wave vector, $\boldsymbol{k}_F$ and different Fermi contours, ϵ_F, for the two different spin-states at the Fermi level. Fig. 2.8 (a) shows the Fermi contours and spin quantization directions of the two spin-subbands at equilibrium[72,73]. In the absence of current the total spin-polarization averages out in each branch, even though the direction of $\boldsymbol{k}$ and the spin orientation are still related.

Next, we consider the case where an external electric field, $\boldsymbol{E}_{ex}$, is applied in the low-symmetry-axis-directions of the system, e.g. into the $\hat{\boldsymbol{x}}$-direction, leading to a current flow, $\boldsymbol{j}_c$. Since $k_{F,+} \neq k_{F,-}$ for these crystallographic directions, the charge current effectively will lead to an asymmetric shift $\Delta k_+ \neq \Delta k_-$ of the Fermi contours for spin (+) and spin (−) electrons, as illustrated in Fig. 2.8 (b). This produces a net out-of-equilibrium spin in-balance in the system, which can be described in terms of an average spin density, as[73]:

$$\langle \delta\boldsymbol{\sigma} \rangle \approx -\frac{\alpha_R m_e^\star}{e\hbar\epsilon_F} j\hat{\boldsymbol{y}}. \tag{2.32}$$

with a net spin-polarization oriented in the $-\hat{\boldsymbol{y}}$-direction. This is called the ISGE[73] or Edelstein effect[71], which describes that a charge current flow in a system with a broken inversion-symmetry exhibiting Rashba SOC produces a net out-of-plane spin polarization. This effect is reciprocal to the spin galvanic effect (SGE), where a spin current flowing in a system with Rashba SOC gives rise to a charge current flow[72].

Spin-torque induced by the ISGE

The out-of-equilibrium spin-density, $\langle \delta\boldsymbol{\sigma} \rangle$, generated by the ISGE described above, is present only highly localized at the interface. In our system, it will couple to the local magnetization texture in the FM layer, via the *s-d*-exchange interaction, J_{sd}. This will produce a torque on the local magnetic moments, which can be described by an effective SO magnetic field, $\delta\boldsymbol{B}_{SO}$, associated with the out-of-equilibrium spin-density[73]:

$$\delta\boldsymbol{B}_{SO} = J_{sd}\frac{\langle \delta\boldsymbol{\sigma} \rangle}{M_s} = -\frac{\alpha_R m_e^\star}{e\hbar M_s} P j(\hat{\boldsymbol{z}} \times \hat{\boldsymbol{j}}). \tag{2.33}$$

The generated torque then reads:

$$\boldsymbol{T}_{\mathrm{ISGE,FL}} = \hat{\boldsymbol{M}} \times J_{sd}\langle \delta\boldsymbol{\sigma} \rangle = \frac{\alpha_R m_e^\star}{e\hbar} P j(\hat{\boldsymbol{M}} \times \hat{\boldsymbol{y}}) \equiv T_{\mathrm{ISGE,FL}} \hat{\boldsymbol{M}} \times \hat{\boldsymbol{y}}, \tag{2.34}$$

which is odd in the magnetization vector, $\boldsymbol{M}$, representing a FL-torques.

So far, we have discussed the ISGE only for the ideal case of quadratic single electron bands, which is only valid for a simple interface-scenario. However, the HM/FM/Oxide systems, that we want to investigate in this thesis are more complex. Typically they have multiple bands participating in the electron transport process under current. Therefore a more advanced treatment of the Rashba SOC and the induced ISGE has to be taking into account. This leads e.g. to additional inter- and intra-band contributions and to an additional possible anti-damping (AD)-like torque:

$$\boldsymbol{T}_{\mathrm{ISGE,AD}} \equiv T_{\mathrm{ISGE,AD}} \hat{\boldsymbol{M}} \times (\hat{\boldsymbol{y}} \times \hat{\boldsymbol{M}}) \tag{2.35}$$

with a symmetry even in the magnetization vector, $\hat{\boldsymbol{M}}$, as discussed recently in the literature e.g. by H. Li et al.[82].

Furthermore, Kurebayashi et al. have identified in the SIA ferromagnetic semiconductor (Ga,Mn)As another contribution leading to an AD-like torque[83]. Here, the origin of the torque was attributed to the intrinsic *Berry curvature*[80,83–86] of the material.

The Berry curvature is also the origin of the intrinsic contributions of the SHE in non-magnetic heavy metals, which intrinsically links both effects. We will discuss the SHE in more details in the following subsection.

2.6.2 Spin Hall effect

In 1971 M. Dyakonov and V. Perel were the first to propose the spin-analog of the charge carrier Hall effect[74], which was later called as the SHE[75]. The SHE describes the phenomenon that a charge current, $\boldsymbol{j}_c$, flowing through a conducting material with strong SOC, such as our HM-layer, induces a spin current, $\boldsymbol{j}_s$, which is flowing in a transverse direction with respect to the current direction and has a certain spin-polarization, that is always perpendicular to the plane defined by $\boldsymbol{j}_c$ & $\boldsymbol{j}_s$. Additionally, this will lead to a highly localized spin accumulation, $\delta\boldsymbol{\sigma}$, towards the edges of the conductor, which then eventually diffuses into neighboring layers, such as the FM layer in our system. The effect is illustrated schematically in Fig. 2.9.

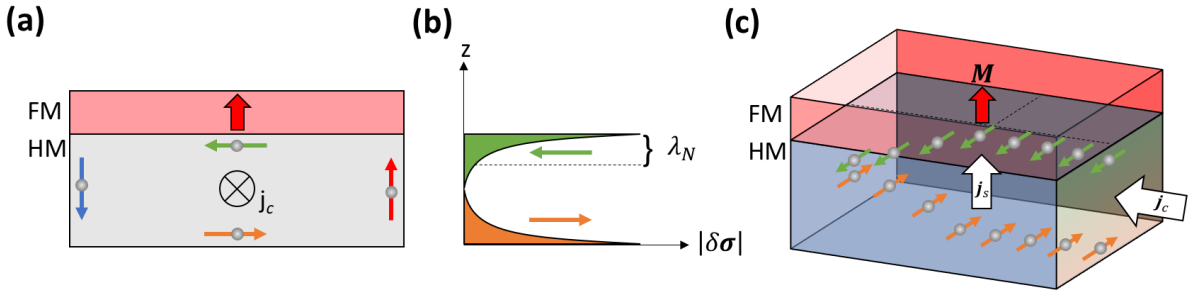

Abbildung 2.9: Illustration of the SHE. (a) An unpolarized charge current, $\boldsymbol{j}_c$, generates a spin current, $\boldsymbol{j}_s$, leading to a polarized spin-accumulation, $\delta\boldsymbol{\sigma}$, towards the edges (highlighted in red, green, blue and orange arrows for spin-up, -left, -down and -right, respectively). The view here is along the current axis, ($j \parallel \hat{\boldsymbol{x}}$). (b) Due to short diffusion lengths λ_N in heavy metals, such as Ta and Pt, thin films can be used to generate highly localized spin-accumulations (e.g. $2-3$ nm) in the vicinity of the surface/interface. (c) Perspective-view of the SHE generating a spin-current, $\boldsymbol{j}_s$, flowing in the $+\hat{z}$-direction, transverse to $\boldsymbol{j}_c$ and with a spin-polarization according to (a) shown with green and orange arrows. Adapted from Ref.[87].

Typically, the link between an injected charge-current and the generated spin-current is given by

$$\boldsymbol{j}_s^y = \theta_{SHE}\frac{\hbar}{2e} j_c \hat{\boldsymbol{z}}, \tag{2.36}$$

where θ_{SHE} is the so-called spin Hall angle (SHA), which describes the spin-charge-conversion efficiency. The superscript, y, indicates the orientation of the spin-polarization. Depending on the

material, the SHA can have a positive or negative sign and can reach typically values up to a few tens of percent[76]. For the material system used in this thesis, Ta/CoFeB/MgO, one generally expects a large SHE generated in the strong SOC Ta-layer, which was found to have typically a negative SHA of about 10%[76] and results in a polarization-symmetry as illustrated in Fig. 2.9 (a).

Microscopically, the SHE can be connected with the anomalous Hall effect (AHE), that is another Hall type transport phenomenon, which describes how an electric field applied to a magnetic material induces a charge current flowing in a transverse direction to both, the electric field and the magnetization direction in the system. The strength of the AHE effect, as well as of the SHE is typically a function of one intrinsic and two extrinsic contributions induced by SOC. The intrinsic contribution depends on the specific band-structure of the material. The two extrinsic contributions are the so-called *skew-scattering* and *side-jump-mechanism*. All three contributions add to both, the total Hall- and spin-Hall-conductivity and can be discussed in an analog way. These microscopic models are not described further here, but instead in section 2.7 of this thesis or in broad details e.g. in[76,85].

Unlike the normal, anomalous and quantum Hall effect, the SHE does not generate a transverse electrical voltage, which made it at first hard to detect experimentally. It took almost 30 years, until 1999, when J. E. Hirsch proposed a setting to detect the SHE experimentally[75]. The SHE was finally observed a decade ago, first optically[88,89] and then also electrically[90]. Since then, the SHE and its reciprocal effect, the inverse spin Hall effect (ISHE) are already widely in use in semiconductor physics, as well as in non-magnetic metals[76].

Very recently, the SHE became also highly relevant in the field of magnetic DW motion in HM/FM/Oxide hetero-structures, as introduced in the beginning of section 2.6. T. Tanaka et al.[91] studied the intrinsic spin Hall conductivity (SHC) theoretically in various $5d$ transition metals, especially Ta, W & Pt among others and in $4d$ transition metals (Ru, Pd, etc.) based on a multi-orbital tight-binding model. They found in particular a huge positive SHC in Pt and Pd and a huge negative SHC in e.g. Ta and W. Futhermore they found that the SHC changes smoothly with the electron number $n = n_s + n_d$ of the different s & d-orbitals, regardless of changes in the crystal structure.

According to Ref.[76,91], we can expect for Ta, which we use in this thesis, as part of our Ta/CoFeB/MgO multilayer stack, that both, the intrinsic contribution from the band-structure and the side-jump mechanism to be dominant.

L. Liu et al.[65] observed experimentally a giant SHE in β-Ta, that generates spin currents intense enough to induce efficient spin-torque switching of ferromagnets at room temperature. This can be useful e.g. for a three-terminal device[92,93] that uses current passing through a high conductivity underlayer with large SOC, which has been brought into contact with a FM layer. In the following subsection, we want to discuss how the SHE-generated spin-current can give rise to the SOTs that act on the FM layer and can potentially explain the above mentioned observations.

Spin torque induced by the SHE

In a HM/FM bilayer system, where the HM-layer exhibits strong SOC and the SHE is generated, we are in particular interested in the spin accumulation towards the HM/FM interface. Considering, Ta, the charge current flowing e.g. in the $-\hat{\boldsymbol{x}}$-direction, and the layer stacking in the $+\hat{\boldsymbol{z}}$-direction, as illustrated in Fig. 2.9 (c), then the spin-current $\boldsymbol{j}_s \parallel +\hat{\boldsymbol{z}}$ will lead to a spin-accumulation $\delta\boldsymbol{\sigma} \parallel +\hat{\boldsymbol{y}}$ at the HM/FM interface, which diffuses into the FM-layer. In the FM-layer, $\delta\boldsymbol{\sigma}$ couples to the local magnetization texture, $\boldsymbol{M}(\boldsymbol{r})$, via the *s-d* exchange interaction. For simplicity, we consider first a homogeneous magnetization texture in the FM layer with $\boldsymbol{\nabla} \cdot \boldsymbol{M} = 0$, forming the magnetization macro-vector, $\boldsymbol{M} = M_s\hat{\boldsymbol{z}}$. This simplifies Eq. (2.17) and one can write the corresponding LLG-equation, including the coupling of the spin-accumulation to $\boldsymbol{M}$, as[94,95]:

$$\frac{d\boldsymbol{M}}{dt} = -\gamma\boldsymbol{M} \times (\boldsymbol{H}_{\text{eff}} + J_{sd}\delta\boldsymbol{\sigma}) + \alpha\boldsymbol{M} \times \frac{d\boldsymbol{M}}{dt}. \tag{2.37}$$

Here, J_{sd} is the *s-d* exchange constant and $\boldsymbol{H}_{\text{eff}}$ contains all other effective fields acting on the magnetization, such as the external, anisotropy and demagnetizing fields. The second term on the right describes the usual Gilbert damping, as discussed in section 2.4. Note, that the new current-induced term, $J_{sd}\delta\boldsymbol{\sigma}$, enters here as an effective field, that acts on a homogeneous magnetization texture. This should be seen in contrast to the classical current-induced STT inside the FM-layer, where the current-induced adiabatic and non-adiabatic STT terms are only present for a non-vanishing magnetization gradient ($\boldsymbol{\nabla} \cdot \boldsymbol{M} \neq 0$), which is given for magnetic DWs or the spin transfer between two non-collinear magnetic layers, separated by a non-magnetic layer, as discussed e.g. in the original STT proposal paper by J. C. Slonczweski[8].

Next, we analyze the dynamics of the spin-accumulation in more detail. As the spin-accumulation diffuses into the FM layer, the interaction with the (strong) local exchange field causes a systematic rotation of $\delta\boldsymbol{\sigma}$ around $\boldsymbol{M}$, which will lead to a new component of spin accumulation pointing into the $\delta\boldsymbol{\sigma} \times \boldsymbol{M}$-direction, as illustrated in Fig. 2.10 (a). This new component is proportional to the spacial change of the spin-current inside the FM-layer, as described e.g. in[87].

Taking this new term of spin accumulation into account, one can extend the expression for the effective field of the spin-accumulation, $J_{sd}\delta\boldsymbol{\sigma}$, into[94,95]

$$J_{sd}\delta\boldsymbol{\sigma}_{\perp} = a\delta\boldsymbol{\sigma} \times \boldsymbol{M} + b\delta\boldsymbol{\sigma}, \tag{2.38}$$

with a and b being parameters depending on the spin mixing conductance[96,97], as well as on the thickness of the FM-layer[94,95].

This leads to an additional torque term

$$\boldsymbol{T}_{SHE,AD} = -a\gamma\boldsymbol{M} \times (\delta\boldsymbol{\sigma} \times \boldsymbol{M}) \tag{2.39}$$

in Eq. (2.37), which is even in the magnetization and represents an anti-damping-like torque, in contrast to the stationary term

$$\boldsymbol{T}_{SHE,FL} = -b\gamma\boldsymbol{M} \times \delta\boldsymbol{\sigma}, \tag{2.40}$$

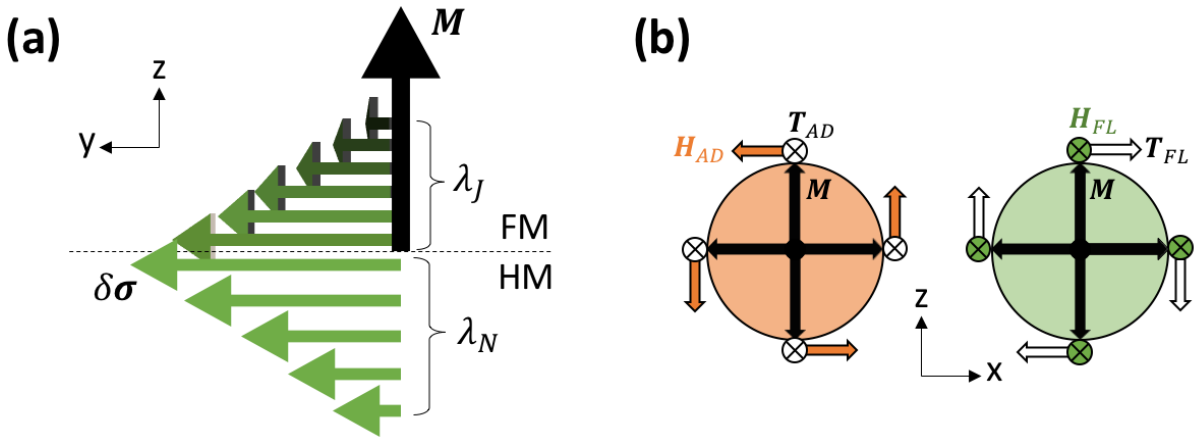

Abbildung 2.10: (a) Illustration of the spin-accumulation $\delta\boldsymbol{\sigma}$ (green arrows) coupling to the local magnetization texture, $\boldsymbol{M}$, (black arrow) in the FM layer. In the vicinity of the NM/FM interface the spin-accumulation becomes maximized within a certain distance λ_N. Inside the FM layer, the strong exchange field with $\boldsymbol{M}$ induces a quick rotation of $\delta\boldsymbol{\sigma}$ around $\boldsymbol{M}$ within the exchange length, λ_J, giving rise to a spin accumulation component that is oriented along $\delta\boldsymbol{\sigma} \times \boldsymbol{M}$ (Adapted from Ref.[87]). (b) Illustration of the AD- and FL-SOTs, $\boldsymbol{T}_{AD}$ & $\boldsymbol{T}_{FL}$ (white arrows) and corresponding effective fields, $\boldsymbol{H}_{AD}$ & $\boldsymbol{H}_{FL}$ (orange & green arrows), acting on the magnetization vector $\boldsymbol{M}$ (red arrows), oriented in the x-z-plane. According to Eq. (2.41) the signs of $\boldsymbol{H}_{AD}$ & $\boldsymbol{H}_{AD}$ depend on the material and the direction of current. Here, the symmetry is illustrated for a Ta/CoFeB/MgO multilayer with the current density, $\boldsymbol{j}_c$, flowing in the positive $\hat{\boldsymbol{x}}$-direction.

which is odd in the magnetization, and represents a FL-torque.

It was found by A. Shpiro et al.[95], that given the strong exchange field, the FL-torque is typically present only directly at the interface, whereas the anti-damping like torque, which originates from the gradient of the spin-current inside the FM layer is maximized after a short distance, λ_J, as illustrated in Fig. 2.10 (a) and then persists throughout the bulk of the FM layer (within the spin-diffusion length).

2.6.3 Discussion of both SOTs

We have discussed in subsection 2.6.1 and 2.6.2, that HM/FM/Oxide multilayer systems exhibit a strong SOC in the HM-layer and naturally consists of a SIA, can give rise to a new class of torques, collectively named as SOTs.

Compared to the classical adiabatic and non-adiabatic STT contributions, which we have discussed in section 2.4, the SOTs have a fundamentally different origin[73].

In case of the classical STTs, a non-vanishing magnetization gradient $(\boldsymbol{\nabla} \cdot \boldsymbol{M}) \neq 0$, e.g. due to a rotation in the spin-texture of a FM or due to a non-collinearity between two magnetic layers, as depicted in Fig. 1.4 are required in order to have a finite adiabatic or non-adiabatic current-induced spin-transfer from one domain into the other.

In the case of the SOTs, the generated spin-densities are also dependent on the magnetization, but are homogeneously present across the HM/FM interface and depend only on the relative angle between the magnetization vector inside the FM layer and the SHE induced spin-accumulation and the non-equilibrium spin density from the ISGE at the HM/FM-interface or its vicinity. Additionally, the SOTs do not transfer spin angular momentum as the STT, but instead transfer orbital angular momentum from the lattice (of the HM) to the spins forming the local magnetization texture in the FM[73].

The adiabatic and non-adiabatic STT exist also in non-SIA or -bulk-inversion asymmetric (BIA) systems. It was seen that the non-adiabatic STT is enhanced in e.g. Pt/Co/AlOx (SIA) systems[98]. This can be related to an increase in the spin-flip rate $1/\tau_{sf}$ due to the strong SOC. The difference between a spin-flip rate enhancement and a proper SOT can be understood by considering the single and many particle electron picture. For the single electron case $\boldsymbol{B}_{SO}$ induces a rotation of the spins around an axis perpendicular to the electric field and $\boldsymbol{k}$. For the multi electron case, the rotation of spins has also a collective component owing to the distribution of $\boldsymbol{k}$ on the Fermi sphere. This leads to a spin decoherence and therefore to a decrease in τ_{sf} and to an increase in the spin-flip rate, correspondingly. This then enhances $\beta_{sf} = \frac{\hbar}{J_{sd}\tau_{\mathrm{sf}}}$ of the classical STT. But this is only valid if a gradient in the magnetization is present ($\boldsymbol{\nabla} \cdot \boldsymbol{M} \neq 0$), as discussed above[73].

However, we have reviewed above, that both effects, the ISGE and the SHE, can simultaneously give rise to a FL- & AD-like torque acting on the magnetization in the FM layer, individually. In the spintronics community, there was recently a notable debate concerning the separation and the definite origin of both underlying effects leading to the new SOTs. Although the debate is not fully finished yet, the AD-like torque has been mostly associated to the SHE and the FL-torque to the combined action of the ISGE and SHE-torque (see e.g.[65,73,80,99–107]).

However, since we do not claim to solve this puzzle here, we can simply summarize both effects within this thesis as an effective SOT torque with

$$\boldsymbol{T}_{\mathrm{eff}} = T_{FL}(\boldsymbol{y} \times \boldsymbol{M}) + T_{AD}(\boldsymbol{M} \times \boldsymbol{y} \times \boldsymbol{M}), \tag{2.41}$$

where T_{FL} and T_{AD} are phenomenological parameters describing the combined action of both SOT contributions acting on a magnetization vector $\boldsymbol{M}$.

In chapter 4, we will experimentally determine the parameters T_{FL} and T_{AD} for our material system by using a *torque magnetometry* measurement method, which is based on a harmonics analysis of the Hall effect signal. This measurement method has been developed recently by U. H. Pi et al.[108] in 2010 and since then has been extended further from several research groups[101,103,109–112]. The newer methods allow in particular to determine the exact angular dependence of the FL- & AD-like torque.

Key experimental publications addressing this are e.g. by K. Garello et al. & X. Qiu et al.[101,111] and very recently by Y. Chen et al.[113]. Among other results, they have found experimentally that the SOT show indeed a complex anisotropic behavior, which is also very different for the FL- & AD-like torque and differs between different multilayer systems, but also for nominal same material systems, but measured by different groups on different exact samples.

The origin for the angular dependence of the SOTs is in general still under debate and needs further theoretical investigations. However, recent theoretical work, that discusses possible

origins of the angular dependencies of the SOTs are e.g. by P. M. Haney et al.[107], K.-S. Lee et al.[114] and C. O. Pauyac et al.[115]. At first, there exists naturally an angular dependence given by the cross products in equation 2.41. Additionally, there has also been discussed a strong angular dependence of Rashba contributions to the torques because of anisotropic spin relaxation rates. It appears e.g. that the strength of the Rashba torque and its symmetry is related to the sample's geometry and dimension[115]. K.-S. Lee et al.[114] argued, that the nontrivial angular dependence of the FL-torque is related to the Fermi surface distortion, determined by the ratio of the Rashba SOC to the exchange interaction. On the other hand, the AD-torque acquires nontrivial angular dependence when the Rashba SOC is comparable to or stronger than the exchange interaction. Then the angular dependence is related to the combined effects of Fermi surface distortion and Fermi sea contribution. The exact disentanglement of the different possible origins of the SOT anisotropies is beyond the scope of this thesis. Instead we will focus more on the experimental methods.

Previous to this thesis, there were reports of different torque magnetometry methods in the literature[101,103,108,111,112], which differ slightly in the exact measurement scheme, the analysis procedure and their particular angular regime they are designed for. It is one of the key goals of this thesis to test these different methods on a single sample experimentally and compare how their individual results eventually match to each other. This will be discussed further in more details in the experimental chapter 4 of this thesis.

The exact knowledge of T_{FL} & T_{AD} in a material, and especially their complex angular dependence, $T_{FL}(\theta,\ \phi)$ & $T_{AD}(\theta,\ \phi)$, as a function of polar and azimuthal angle is crucial in order to analyze the DW dynamics in a given HM/FM/Oxide system further within e.g. numerical simulations or analytically models, such as the above introduced 1D model. This is, because a DW inherently consists of spins, pointing in various directions, across the transition from one domain to another. This will result in a superposition of all acting torques, if one wants to describe the current-induced motion of a complex magnetization texture.

Next, we want to discuss shortly an example of SOT driven DW motion. From the symmetry of the torques, which are generated by a spin-accumulation pointing in the $\pm\hat{\boldsymbol{y}}$-direction (or the spin current due to the SHE, respectively), it is clear, that they can not cause motion of e.g. Bloch type DWs in PMA systems, where the magnetic moment of the wall is pointing in the $\pm\hat{\boldsymbol{y}}$-direction and is causing the SOT terms in Eq. (2.41) to vanish.

However, Néel type DWs, which have a magnetization texture transforming along the xz-direction, and having a magnetic moment pointing into the $\pm\hat{\boldsymbol{x}}$-direction will indeed experience a SOT torque ($\hat{\boldsymbol{y}} \times \hat{\boldsymbol{m}} \neq 0$) causing the DW to move[18,19]. As discussed in section 2.3.2, especially systems with homo-chiral Néel type DWs are of particular interest for the application in e.g. racetrack memory type devices, since these can be driven in the same direction via the ultra-efficient SOTs (see Fig. 2.11)[18]. Recently it was shown in several studies of HM/FM/Oxide multilayer systems, that homochiral ↑↓- and ↓↑-DWs not necessarily have to move with the same speed ($\boldsymbol{v}_{DW}^{\uparrow\downarrow} \neq \boldsymbol{v}_{DW}^{\downarrow\uparrow}$)[18,81,116]. This asymmetry can be partially explained by the presence of the DMI-field, $\boldsymbol{H}_{DMI}$ at the HM/FM interface. $\boldsymbol{H}_{DMI}$ is pointing typically in $\pm\hat{\boldsymbol{x}}$-direction, which breaks the symmetry (see subsection 2.3.2) and it enters the LLG equation similar as an externally applied in-plane magnetic field. This was discussed theoretically, e.g. by O. Boulle et al. & in A. Thiaville et al.[19,117].

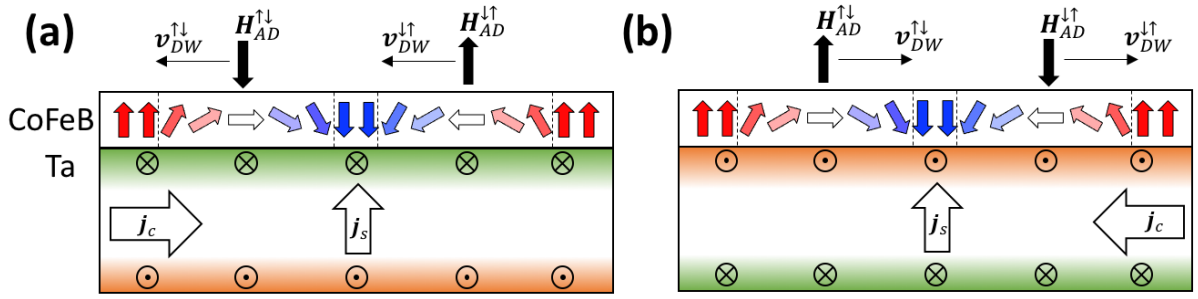

Abbildung 2.11: Illustration of the anti-damping-like SOT originating from the SHE in a Ta/CoFeB bi-layer with negative spin Hall angle acting on an ↑↓ & ↓↑ Néel type DW. The homochirality of both walls will lead to a motion of the DWs in the same direction. (a) & (b) shows how an change of the current polarity will lead to a reversed SHE generation resulting a DW motion in the opposite direction, always against the charge current direction $\hat{\boldsymbol{j}}_c$.

In chapter 6, we will experimentally manipulate the DW's internal magnetization direction with externally applied in-plane magnetic fields pointing into the x- & y-direction and measure simultaneously the corresponding DW depinning efficiencies. This will allow us to test the model and in particular the symmetry of the SOTs and their effects on complex magnetization textures.

2.7 Hall effect in high anisotropy magnetic nanostructures

Since all of our main experimental methods used in this thesis, namely the torque magnetometry (see chapter 4), the DW nucleation detection (see chapter 5) and the DW depinning experiments (see chapter 6), rely on the use of the Hall effect in magnetic systems, we want to give a brief introduction to this effect as well.

In 1879 E. H. Hall[118] discovered that a conducting material will generate a transverse potential difference under the influence of external or internal magnetic fields in a conducting material (see Fig. 2.12) (a). The effect was named after him and the relation of the transverse resistivity and the externally applied magnetic field in a simple non-magnetic conductor, was found to be described by $\rho_H = R_0 H$, with R_0 the normal Hall constant and H the amplitude of an external magnetic field.

In order to describe the Hall effect in ferromagnets, R. Karplus and J. M. Luttinger solved in 1954[119] the kinetic equation, including SOC in the $\hat{\boldsymbol{z}}$-direction for the multi-electron spin-↑ & spin-↓ systems, which are forming a non-vanishing magnetization, $\boldsymbol{M}$. They showed in particular, that under an electric field $\boldsymbol{E} \parallel \hat{\boldsymbol{x}}$ and with spins quantized in e.g. $\hat{\boldsymbol{z}}$-direction, a potential difference proportional to the SOC strength is generated in the direction perpendicular to both the electric field and the initial spin-polarization direction, giving rise to an anomalous Hall velocity of the electrons.

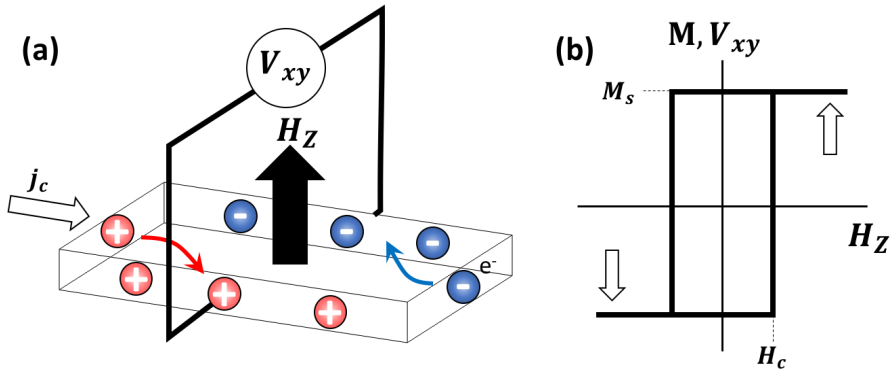

Abbildung 2.12: (a) Illustration of the normal Hall effect in conductors. Under current, j_c, the externally applied out-of-plane magnetic field, H_z gives rise to a transverse motion of the positive and negative charge carriers in opposite direction, causing a charge-in-balance. This can be detected via a measurement of the transverse voltage potential difference, V_{xy}. (b) Typical Hall voltage signal in our FM/HM/Oxide sample. The magnetic anisotropy is so high, that the contribution of the normal Hall effect is negligible small and only the extraordinary Hall effect (EHE) can be observed.

This is true even in the absence of any external magnetic field and only induced by the systems internal magnetic moments experiencing SOC. The total Hall resistivity, ρ_H, can then simply be written as a sum of the normal Hall effect and the so-called anomalous Hall effect[119]:

$$\rho_H = R_0 H + 4\pi R_s M_z = V_{xy}/I_{xx}, \tag{2.42}$$

with R_s the AHE constant proposed by Karplus and Luttinger[119], which is experimentally found to be generally much larger than the ordinary Hall coefficient and e.g. can be strongly temperature dependent. M_z is the out-of-plane component of the internal magnetization, which is perpendicular to the applied current in x-direction, I_{xx}. The total Hall resistivity can then be measured via the generated transverse Hall voltage signal, V_{xy}. In case that no external magnetic field is applied, one can then directly determine the AHE contribution.

However, it turned out that this model is to simple to fully explain realistic systems. This is because the original theory behind R_s only considers inter-band particle-hole excitations, which are intrinsic to the material and depend on the magnetization of the sample, but are independent from eventual electron scattering events with e.g. impurities, grain boundaries or even phonons inside the system. Accordingly, the AHE model described by Karplus and Luttinger is usually called as the intrinsic component of the AHE and the model had to be extended.

In the last 60+ years, certain improvements in the understanding of the Hall effect in condensed matter systems have been made, leading accompanied to a more advanced theoretical description of electron transport phenomena in general. This includes e.g. a sophisticated treatment of the topological nature of the band-structure[76,85,120]. However, in case of the AHE, three types of contributions to the Hall conductivity are typically considered. It is useful to separate them in terms of intrinsic and extrinsic contributions. The extrinsic contributions then again split further into two types. First, the so-called skew-scattering mechanism, which is based on Mott

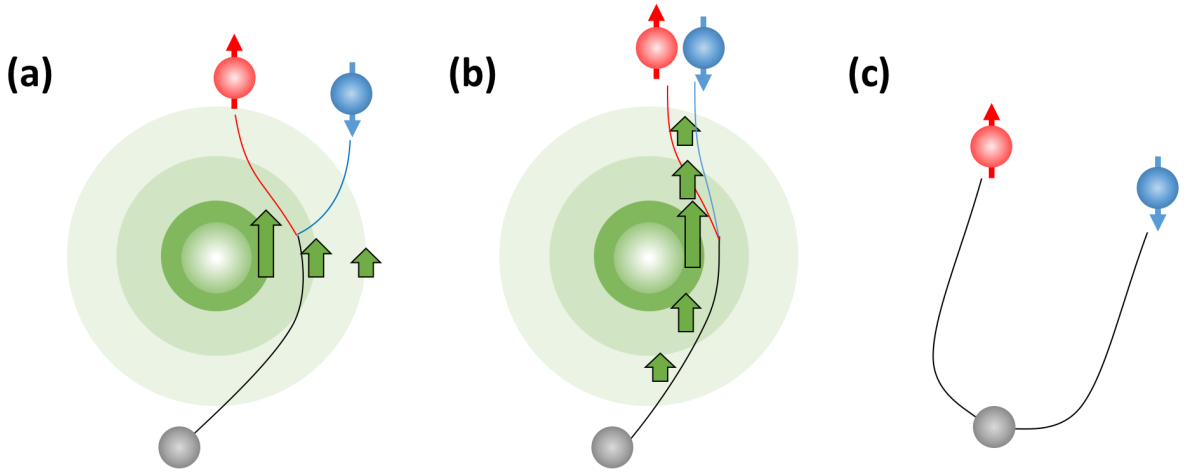

Abbildung 2.13: Schematic illustration of different mechanisms contributing to spin Hall and anomalous Hall conductivities. (a) Spin skew scattering - the spin orbit coupling gives rise to an effective field gradient (indicated by the differences in the green arrows) along the scattering vector at the location of e.g. an impurity (big green sphere), which effectively results in a spin dependence of the scattering angle. (b) Side jump mechanism - the spin orbit coupling results in an effective field gradient along the incoming and out going moment direction, which results upon repeated scattering in a sideway displacement. (c) Intrinsic (spin) Hall effects - due to the band structure there is a spin-dependent transverse velocity, which develops during the acceleration between scattering events.

scattering[121] and second, the side-jump mechanism[122]. All three mechanisms are illustrated in Fig. 2.13.

Both extrinsic mechanisms describe the asymmetric (chiral) scattering of conduction electrons on magnetic or non-magnetic impurities in the system. Typically, these contributions are discussed in transport theory in terms of the Hall conductivity, σ_{xy}^{H}, scaling with respect to the scattering time τ_s of an electron in the system. The total Hall-conductivity then can be written as[85]:

$$\sigma_{xy}^{H} = \sigma_{xy}^{H-int} + \sigma_{xy}^{H-skew} + \sigma_{xy}^{H-sj}, \tag{2.43}$$

with σ_{xy}^{H-int}, σ_{xy}^{H-skew} and σ_{xy}^{H-sj}, the intrinsic, skew-scattering and side-jump contributions, respectively.

As said, σ_{xy}^{H-int} is independent from extrinsic scattering events, yielding $\sigma_{xy}^{H-int} \propto \tau_s^0$. The skew-scattering in contrast scales linearly with the scattering time, $\sigma_{xy}^{H-skew} \propto \tau_s^1$, similar as the longitudinal conductivity, σ_{xx}. The side-jump contribution to the conductivity is considered to have actually itself both, an extrinsic ($\sigma_{xy}^{H-sj-ext} \propto \tau_s^1$) and an intrinsic contribution ($\sigma_{xy}^{H-sj-int} \propto \tau_s^0$), making it a mixed mechanism[76,91]. However, these scattering times are for real samples typically hard to predict, given the arbitrary distribution of e.g. impurities in a system, so that they have to be determined usually experimentally for each sample. Two excellent review paper, where this topic in broadly discussed can be found e.g. in Ref.[76,85].

As described in section 2.2, high anisotropy materials exhibit an easy axis and a hard axis. If no external magnetic field is applied, the magnetization will orient along the easy axis, locked to

one of the magnetic equilibrium states (Up or Down). If one applies an external magnetic field to the sample, this will lead to a square shaped hysteresis loop, where the magnetization state can be switched between the up- or down-state, as depicted in Fig. 2.12 (b). For in-plane magnetic fields, $\boldsymbol{H}_x$ or $\boldsymbol{H}_y$, the magnetization can be tilted into the hard-axis, as used e.g. for the torque magnetometry method in chapter 4.

However, in this thesis we use the Hall effect in our sample for multiple services: First, we analyze the higher-harmonics of the Hall signal within a torque magnetometry measurement in order to determine the exact angular dependence of the FL- & AD-torque as introduced above or in great detail in chapter 4.

Second, we used the Hall effect in chapter 5, to detect the success or failure of DW nucleation experiments. Here, the Hall effect serves as a detector for DWs, which get pinned or even pass a Hall-cross structure after successful nucleation. This is possible because DWs can get pinned easily at Hall-bar geometries. We will introduce this again step-by-step in chapter 5.

Third, we use the Hall effect in chapter 6 in order to detect DW depinning from our nanofabricated Hall cross geometry pinning site. This allows us to systematically determine the effective depinning fields in our sample and with that determine the strength of the current-induced STTs and SOTs on a DW.

3 Material system and experimental setup

In this chapter the material system and the experimental setup used in the thesis will be introduced.

First, we discuss in section 3.1 the deposition of the thin multilayer system and its special treatment in order to tune the magnetic anisotropy from initially pointing in-plane, towards pointing perpendicular to the plane of the thin film.

After that, the PMA thin films are patterned into nanodevices with Hall-bar geometry, which we describe in section 3.2.

Finally, the general experimental cryostat-setup will be described in section 3.3. The exact measurement setups & techniques used for the individual measurements are for a better readability of the thesis, part of the result chapters 4, 5 and 6 and will be shortly introduced in the beginning of each of them.

3.1 Sample fabrication and characterization

Within this thesis we investigate the HM/FM/Oxide multilayer system Ta (5 nm) / $Co_{20}Fe_{60}B_{20}$ (1 nm) / MgO (2 nm) / Ta (5 nm), often abbreviated as Ta / CoFeB / MgO multilayer, which is the main stack we are interested in.

In the full material stack, the top Ta layer is typically assumed to not participate in the magnetization dynamics inside the CoFeB layer, because of the 2 nm insulating MgO layer in between. In our material stack, we use it in order to protect the CoFeB/MgO-layer from beeing subject to further oxidation from the environment.

In order to handle ultra-thin multilayer systems, in our case the multilayer is in total 13 nm thick, one typically deposit it on top of a much thicker substrate material, which is easier to handle. For our samples, a standard Si/SiO substrate is used. It is assumed to not participate in the transport properties, giving its much higher semiconductor resistivity, compared to the metallic Ta and CoFeB layers. However, it was found e.g. by M. Walter[123], who compared the MTJ switching in Si / SiO (bulk) / CoFeB / MgO / CoFeB systems with that of MgO (bulk) / CoFeB / MgO / CoFeB systems, that the use of Si-substrates in their experiments did influence the ultra-fast MTJ switching behavior, they investigated. They found in particular, that the bottom semiconducting Si-substrate can couple as a capacitor to the electrical circuit built by the ferromagnet / insulator / ferromagnet system, which led to certain artefacts in their measurement signals. In their experiments the current is typically sent perpendicular to the film plane and we perform in this thesis measurements with current sent only within the film plane. Additionally their pulse lengths for their switching experiments are much shorter than the ones we use later in

the DW nucleation and DW depinning measurements, we assume that those effects are negligible in our structures.

3.1.1 Deposition and sample quality

The Ta/CoFeB/MgO thin films studied in this thesis were deposited by our industrial project partner B. Ocker from *Singulus Technologies AG*, using a commercial *Singulus TIMARIS/ROTARIS©* sputtering machine. With this, the deposition of all four material layers of the Ta/CoFeB/MgO/Ta multilayer stack can be performed in a single process, where the sample is tilted towards the individual sputtering targets in the machine one after the other. The deposition is performed in ultra-high vacuum, leading to a sub-nm to nm precession of the individual layer thicknesses. After the deposition, the thin films are annealed at high temperature in order to induce PMA, which will be confirmed in subsection 3.1.2. To check the quality of the fabricated multilayer, a Lorentz-transmission electron microscopy (TEM) image was taken and the sample was characterized using secondary ion mass spectroscopy (SIMS)[1]

First, we discuss the Lorentz-TEM image, which shows a cross-sectional view of the annealed thin film with a sub-nm resolution (Fig. 3.1 (a)). In this image, one can recognize a sharp CoFeB/MgO and a less sharp Ta/CoFeB interface. Additionally, one can see a splitting of the top Ta interface, which results from the natural oxidation in air. One can also slightly see the presence of crystalline MgO and CoFeB layers around the interface, but most of the layer results to be polycrystalline. Lastly, one can extract the nominal thicknesses of the different layers, Ta (5 nm) / CoFeB (1 nm) / MgO (2 nm) / Ta (3 nm) / TaO_x (2 nm), which match nicely with the intended ones.

The fact, that the Ta/CoFeB and the CoFeB/MgO interfaces seem to be smeared out in the Lorentz-TEM image, was investigated further by performing SIMS measurements.

With a SIMS measurement the material composition of each individual layer can be detected. For this, the sample is etched continuously under the bombardment of high energetic Ga^+-ions and the sample's constituents are simultaneously detected by the mass spectrometer[124]. Fig. 3.1 (b) shows a SIMS etching curve of the Ta/CoFeB/MgO thin film, whereby the material composition of the sample before and after the annealing process are indicated with empty and filled symbols, respectively (see legend in Fig. 3.1 (b)). In general the composition shows the expected material distribution of the multilayer stack. However, we find that the magnetic materials, Fe (Grey triangles) & Co (green triangles) as well as the B (black circles), indeed are strongly overlapping with the MgO on top (red squares) forming a CoFeB/MgO alloy. Furthermore we find that the B atoms (black circles) seem to be present all over the multilayer, even if they are mostly present at a depth of 6 to 14 nm. By taking into account that Fig. 3.1 (b) is presented in logarithmic scale and the stoichiometric B concentration is only 20 % of the 1 nm thick $Co_{20}Fe_{60}B_{20}$ layer this might not be a large effect and could be explained by a higher sensitivity of the mass spectrometer for B atoms compared to the other materials in the multilayer. Finally we find a trend of B diffusion towards the Ta layers due to the annealing process, which we discuss next.

[1] The actual Lorentz-TEM and SIMS measurements have been performed by our project partners L. Nasi, L. Lazzarini and R. Mantovan, from the IMEM–CNR, Italy[124].

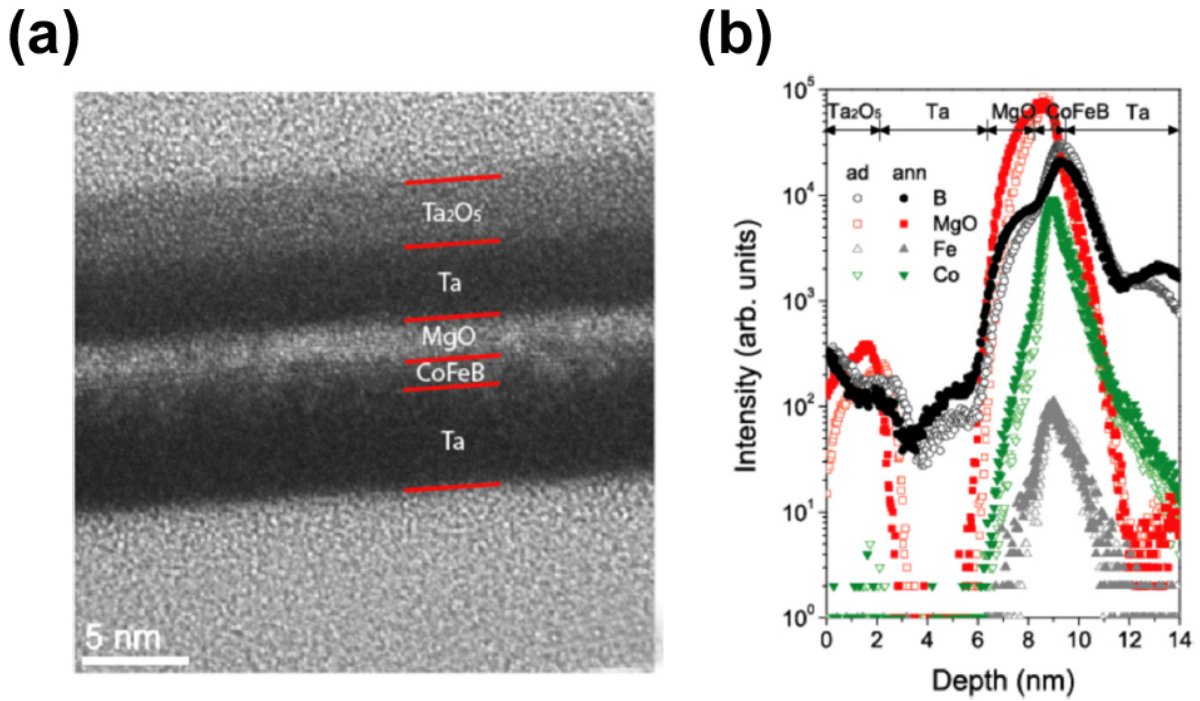

Abbildung 3.1: (a) Lorentz-TEM cross-section image of the Ta (5 nm) / $Co_{20}Fe_{60}B_{20}$ (1 nm) / MgO (2 nm) / Ta (5 nm) stack. The red lines indicate the different layers of the multilayer. (b) SIMS depth profiles of as-deposited (ad) and annealed (ann) structures. Signals related to B (dots), MgO (squares), Fe (up-triangles) and Co (down-triangles) are shown. A strong intermixing of the MgO and the CoFeB layer can be observed. Following the B profile, B diffusion from the CoFeB layer towards the Ta layer (and partially the MgO layer) is evident. For the sake of clarity profiles are aligned at the CoFeB/Ta interface. Secondary ions are collected and the measurement parameters are as reported in Ref. [124].

3.1.2 Magnetic anisotropy

After the deposition, the thin films have naturally an in-plane magnetic anisotropy, as discussed in section 2.5. In order to tune the anisotropy perpendicular to the plane, the sample was annealed for 2 h at 300 °C in vacuum[2]. Afterwards the presence of the PMA is verified by measuring the magnetization of the thin film, using e.g. a superconducting quantum interference device (SQUID).[3]

Fig. 3.2 (a) and (b) show the SQUID magnetic field scans using in the out-of-plane and in-plane direction, respectively. The diamagnetic part of the SQUID signal has already been removed by subtracting the slope of the high-field signal from the measurement data. The measurements yield a coercive field $H_c^{\text{thin film}} \approx 2$ mT (Fig. 3.2 (a)) and an in-plane anisotropy field $H_k^{\text{eff}} \approx (400 \pm 50)$ mT (Fig. 3.2 (b)). This confirms the out-of-plane anisotropy of the thin film after the annealing.

[2]The actual annealing procedure has been performed by our project partner B. Ocker from Singulus Technologies AG.

[3]The actual measurements have been performed together with Tim Zacke and Su-Jung Noh and have been reported also in Tim Zackes diploma thesis [125].

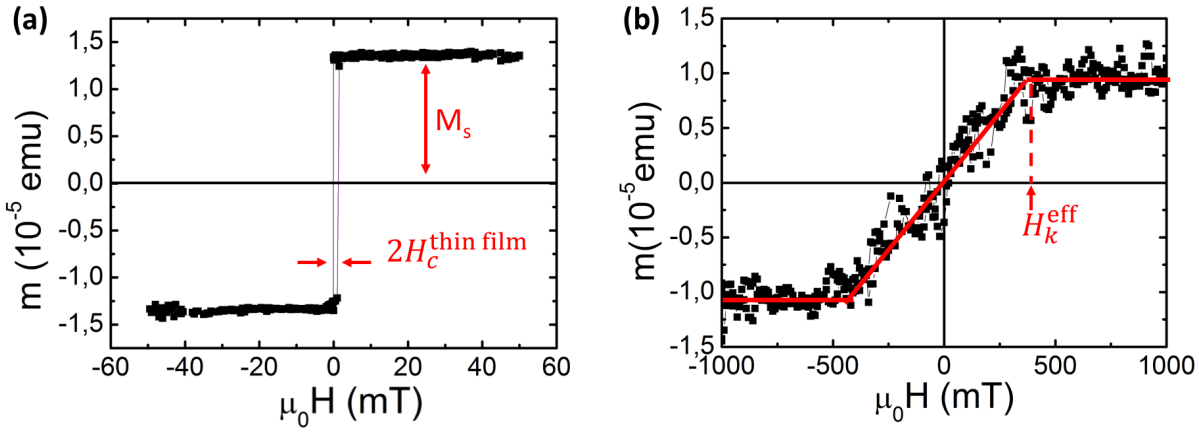

Abbildung 3.2: SQUID hysteresis measurement data for a small un-patterned Ta/CoFeB/MgO thin film sample at 300 K. (a) shows the out-of-plane and (b) the in-plane magnetic field scan confirming the perpendicular anisotropy of the sample after the annealing procedure. Additionally, the coercive field $H_c^{\text{thin film}} \approx 2$ mT, the saturation magnetization $M_s \approx 1.1 \times 10^6$ A/m and the in-plane anisotropy field $H_k^{\text{eff}} \approx (400 \pm 50)$ mT can be determined from these measurements.

The saturation magnetization of the sample can be determined to be $M_s \approx 1.1 \times 10^6$ A/m at room temperature (300 K).

3.2 Nano fabrication and measurement preparations

After the annealing process and the confirmation of proper material properties, the PMA thin films are patterned into nanodevices. For this thesis, these are nanowires with a certain cross-shaped geometry, which is useful in order to measure the Hall-effect (see Fig. 3.3)

The patterning can be done by using standard electron-beam lithography (EBL) processes combined with Argon-ion milling and wet etching techniques. The nanofabrication process for all the samples used within this thesis have been done by our collaborators Karin Garcia from Université Paris-Sud together with Laurent Vila from the SPINTEC group at Université Grenoble Alpes.

Because of that, we describe the process here only very rudimentary, without details on sample handling, exact resist types or developing times etc. However, this section is intended to give the reader a general idea on how our nanostructured samples were lithographically fabricated. The main process steps are illustrated in Fig. 3.4 (a)-(g) and are described in the following text.

First, a thin layer of electron-sensitive polymeric resist is deposited on top of the Ta / CoFeB / MgO / Ta multilayer, as illustrated with the transparent orange layer in Fig. 3.4 (a).

After a development step with an appropriate solvent, certain regions of the polymer (indicated by the orange cross structure in Fig. 3.4 (b)) are exposed by a highly focused electron beam using an EBL machine.

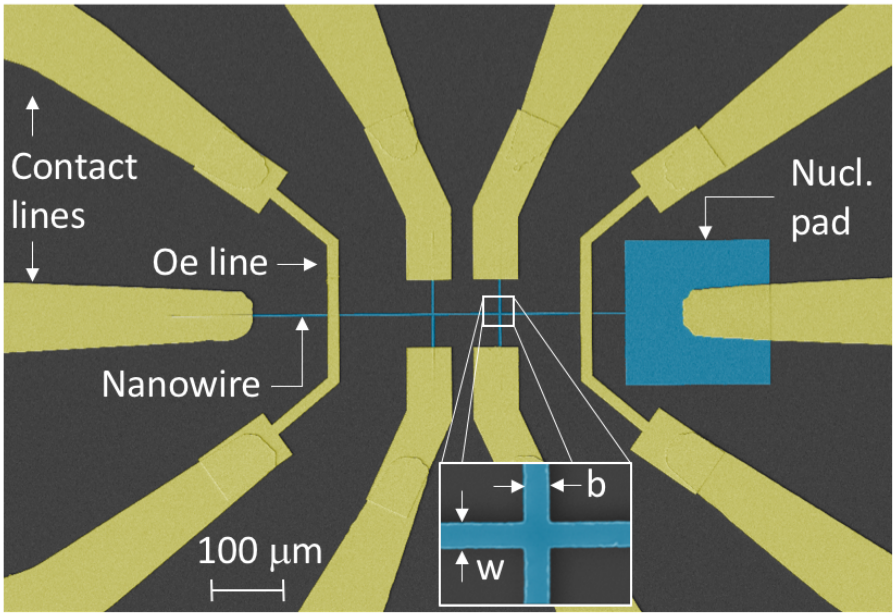

Abbildung 3.3: SEM image of a nanostructured Ta / CoFeB / MgO sample used in this thesis. The multilayer has been patterned into a nanowire (highlighted in blue color) with a nucleation pad (Nucl. pad) and two Hall bars (inset), with dimensions $w = d = 400$nm. On top of the nanowire two Au strip lines (Oe lines) have been deposited (highlighted in yellow color). The nanostructure can be electrically connected via 300 μm × 300 μm Au bond pads (not shown in this SEM image).

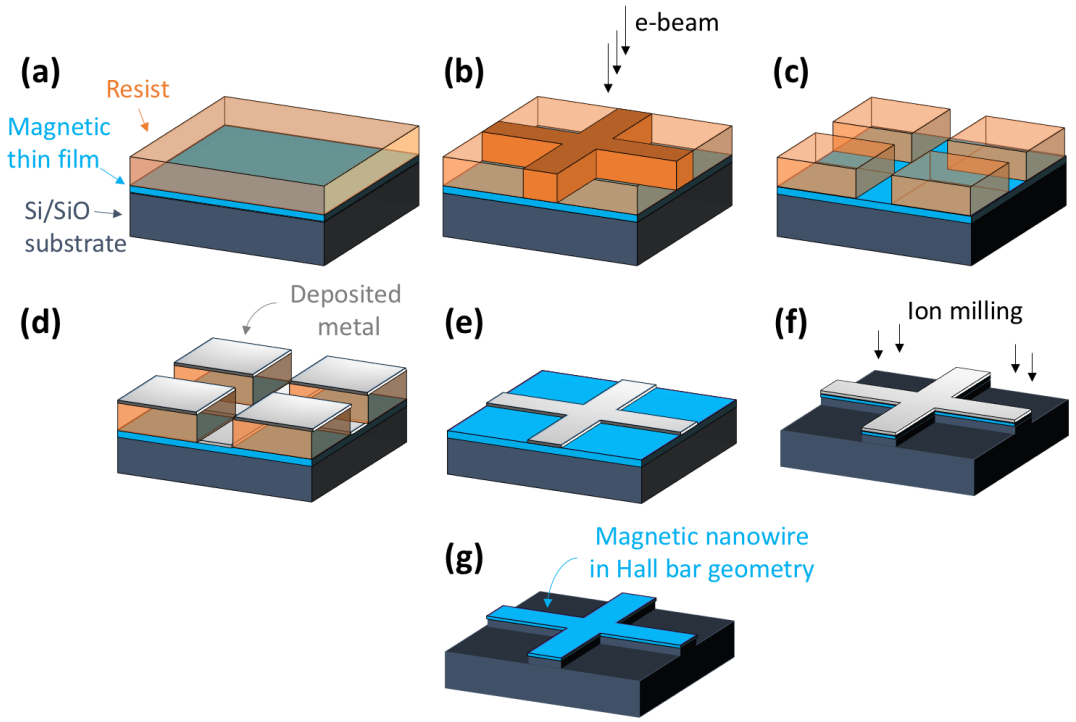

Abbildung 3.4: Illustration of the magnetic nanowire patterning process. Description of the process in the main text.

After the exposure, the resist is developed by using an appropriate solvent. Depending on the resist type, positive or negative, the e-beam exposed regions of the polymeric resist are either been removed or left on top of the sample surface, respectively. As a result a mask out of polymeric resist is defined on top of the magnetic thin film surface. Fig. 3.4 (c) shows the result of a positive resist exposure combined with the developing step, as used for our samples.

Such a mask can then be used either to deposit material on the free areas on top of the sample surface or to pattern devices out of the material stack with the specific shape of the mask.

For our samples, a thin Aluminum (Al) metal layer is evaporated on top of the predefined resist mask, as illustrated in Fig. 3.4 (d).

By using an appropriate solvent, e.g. Acetone, one can now remove all the resist and the metal on top of it from the sample. As a result only the metal layer, directly bonded to the multilayer stack will remain (see Fig. 3.4 (e)).

The next step is to transfer the shape of the patterned Al layer into the multilayer stack. For that, a technique, called Ar ion milling was used. Here, Ar ions are accelerated towards the sample. By impacting it, the surface atoms will be sputtered away. By using a thick enough Al layer previously, the milling time to remove the uncovered magnetic multilayer completely is shorter than the milling time to remove the Al layer, which covers part of the magnetic layer. As a result one gets a structure as illustrated in Fig. 3.4 (f), where the magnetic film is only remaining below the Al layer.

Finally, the Al layer is removed by using e.g. a selective Al wet etching developer and one gets a free nanopatterned structure as illustrated in Fig. 3.4 (g).

Fig. 3.3 shows the corresponding scanning electron microscopy (SEM) image of our real final sample, consisting of a 400 nm wide Ta / CoFeB / MgO nanowire with a 400 nm $\times$ 400 nm Hall cross geometry (see inset of Fig. 3.3) and a so-called DW nucleation pad[4] on the right.

In order to electrically connect this patterned nanodevice to the rest of the experimental setup, a further lithographic process is necessary, where contact lines, that are leading to a few hundert micrometer-sized contact pads, are deposited on top of the nanodevice. For that, one can repeat the steps (a)-(e), illustrated in Fig. 3.4. In order to align the contact lines and contact pads with the nanostructure, one usually adds some sort of alignment marker system during the first fabrication step, which can then be scanned and adjusted to in the second step.

For our sample, the contact lines are made of Ti (5 nm) / Au (150 nm) and are illustrated in Fig. 3.3 with golden color.

Additionally, to the left and to the right of the double Hall cross structure, two 1.4 μm wide stripe lines are deposited on top and perpendicular to the nanowire. These will be used in chapter 5 & 6 as writing elements for DWs.

[4] A DW nucleation pad can be used to inject DWs into the wire at magnetic fields lower than the usual wire coercivity [126,127], but it will not be used within this thesis.

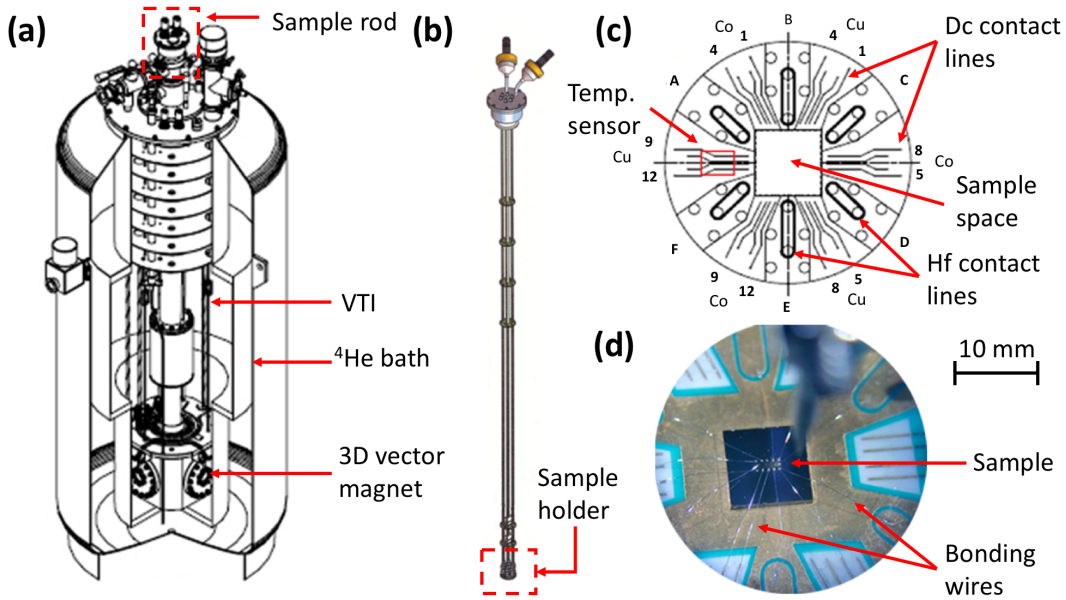

Abbildung 3.5: Illustration of the measurement setup. (a) Schematics of the He4-cryostat setup, equipped with a 3D vector magnet. (b) Unplugged sample rod, consisting of 6 high frequency (Hf) and 24 low frequency lines (Dc). (c) Schematic drawing of the sample holder consisting of a sample space, Hf and Dc contact lines made of Cu and Co and a sample temperature (Temp.) sensor. (d) Microscopy image of the sample, which has been glued to the sample holder and electrically connected via Al bonding wires.

3.3 Experimental measurement setup

All transport measurements presented in this thesis were performed in a ^{4}He-cryostat environment (Fig. 3.5 (a)). With the cryostat the sample temperature can be easily adjusted in a range between 1.2 K and 325 K by using a variable temperature inset (VTI) with a needle valve separating the liquid He bath from the sample space and a heater to warm up the incoming He-gas. To increase the temperature stability the VTI is continuously pumped by a vacuum pump leading to a constant He-gas flow inside the sample space. To monitor and control the temperature, two temperature sensors (*Cernox model CX-1050-SD-1.4L*) are used. The first sensor is used to monitor the VTI temperature and provides the input temperature for a proportional-integral-derivative (PID) control loop running at the temperature controller (*CryoCon model 32B*). The second temperature sensor is used to measure the temperature directly on the sample holder. Additionally, the resistivity of the sample itself was used to measure the sample temperature directly. Depending on the He flow rate into the VTI, we could achieve with this setup a temperature stability of $\Delta T \approx \pm 20$ mK.

Furthermore the setup consists of a superconducting 3D-vector coil magnet (Fig. 3.5 (a)). With this, magnetic fields can be applied up to ±5 T in the $\hat{z}$-direction and up to ±1 T in the $\hat{x}$, $\hat{y}$-directions of the sample. In order to measure the sample inside the cryostat, we glue it on top of a customized sample holder, by using *PMMA* resist[128]. Fig. 3.5 (c) shows a schematics drawing of the sample holder. Electrically, the sample can then be bonded to the sample holder

by using a semi-automatic wire bonding machine (*HYBOND model 572A-40*) and conducting wires, typically consisting of Al or Au.

Next, the sample holder is connected to a vacuum proof sample rod (Fig. 3.5 (b)), which can be connected electrically from outside of the cryostat to the electrical equipment.

The cryostat setup provides 6 high frequency and 24 low frequency connections. The high frequency (hf) connections are made of semi flexible coaxial cables, which are suitable for frequencies up to 18 GHz and for low temperatures. The low-frequency connections are twisted pairs of Cu & constantan ($Cu_{55}Ni_{44}Mn_1$) wires, which are combined to flat band cables, where each twisted pair consists of one signal line and a wire connected to the common ground. To avoid electrostatic discharges (ESD) and thus the destruction of a sample, we use a customized switch box, which has been developed by Jan Heinen and coworkers within his PhD thesis[10]. Furthermore, we wear special electrical conducting anti-ESD clothes (i.e. a coat, a foot and an arm wristlet, which all are connected to the common ground) during the sample handling.

4 Effective field analysis using SOT magnetometry experiments

4.1 Introduction

A method, which allows one to detect the acting current-induced spin-torques in a given system as a function of the magnetization direction $\boldsymbol{m}$ is the so-called *torque magnetometry* method based on a higher harmonics analysis of the anomalous Hall effect[101,103,108,110–112]. In this thesis we apply this method to our nano-patterned Ta/CoFeB/MgO multi-layer sample.

According to the current view on the physics in these type of HM/FM/Oxide multilayer-systems, several spin-torques from different possible origins, are acting simultaneously on the magnetization of the FM layer when a current is flowing across the sample, as discussed in chapter 2. When the sample's magnetization, $\boldsymbol{M}$, is homogeneously pointing in a single direction, i.e. when $\boldsymbol{M}$ is saturated in one directions, there is no net effect of the classical adiabatic and non-adiabatic STTs on the magnetization. These are optimal conditions to measure the recently discovered SOTs, which can be present due to their particular symmetry.

The most prominently considered SOTs in our material system are originating from the ISGE and the SHE, as discussed in section 2.6.1 and 2.6.2. Both mechanisms are supposed to generate a FL- and an AD spin-torque component, $\boldsymbol{T}_{FL}$ and $\boldsymbol{T}_{AD}$.

Additionally, both effects are dependent on the relative orientation of the equilibrium magnetization direction, $\boldsymbol{M}$, with respect to the spin-polarization of the spin-current originating from the SHE and the non-equilibrium spin density, $\delta\boldsymbol{\sigma}$, which is generated at the HM/FM interface due to the ISGE. The vectorial dependencies for the FL- and AD-torque are $\boldsymbol{T}_{\perp} \approx \boldsymbol{M} \times \delta\boldsymbol{\sigma}_{\perp}$ and $\boldsymbol{T}_{\parallel} \approx \boldsymbol{M} \times \delta\boldsymbol{\sigma}_{\parallel}$, respectively. Hereby $\delta\boldsymbol{\sigma}_{\perp} \approx \hat{z} \times \boldsymbol{j}$ and $\delta\boldsymbol{\sigma}_{\parallel} \approx (\hat{z} \times \boldsymbol{j}) \times \boldsymbol{M}$. Considering the current, $\boldsymbol{j}$, to be flowing into the $\hat{x}$-direction this yields $\delta\boldsymbol{\sigma}_{\perp} \approx \hat{y}$ and $\delta\boldsymbol{\sigma}_{\parallel} \approx \hat{y} \times \boldsymbol{M}$ and finally $\boldsymbol{T}_{\perp} \approx \boldsymbol{M} \times \hat{y}$ and $\boldsymbol{T}_{\parallel} \approx \boldsymbol{M} \times (\hat{y} \times \boldsymbol{M})$ (see Fig. 2.10 (b)).

This makes $\boldsymbol{T}_{\perp}$ and $\boldsymbol{T}_{\parallel}$ to act also on uniform magnetization textures, which enables e.g. the possibility to tailor purely SOT driven domain switching to be realized[65]. However, in this chapter we don't want to use the SOTs to switch the magnetization completely, but instead probe the effect of the SOTs on the homogeneous magnetization as a function of its inclination angle θ, since this allows us to determine the anisotropy of the SOTs. Therefore we apply only relatively small current densities of $j \approx 5 - 8 \times 10^{10}\mathrm{A/m}^2$ across the sample, which are chosen to be smaller than the critical current density for switching.

With the torque magnetometry method it is only possible to measure the net effects of the acting torques in the form of effective magnetic fields $\boldsymbol{H}_{\perp} = \boldsymbol{M} \times \boldsymbol{T}_{\perp}$ and $\boldsymbol{H}_{\parallel} = \boldsymbol{M} \times \boldsymbol{T}_{\parallel}$ as we perform vectorial magnetic field scans in three dimensional space. Typically it is enough to perform scans

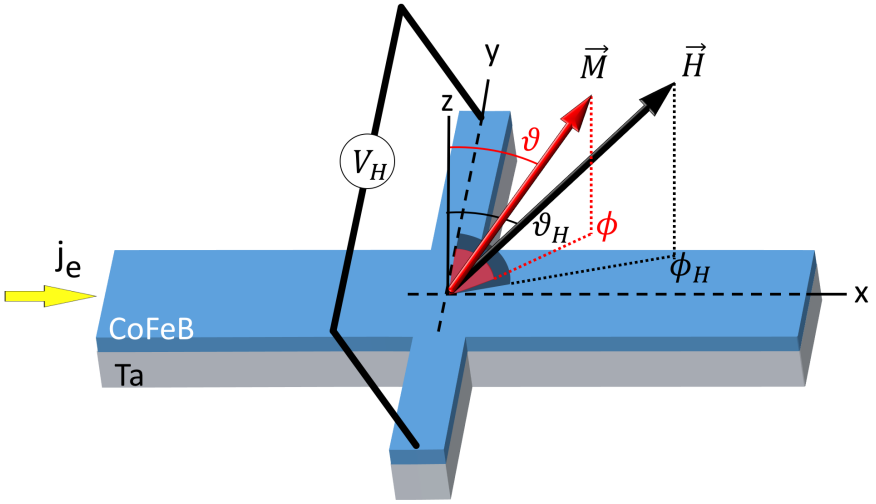

Abbildung 4.1: Schematic illustration of the experimental setup. A Hall bar is patterned from our Ta/CoFeB/MgO magnetic heterostructure. Definitions of the coordinate systems are illustrated together. $\boldsymbol{M}$ denotes the magnetization and $\boldsymbol{H}$ represents the external magnetic field. When a current $\boldsymbol{j}_e$ is applied to the sample the magnetization tilt inside the CoFeB-layer can be detected via the Hall measurement signal V_H.

only in the main symmetry axis of the nanopatterned structure, which are defined to be the zx and zy planes, i.e. planes with $\phi = 0$ or $\pi/2$, in our coordinate system (see Fig. 4.1). All effects for planes with $\phi \neq 0$ or $\pi/2$, can then be superimposed by those in the longitudinal or transverse direction[87,101,109,129].

Experimentally, one can detect the effective magnetic fields generated by the SOTs by measuring the out-of-phase contribution of the second harmonics Hall voltage signal, which is generated as the effective magnetic fields will tilt the magnetization vector out of its equilibrium position (θ_0, ϕ_0). Hereby, θ_0 and ϕ_0 can be derived from minimizing the energy of the system:

$$E = -K_{\text{eff}} \cos^2\theta - K_i \sin^2\phi \sin^2\theta - \boldsymbol{M} \cdot \boldsymbol{H} \tag{4.1}$$

by considering that the equilibrium position fulfills $\partial E/\partial\theta = 0$ and $\partial E/\partial\phi = 0$[110]. Here, $K_{\text{eff}} = K_u - \frac{1}{2}(N_z - N_x)M_s^2$ and $K_i = \frac{1}{2}(N_x - N_y)M_s^2$ in Eq. (4.1) are the effective out-of-plane and in-plane anisotropy constants, with K_u being the uni-axial anisotropy constant in the easy-axis direction. $N_{x,y,z}$ with $\sum_{i=x,y,z} N_i = 4\pi$ are the demagnetization coefficients of the sample including the shape-anisotropy effects and M_s is the saturation magnetization. $\boldsymbol{M} = M_s(\sin\theta\cos\phi,\ \sin\theta\sin\phi,\ \cos\theta)$ and $\boldsymbol{H} = H(\sin\theta_H\cos\phi_H,\ \sin\theta_H\sin\phi_H,\ \cos\theta_H)$ are the magnetization vector and the external magnetic field pointing in $(\theta,\ \phi)$ and $(\theta_H,\ \phi_H)$ direction, respectively and are systematically varied throughout the torque magnetometry measurements.

As described above, it is known that the SOTs present in HM/FM/Oxide multilayer-systems exhibit in general a complex material dependent angular dependence[101,111,114]. In this thesis we show that the effective fields acting on magnetic DWs, which are responsible for the efficiency of their dynamics, require a sophisticated analysis taking into account the full angular dependence of the torques. This should not be surprising, since DWs by definition consist of spins pointing in various directions.

The remainder of this chapter is structured as follows:
In section 4.2 we introduce the torque magnetometry measurement technique in more detail and describe our experimental setup.

Since it is not possible to measure the full polar angular spectrum of the torques with a single torque magnetometry analysis method, we will use three different methods instead. Each of these methods was developed for a particular angular region and requires a slightly different analysis caused by different approximations made in the fitting formalism[101,103,112]. These we name in the following as the *small*, *intermediate* and *large* angle regimes, accordingly to the polar angular regimes they cover, respectively.

Accordingly, in section 4.3 we split the experimental results section for the specific parts into the above mention three angular regimes - subsection 4.3.1 to 4.3.3. In each of these we discuss the changes in the measurement protocol, the resulting measurement results and their individual analysis methods. In this sense the general method section 4.2 will only contain parts that are valid for all three angular regimes.

In subsection 4.3.4 we combine the measurement results for the individual angular regimes in order to obtain the full angular dependence of the effective torque fields and discuss the congruence of the different measurement methods, which has not been addressed before this thesis work in the literature.

Having this, we go a step further and use in section 4.4 the combined SOT effective field dependence obtained for an uniform magnetization macro-vector from section 4.3 and calculate the effective FL- and AD- SOT fields for a more complex spin-texture for the example of a magnetic Néel type DW.

Finally, we use the obtained result for the effective torque fields on a Néel type DW from section 4.4 and calculate in section 4.5 its corresponding effective depinning field in a DW depinning experiment. This allows us later in chapter 6 to compare the theoretical predicted torque efficiencies based on torque magnetometry measurements to the experimental results obtained in real DW depinning experiments.

This comparison has also not been addressed before this thesis work and allows to evaluate the comparability for results obtained with both methods. Most parts of this chapter have been published in a less detailed version in Ref.[130].

4.2 Measurement technique

Following general safety and alignment procedures, the nanostructured Ta/CoFeB/MgO sample in Hall bar geometry is mounted at the center of a 3D-vector magnet inside the He4-cryostat environment, as introduced in section 3.3.

The usage of a 3D-vector magnet is for this measurement of particular advantage, as it allows us to apply an external magnetic field vector, $\boldsymbol{H}$, conveniently into any arbitrary direction in space within the magnet's specifications range and without physically changing the samples orientation nor the setup. This allows us to ramp the magnetic field not only e.g. within the film plane direction or along the out-of-plane axis, but also into any particular directions slightly

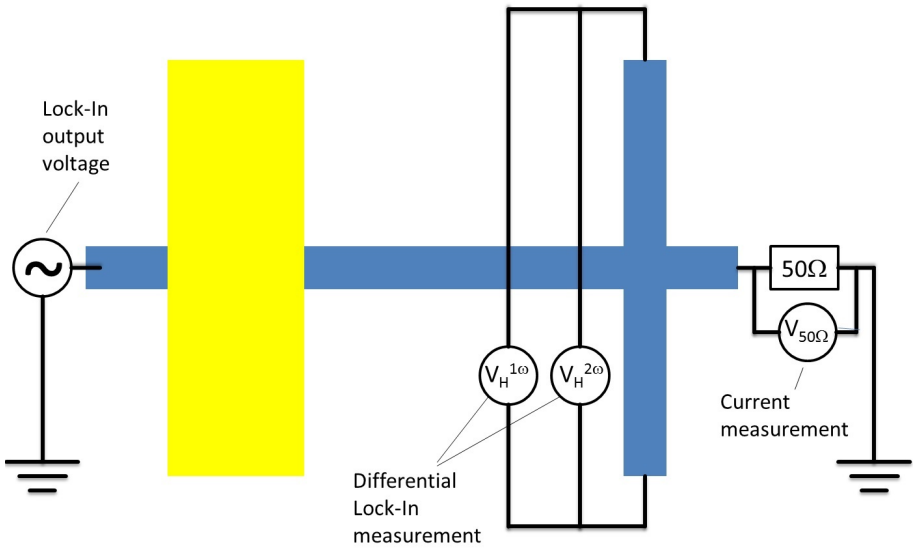

Abbildung 4.2: Circuit diagram for the torque magnetometry measurement. A low frequency ac voltage is applied to the nanowire system, which converts into an ac current across the sample. The Hall signal is measured at the patterned Hall bar contacts and analyzed for the first and second harmonics of the applied measurement frequency using two Lock-im-amplifiers. Additionally the generated current is measured using the voltage drop over a 50 Ω resistance behind the sample.

tilted away from these main axes. This is especially necessary for measuring the torque signals in the intermediate and large angle regime, where one needs otherwise very large magnetic fields to be able to detect the torque efficiencies, as we will see later in subsection 4.3.2. In order to perform the vectorial magnetic field scans, a special control software was developed as part of this thesis to automatize the measurement procedures and give the user quick access to conveniently configure any arbitrary magnetic field scan provided by the 3D-vector magnet setup.

The He4 cryostat allows us to perform magnetometry measurements for various temperatures and with great temperature stability. During a single scan, the temperature variations are $\Delta T \lesssim \pm 20$ mK, which leads to good signal-to-noise ratios.

Next, the sample is connected to our electrical measurement equipment. The circuit diagram for the torque magnetometry measurements is illustrated in Fig. 4.2.

Our typical measurement protocol can be described as follows: We use the voltage output of a Lock-in-amplifier as a voltage source to apply a low-frequency ac-voltage V_{ac} to one end of the patterned nanowire with Hall-bar geometry. This generates a sinusoidal current flow $I_{ac} = I_0 \sin(\omega t)$ along the nanowire, which we measure in terms of a longitudinal voltage drop over a 50 Ω resistance placed in series at the other end of the nanowire (see Fig. 4.2).

As previously discussed, the current generated SOTs act on the magnetization vector and tilt it out of its zero current equilibrium position. This tilting ($\Delta\theta$, $\Delta\phi$) can be measured via the first and second harmonics of the Hall voltage, $V_H^{1\omega}$ and $V_H^{2\omega}$, respectively and will be discussed in more detail throughout this chapter.

Within the torque magnetometry method we want the magnetization vector to follow to the effective fields generated by the acting torques adiabatically. Therefore, the frequency of the applied voltage (and current) ω has to be chosen much smaller compared to the electronic relaxation and spin dynamics time scales of the magnetic multilayer system. The latter are typically in the MHz to GHz regime. Additionally, for signal quality reasons the test-frequency should ideally not be an integer multiple of the net frequency, which is 50 Hz in Germany, where the experimental setup was located. In our measurements we chose an arbitrarily test-frequency $\omega = 13.7$ Hz.

Technically, we measure $V_H^{1\omega}$ and $V_H^{2\omega}$ simultaneously by using a T-shaped connector to split the signal coming from the sample and feeding it into two Lock-In amplifiers. This turned out to provide a better signal-to-noise ratio with our measurement equipment than other available methods, e.g. compared to use a software-side Fourier analysis[101] or a single Lock-In with the ability to measure two or more harmonics at the same time (e.g. with the *Signal Recovery model 7265*).

Typically, the Hall resistance R_{xy} of a metallic FM system contains of three contributions originating from the ordinary Hall effect (OHE), the AHE and the planar Hall effect (PHE). In our Ta/CoFeB/MgO system the OHE is negligible small compared to the other contributions, so that the Hall resistance has only relevant contributions from the AHE and PHE and can be written as:

$$R_{xy} = \frac{1}{2}\Delta R_{AHE}\cos\theta + \frac{1}{2}\Delta R_{PHE}\sin^2\theta\sin 2\phi, \tag{4.2}$$

The first term represents the AHE and the second term the PHE contribution, with ΔR_{AHE} and ΔR_{PHE} being their corresponding resistance coefficients, respectively. θ and ϕ are the polar and azimuthal angles of the magnetization vector $\boldsymbol{m}$. A schematically illustration and the definition of the coordinate system we used in Eq. (4.2) and for the remaining of this chapter is shown in Fig. 4.1.

Next, we want to discuss the torque magnetometry measurement scheme in more detail. When an in-plane magnetic field, $\boldsymbol{H}_{\mathrm{x,y}}$, is applied to the sample, the magnetization vector, $\boldsymbol{M}$, is tilted away from the out-of-plane easy axis ($\hat{z}$-direction). The competition between applied magnetic in-plane field and internal anisotropy fields thereby leads to a new equilibrium position of the magnetization, which we define by the polar and azimuthal equilibrium angles θ_0 and the ϕ_0, respectively.

By neglecting for a moment the relatively small PHE contribution (for our sample we measure a ratio between the PHE and AHE, $\xi = \Delta R_{\mathrm{PHE}}/\Delta R_{\mathrm{AHE}} \approx 5$ %), the measured Hall resistance, given by the anomalous Hall term, is commonly estimated as directly proportional to the z-component of the magnetization, yielding[110,119]:

$$R_{xy,\,\mathrm{OHE}\ll\mathrm{PHE}\ll\mathrm{AHE}} \approx R_{\mathrm{AHE}} \propto m_z = \cos\theta_0. \tag{4.3}$$

In the following this proportionality is used as a tool to evaluate the magnetization's equilibrium polar angles, θ_0, for a given applied in-plane magnetic field in a fixed azimuthal direction, ϕ_0.

So far the evaluation applies to all of the three defined angular regimes. In the following it is useful to split the experimental results section into three parts, where we continue with

a more detailed description of the field-scans and their individual data analysis procedures, individually.

4.3 Results on torque magnetometry

As introduced above, we utilize in the following three different analysis methods for the small, intermediate and large angular regime and later combine the individual results to get the full angular dependence of the SOTs.

4.3.1 Small angular regime

The measurement procedure works as follows: First the magnetization of the sample is saturated in one of the easy axis directions ($\pm\hat{z}$) by applying an external out-of-plane magnetic field, $\pm H_z$, which is larger than the coercive field, $\boldsymbol{H}_c \approx \pm 20$ mT, of the Hall-bar shaped nanostructure.

Next, H_z is relaxed to zero and a magnetic field in the longitudinal or transverse in-plane direction, $H_{x,\,y}$, is systematically increased. With the in-plane magnetic field we can systematically tune the equilibrium position of the magnetization away from the easy axis direction, $\pm\hat{z}$, towards the longitudinal or transverse in-plane axes, $\pm\hat{x}$ or $\pm\hat{y}$, within the zx- or zy-plane, respectively. Doing so, the first and second harmonics of the Hall signals, $V_H^{1\omega}$ and $V_H^{2\omega}$, are recorded, as described in section 4.2. Typical raw data of such a measurement in the small angular regime with $\theta \lesssim 10°$ is shown in Fig. 4.3.

In the small angular regime, the first harmonics Hall signal, $V_H^{1\omega}$, (Fig. 4.3 (a) & (b)) shows in good approximation a quadratic dependence on the external magnetic in-plane field, $H_{x,\,y}$.

Using a small-angle approximation for $V_H^{1\omega} \propto \cos\theta \approx 1 - \frac{1}{2}\theta^2$, we can extract the polar angles of the magnetization, which reflect the magnetization's equilibrium position for each applied in-plane field.

By analyzing the measurement results for the second harmonics signal (Fig. 4.3 (c) & (d)), we observe, that $V_H^{2\omega}$ depends linearly on the applied magnetic in-plane fields for all combination of the initial saturation magnetization direction and longitudinal or transverse in-plane field direction. Additionally, one can observe that the longitudinal scan yields a negative slope for both, the positive ($M+$, black) and negative ($M-$, red) initial magnetization saturation scenario, but switches sign for the transverse magnetic field scan. This behavior reflects the different symmetries of the FL- and AD-like torques (See fig. 2.10 (b)).

To further analyze the data we perform a linear fit to the data and extract the average value of the slopes for both initial magnetization directions, while taking into account the change in sign for the transverse field scan. This analysis method has been developed first by J. Kim et al.[103] and is guiding also the remaining analysis within the small angular regime.

In order to extract the effective spin-torque fields acting in the longitudinal and transverse direction from the first and second harmonics raw data one can use the relation[103]:

$$H_{L,\,T}^{meas\pm} = -2\frac{\partial V_{2\omega}^{\pm}}{\partial H_{x,\,y}} \Big/ \frac{\partial^2 V_{\omega}^{\pm}}{\partial H_{x,\,y}^2}, \tag{4.4}$$

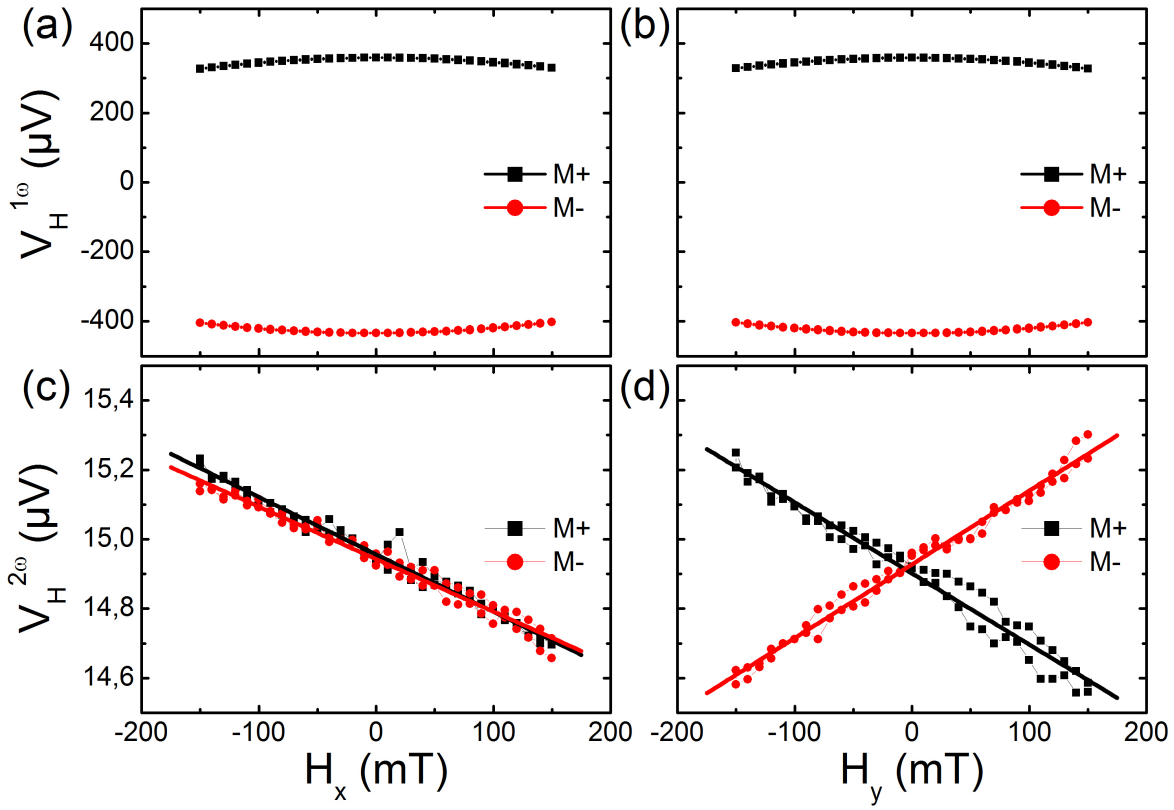

Abbildung 4.3: First and second harmonic Hall signal as a function of (a) & (c) longitudinal or (b) & (d) transverse magnetic field for positive and negative magnetic ground states, $\pm M$, respectively.

where the ±sign represents the up and down magnetization scans, respectively.

So far, we have neglected the small PHE contribution in our analysis. In order to obtain a more accurate analysis, we include it, which leads to a small decomposition of the longitudinal and transverse current-induced fields in the measured signal $H_L^{meas\pm} = \pm(H_L - 2\xi H_T)$ and $H_T^{meas\pm} = (H_T - 2\xi H_L)$.

Following the derivation by M. Hayashi et al.[110] or H.-R. Lee et al.[131], one can now use

$$H_L = \frac{\pm H_L^{meas\pm} \pm 2\xi H_T^{meas\pm}}{1 - 4\xi^2} \tag{4.5}$$

and

$$H_T = \frac{H_T^{meas\pm} \pm 2\xi H_L^{meas\pm}}{1 - 4\xi^2} \tag{4.6}$$

to disentangle the mixing of the longitudinal and transverse contributions and find the corrected values for the current-induced effective fields, H_L and H_T. We repeat the measurements for various current densities in the range between $5 - 8 \times 10^{10}$A/m^2 and for various temperatures T in the range of 50-300 K. The resulting corrected effective fields H_L and H_T are plotted as a

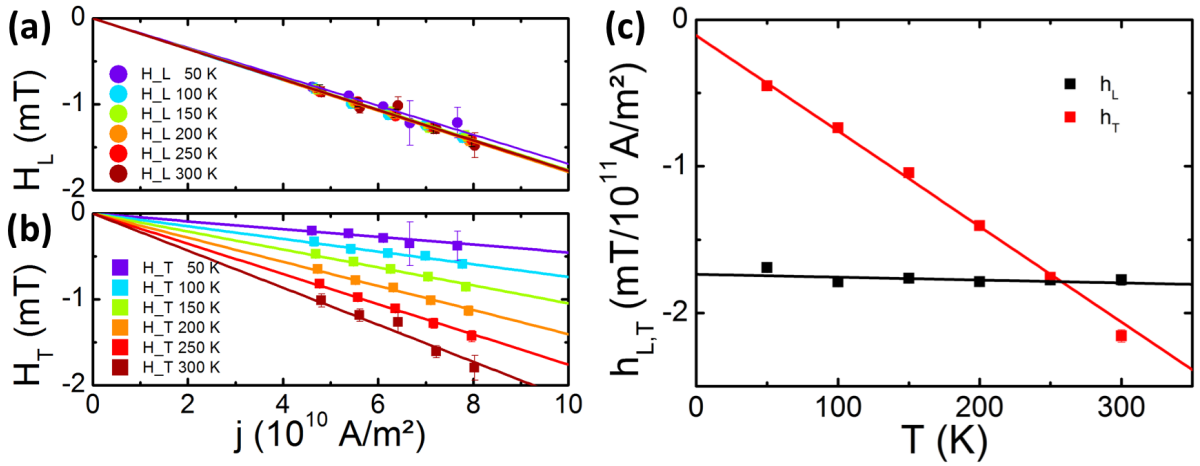

Abbildung 4.4: Results for torque magnetometry measurements in the small angle regime and for temperatures between 50 K and 300 K. (a) & (b) show the corrected longitudinal and transverse effective SOT-fields measured for various current densities, respectively. The effective SOT-fields both depend inversely proportional on the applied current density. (c) shows the extracted effective SOT-field efficiencies $h_{\mathrm{L,T}} = dH_{\mathrm{L,T}}/dj$ plotted as a function of temperature, which summarizes Fig. (a) & (b).

function of current density in Fig. 4.4 (a) and (b). Here the sign of the magnetization was taken into account and H_L and H_T represent the averaged effective fields for both the up and down magnetization state measurements.

Analyzing first the room temperature results (dark red colored symbols), we find that both, the longitudinal effective fields, H_{L}, as well as the transverse effective fields, H_{T}, scale linearly and inverse proportional with the applied current density, j.

Taking a linear fit of the room temperature data for $H_L(j)$ and $H_T(j)$ (dark red solid line in Fig. 4.4 (a) & (b)) yields an average longitudinal and transverse SOT-field efficiency for our Ta/CoFeB/MgO sample, $h_L^{300\mathrm{K}} = dH_L^{300\mathrm{K}}/dj \approx (-1.77 \pm 0.04) \times 10^{11}\mathrm{mT/Am^{-2}}$ and $h_T^{300\mathrm{K}} = dH_T^{300\mathrm{K}}/dj \approx (-2.16 \pm 0.04) \times 10^{11}\mathrm{mT/Am^{-2}}$ (Fig. 4.4(c)). These results fit well with the results found by other research groups using similar material stacks e.g.[101,103,111]. However, a more detailed quantitative comparison should only be discussed by considering at the same time that e.g. even small differences in the growth conditions for the nominal same material stack can have large effects on the measured torque efficiencies and can therefore not give particular good insights[109].

Analyzing next the temperature dependence of the SOTs, shown in Fig. 4.4 (c), one can see that h_{T} varies strongly in the range from 50 K to 300 K, where h_{L} is more or less temperature independent. This is a strong indicator, that h_{L} & h_{T} originate from different microscopic origins. h_{L} & h_{T} are typically also-called as the AD-like & FL-SOTs, which are attributed as dominated by the SHE & ISGE, respectively, as discussed in section 2.6. However, since both, the SHE and the ISGE can give rise to an effective field in the longitudinal and transverse current direction a definite separation of the individual contributions is still under investigation in the spin-torque research community and will not be further discussed here.

4.3.2 Intermediate angular regime

For the small angular regime (see subsection 4.3.1) we saw that the first (second) harmonics signal follows a quadratic (linear) trend as a function of the applied external magnetic in-plane field, respectively. For larger polar angles, $\theta \gtrsim 10°$, the signal deviates significantly from this behavior, so that the small angle approximations made during the derivation of Eq. (4.4) to (4.6) are not valid anymore and the Hall signal requires a more sophisticated analysis. This is usually done by taking into account the complex angular dependence of the magnetization's tilting angle $\theta(B_{ext})$ into the fitting equation for $V_H^{2\omega}$, without a simplifying approximation[101].

In the literature this has been investigated first by K. Garello et al.[101] for the angular regime $10° < \theta < 60°$ in Pt/Co/AlOx and Ta/CoFeB/MgO samples. Later X. Qiu et al.[111] used a slightly different analysis approach and analyzed the SOT effective fields in the range of $10° < \theta < 80°$ in a Ta/CoFeB/MgO sample.

In this thesis we follow for the intermediate angular regime the analysis method reported by K. Garello et al.[101]. Here the second harmonics Hall signal is described as a function of the magnetization direction $\boldsymbol{M}$ in spherical coordinates (θ, ϕ) as follows[101]:

$$\begin{aligned} V_H^{2\omega}(\theta,\ \phi) = (\Delta R_{AHE} - 2\Delta R_{PHE}\cos\theta\sin 2\phi)\frac{d\cos\theta}{dH_{ext}}\frac{H_\theta}{\sin(\theta_H - \theta)} \\ + 2\Delta R_{PHE}\sin^2\theta\cos 2\phi\frac{H_\phi}{\sin\theta_H}. \end{aligned} \tag{4.7}$$

Hereby, H_{ext} is the applied external magnetic field, H_θ and H_ϕ represent the polar and azimuthal components of the total current-induced effective fields, H_{L} and H_{T}, which we want to determine. A detailed derivation of Eq. (4.7) can be found e.g. in Ref.[101].

One major difference in the experimental measurement protocol for the intermediate (and also large) angular regime compared to the small angular regime is to apply the external magnetic field during the field-scan not aligned with the sample's in-plane axis. Instead, the field is applied with an additional fixed out-of-plane polar angle $\theta_H \neq 0$ (see Fig. 4.1). This is done to prevent multi-domain states from forming at large tilting angles. Additionally, one is able to scan a wider angular range within the limited 1 T field range of our in-plane magnets. Since this out-of-plane component is pointing anti-parallel to the initial saturation direction it supports the tilting into the in-plane direction by counteracting the strong internal uni-axial anisotropy fields, thus leading to a larger tilting of the magnetization vector. But it also makes the analysis more complicated. For our measurements we use a tilting angle of the applied external magnetic field, $\theta_H = 82°$, which is a good trade off, between the signal size of $V_H^{2\omega}$ and the maximum tilting angle of the magnetization vector, θ_{max}.

Fig. 4.5 shows the measurement results we obtain for our Ta/CoFeB/MgO sample using the measurement scheme described above. Both, Fig. 4.5 (a) and (b) show the first (black) and second harmonics (red) Hall voltage signals as a function of the applied external magnetic field in the longitudinal and transverse in-plane direction with the above described out-of-plane tilting angle θ_H, respectively.

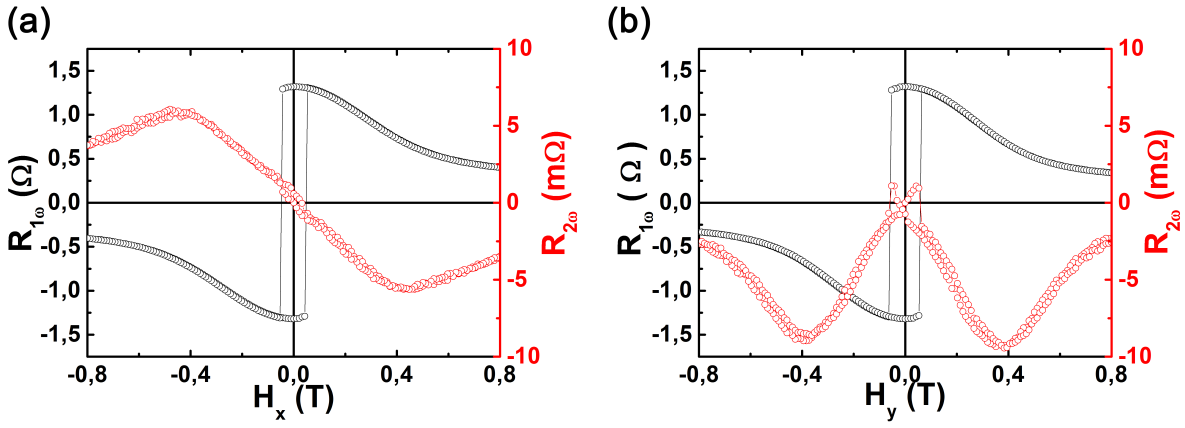

Abbildung 4.5: First (black) and second (red) harmonics Hall resistance measurements as function of longitudinal (a) & transverse (b) magnetic field with a fixed out-of-plane tilting angle of the field, $\theta_{\mathrm{H}} = 8°$.

For small applied magnetic fields one can identify the already discussed linear and quadratic behavior of $V_H^{2\omega}$ and $V_H^{1\omega}$, respectively. Different from the behavior discussed in subsection 4.3.1, one can now observe a switching of the magnetization at $\boldsymbol{H}_{x,\,y} \approx \pm 50$ mT, which occurs due to the discussed out-of-plane component of the external magnetic field applied with the extra tilting angle θ_H.

However, here we analyze $V_H^{2\omega}$ for the intermediate angle regime beyond the switching field and find that the signal continues to increase (decrease) monotonically until it reaches a maximum (minimum) at the perpendicular magnetic anisotropy field, $H_K \approx 400$ mT, depending on the sign of the $\hat{z}$ component of the magnetization vector. For fields larger than H_K the signal decreases (increases) again, respectively.

Following the analysis method developed by K. Garello et al.[101], we first extract the corresponding θ-angle of the magnetization for each applied in-plane magnetic field from the first harmonics signal by using that $V_H^{1\omega} \propto \cos\theta$. Next, we use an iterative fitting approach to extract H_θ and H_ϕ by using a Taylor expansion of the torques, T_{L} & T_{T}, modeling the torque anisotropy in the form of $T_{\mathrm{L}} = T_{\mathrm{L}}^0 + T_{\mathrm{L}}^2 + T_{\mathrm{L}}^4$ and $T_{\mathrm{T}} = T_{\mathrm{T}}^0 + T_{\mathrm{T}}^2 + T_{\mathrm{T}}^4$. Finally, this allows us to convert H_θ and H_ϕ into H_{L} and H_{T}. A detailed instructive analysis protocol can be found in Appendix B.

Fig. 4.6 shows the extracted angle dependence of H_L and H_T in the intermediate regime, using the iterative fitting approach.

Qualitatively, both, H_L and H_T, have negative values and increase in the intermediate polar regime. For small polar angles both effective fields diverge because the derivative of the first harmonics vanishes for the flat part of $R_H^{1\omega}$. For polar angles $\theta \gtrsim 70°$ the signal becomes to low and therefore the extracted effective fields values become very noisy. This limits the range of the intermediate regime. Additionally, we find that H_L is always less negative then H_T with a maximum ratio of $H_T/H_L \approx 2.8$ for $\theta \approx 70°$. This behavior has also been seen by other groups measuring on Ta/CoFeB/MgO samples[101,111].

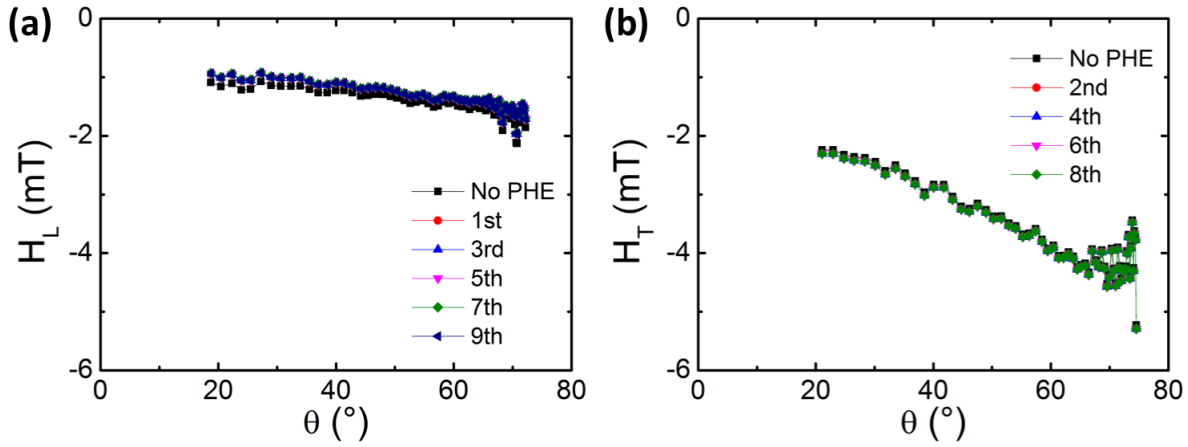

Abbildung 4.6: Angular dependence of the (a) longitudinal and (b) transverse SOT effective field obtained by using the analysis method developed by Garello et al.[101].

4.3.3 Large angular regime

As we saw in Fig. 4.6, the extracted SOT effective fields become noisy for polar angles θ larger than $\approx 70°$ when using the iterative fitting approach developed by K. Garello et al.[101].

Another approach to analyze the data at such large angles, $\theta \approx 70° - 90°$, is to fit the $1/(H_{\text{ext}} - H_{\text{K}})$ decrease of the second harmonics Hall signal, $V_H^{2\omega}$, with

$$V_H^{2\omega} = -\frac{1}{2}\frac{\Delta R_{\text{AHE}} H_{\text{L,T}}}{H_{\text{ext}} - H_{\text{K}}} \cdot i, \tag{4.8}$$

with i, beign the applied current. This approach was first published by Y. Fan et al.[112] and was applied only to second harmonics Hall data within a magnetic field scan in the transverse direction. In this thesis, however, we use this approach to fit both the longitudinal and transverse measurement data.

Accordingly, Fig. 4.7 shows the fits to the second harmonics data in the large angular regime. Note that this approach does not include the PHE contribution. As already stated, in our system the PHE is only 5% of the AHE, therefore we can still apply this method to calculate the effective fields in the high magnetic field regime without generating large errors.

Doing so, we derive as the effective SOT fields $\mu_0 h_{\text{L}} = (-1.29 \pm 0.1)\ \text{mT}/10^{11}\text{Am}^{-2}$ and $\mu_0 h_{\text{T}} = (-0.11 \pm 0.04)\ \text{mT}/10^{11}\text{Am}^{-2}$ for the large polar angle regime $\theta \approx 70° - 90°$.

4.3.4 Extraction of the full angular dependence of the SOT effective fields

So far we have discussed the different analysis methods and results obtained for the individual angular regimes separately. Next, we want to compare them and extract the full angular dependence of the SOT effective fields for our Ta/CoFeB/MgO sample.

Fig. 4.8 shows the results for the SOT effective field efficiencies for the different angular regimes plotted in the same graph. Qualitatively the results fit together and form a relatively smooth

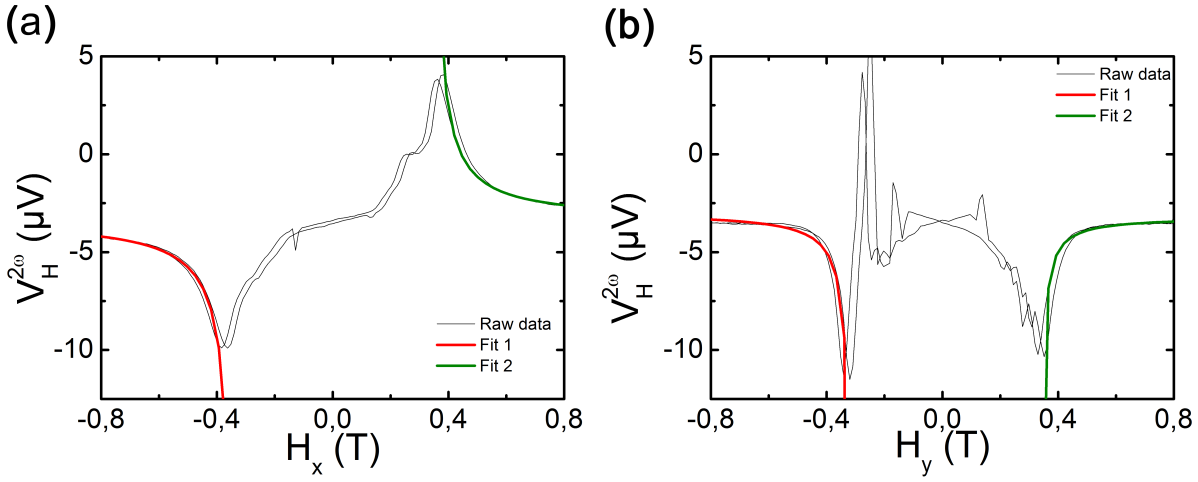

Abbildung 4.7: Second harmonics Hall signal plotted as a function of applied longitudinal (a) and transverse external magnetic field (b). The magnetic field is applied with a fixed out-of-plane tilting angle $\theta_H = 8°$. The $1/(H_{\text{ext}} - H_{\text{K}})$ decrease of the raw data (black) is fitted by using Eq. (4.8). Fits are highlighted in red and green for the large negative and positive field range, respectively.

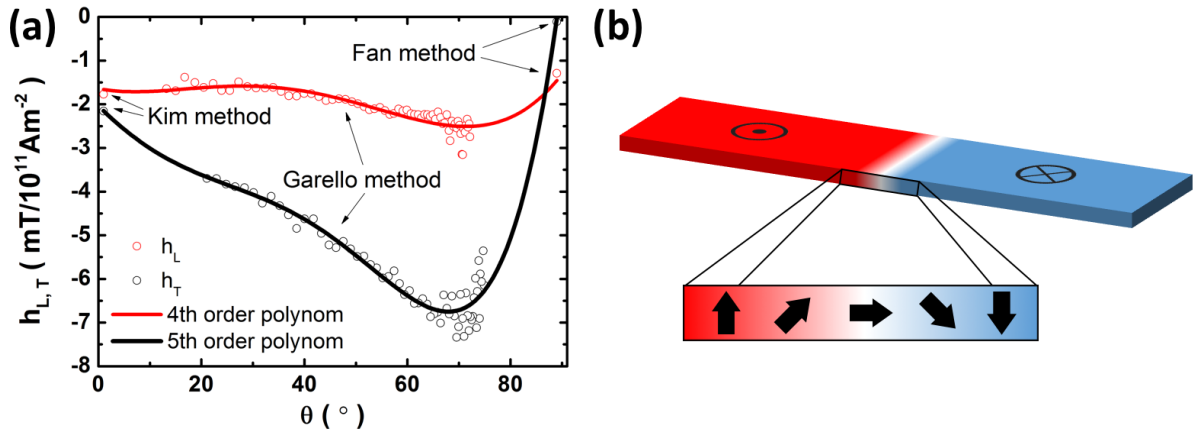

Abbildung 4.8: (a) Angular dependence of the SOT effective fields obtained by using three different analysis methods for the small, intermediate and large angular regime of the magnetization angle θ. The longitudinal and transverse effective fields efficiencies, $h_{\text{L}}(\theta)$ and $h_{\text{T}}(\theta)$ are highlighted in red and black, respectively. The solid lines are polynomial fits to the data points of 4th and 5th order for the longitudinal and transverse data, respectively. (b) Illustration of the internal magnetization profile of a Néel type DW. The polar angle changes from 0° to π as one follows the DW profile from left to right.

curve. Both SOT effective field efficiencies, $h_{\mathrm{L}}(\theta)$ & $h_{\mathrm{T}}(\theta)$, start with an intermediate value at small polar angles and increase monotonically until they reach a maximum at a certain polar angle $\theta_{\mathrm{L,T}}^{\mathrm{max}} \approx 70°$, which is within our accuracy range equal for the longitudinal and transverse field direction. Note that the transverse effective field is for $\theta \lesssim 70°$ always smaller then the longitudinal field, but than goes immediately to ≈ 0 mT for $\theta \gtrsim 70°$, where h_{L} remains still nonzero. Note that at large angles the magnetization is pointing almost into the plane of the nanostructure, and both the SHE and ISGE model predicts a vanishing torque at this range, since the cross-product between equilibrium magnetization vector $\boldsymbol{m}$ and the non-equilibrium spin-density $\delta\boldsymbol{m}$ vanishes. This behavior can also be observed in our measurement results.

Lastly, we want to extract analytical expressions for the angular dependence of the effective SOT fields to model their anisotropic behavior. These can later be used e.g. to calculate the effective fields for arbitrary spin-textures (as we will see in the section 4.4). Here, we fit the extracted effective SOT fields with simple polynomial curves, even though these have no deeper physical meaning, but nicely represent the data, which is sufficient for our purposes. For the angular dependence of effective fields we tested polynomials of various orders and finally find good fitting for the longitudinal effective field with a polynomial of order 4 and for the transverse effective field with a polynomial of order 5 (solid lines in Fig. 4.8 (a)):

$$\begin{aligned} h_{\mathrm{L}}(\theta) &= a + b \cdot \theta + c \cdot \theta^2 + d \cdot \theta^3 + e \cdot \theta^4 \\ h_{\mathrm{T}}(\theta) &= a' + b' \cdot \theta + c' \cdot \theta^2 + d' \cdot \theta^3 + e' \cdot \theta^4 + f' \cdot \theta^5. \end{aligned} \tag{4.9}$$

4.4 Effective SOT field for Néel type domain walls

So far we have determined the full angular dependence of the SOT effective fields for a homogeneous magnetization texture, with all spins pointing in the same direction, which we tuned with an external magnetic field. In this case all spins are expected to experience approximately the same effective torque field. Next, we want to calculate the effective torque field for a more complex spin-structure such as a magnetic DW. In this case the spin directions across the sample are not homogeneous anymore.

Here, we want to calculate the expected average effective SOT fields in the scenario of a Néel type DW. Fig. 4.8 (b) schematically shows the profile of a Néel DW. Analytically the Néel DW profile can be written as

$$\boldsymbol{M}_{\text{Néel DW}} = \frac{\boldsymbol{M}_s}{\cosh\frac{x-q}{\lambda}} \left(\cos\psi,\ \sin\psi,\ \sinh\frac{x-q}{\lambda}\right), \tag{4.10}$$

with λ being the length of the DW and ψ and q being the collective coordinates in a 1D model describing the DW dynamics. In the following we calculate the effective field for such a DW by using the full angular dependence of the SOT effective fields, $h_{\mathrm{AD,FL}}[\theta(x)] \equiv h_{\mathrm{L,T}}[\theta(x)]$, which we obtained in the previous section from our torque magnetometry measurements.

Assuming that the DW is centered around $x = 0$ and thus the spins tilt from $\theta = -\pi/2$ to $\theta = +\pi/2$ along the DW profile, the averaged effective field can be determined using[130]

$$h_{\mathrm{AD,FL}}^{\mathrm{avg}} = \frac{1}{\pi\lambda} \int \frac{h_{\mathrm{AD,FL}}[\theta(x)]}{\cosh\left(\frac{x-q}{\lambda}\right)} dx. \tag{4.11}$$

Note that every spin vector within the DW profile is correctly weighted with its corresponding SOT effective field strength $h_{\mathrm{AD,FL}}[\theta(x)]$ as the integral sums up all the effective field terms for each spin in the DW. Doing so, we obtain as the average SOT effective fields for a Néel type DW in our Ta / CoFeB / MgO sample $\mu_0 h_{\mathrm{AD}}^{\mathrm{avg}} \approx -1.57\ \mathrm{mT}/10^{11}\mathrm{Am}^{-2}$ and $\mu_0 h_{\mathrm{FL}}^{\mathrm{avg}} \approx -4.5\ \mathrm{mT}/10^{11}\mathrm{Am}^{-2}$ for the AD- and FL-torque component, respectively.

4.5 1D modeling of the depinning field

In the previous section (4.4) we used the measured angular dependence of the SOT effective fields to calculate the effective SOT fields acting on a Néel type DW. Next, we want to go another step further and calculate within a 1D model Ansatz for this DW type the current equivalent out-of-plane field ΔH_z, which can be detected within a DW depinning experiment (such as investigated in[10,49,50,132] and later in this thesis in chapter 6).

Following the formalism to model the DW depinning process developed by Benjamin Krüger[130], one obtains for the current equivalent out-of-plane field,

$$\Delta H_z = H_{\mathrm{dep,j}} - H_{z,0} \approx \frac{\pi}{2} h_{\mathrm{AD}}^{\mathrm{avg}} \cdot j, \tag{4.12}$$

whereby $H_{\mathrm{dep,j}}$ is the depinning field measured while a current density, j, is applied to the sample and $H_{z,0}$ is the critical out-of-plane depinning field when no current is applied. Note that here it is crucial to take into account the $\frac{\pi}{2}$ integration factor in order to translate effective SOT fields determined with torque magnetometry measurements into effective current-equivalent out-of-plane depinning fields. This has not been pointed out so clearly previous to this thesis work and was reported by us in[130].

However, inserting the values that we determined in the previous section, we obtain an effective out-of-plane depinning field efficiency, $\Delta h_{\mathrm{z,calc}}^{\mathrm{depin}} \sim (2.45 \pm 0.5)\ \mathrm{mT}/10^{11}\mathrm{Am}^{-2}$.

It is noticeable that the current-equivalent-field, calculated from the SOT field measured at the low angle magnetization tilt, shows a similar value of $\Delta h_{\mathrm{z,calc}}^{\mathrm{depin}} \sim (2.24 \pm 0.7)\ \mathrm{mT}/10^{11}\mathrm{Am}^{-2}$, which is because the angular dependence of the AD-like effective field is relatively small in our Ta / CoFeB / MgO sample and the FL effective field has only a small effect on the effective depinning fields[130], which is to alter slightly the critical DW tilting angle, ψ, just before the depinning occurs. This does not change much the critical DW depinning field and is included within the error bar of $\Delta h_{\mathrm{z,calc}}^{\mathrm{depin}}$.

However, in chapter 6 we will compare our experimental results on real DW depinning measurements with the values we calculated here and discuss further on the validation and implications of this approach.

4.6 Summary

We performed torque magnetometry measurements on a Ta / CoFeB / MgO nanostructure in Hall-bar geometry using the higher harmonics analysis technique of the Hall effect. By applying magnetic field-scans in the longitudinal and transverse direction with respect to the sample geometry we tuned the samples magnetization vector systematically pointing in-plane and thus we were able to measure the polar angular dependence of the SOTs. Since it is not possible to measure the full polar angular dependence of the SOTs with a single measurement technique, we applied three different techniques, each of these developed for a specific angular regime, namely the small, intermediate and large angular regime. By combining the three different analysis methods, we validated their congruence and finally extracted a simple analytical polynomial expression for the anisotropic behavior of the AD- and FL-SOT effective fields, which has previous to this thesis work not done on a single sample so far[101,103,108,110–112].

Next, we used the extracted analytical expression for the full angular dependence of the torques determined from measurements on a homogeneous spin-texture to calculate the total effective fields acting on more complex spin-textures. This becomes in general necessary, since the constituting spins of complex spin-textures are not aligned homogeneously anymore, thus the current-induced effects across the spin-texture will not be homogeneous accordingly. We examined this theoretical calculation at the example of a Néel type DW[1], where the spins perform a full angular rotation accordingly to its characteristic DW profile.

Lastly, we used the determined total effective field for such a Néel DW to calculate the current-equivalent out-of-plane field, which can be measured during a DW depinning experiment[50,132,133]. This enables us later in chapter 6 to compare these two completely different experimental methods. Given the relatively small angular dependence of the AD-torque effective field in our sample it is clear, that the angular dependence will not have such a large influence on the effective field of a complex spatially varying spin-texture. However, for other materials this may not be the case.

Additionally, it was confirmed during the thesis work, that the influence of the FL-SOT effective field on the effective depinning field is almost negligible and it will only change the equilibrium tilting angle of the DW just before the depinning process occurs. This behavior however was not investigated in more detail within the thesis.

In chapter 6 we will compare the theoretically predicted values for current-equivalent out-of-plane fields to values obtained in real DW depinning measurements and discuss the validation of such a comparison and its further implications.

Previous to that, we introduce first in chapter 5 how a DW can be reliably created e.g. by injecting an ultra-short current pulse into the Au stripe line, which is fabricated on top and perpendicular to our nanowire structure (see Fig. 3.3).

[1] The calculations have been performed by Benjamin Krüger[130].

5 Domain wall nucleation experiments

5.1 Introduction

In this chapter, we want to establish a writing scheme for magnetic DWs in our Ta / CoFeB / MgO based nanowire structure, by using current-induced Oersted fields.

With this technique, the creation of magnetic DWs is realized together with a local reversal of the magnetization direction inside the nanowire in the vicinity of our nanofabricated Oersted line (see Fig. 3.3). The reversal process happens due to the formation of a new magnetic domain, separated from the residual magnetization inside the nanowire by two DWs (see Fig. 5.1 (b)). Later, in chapter 6, we want to use one of those two DWs to investigate the field- and current-induced DW depinning through the Hall cross geometry, that is patterned intro our sample. For this purpose, a controlled and reliable DW nucleation scheme is mandatory and will be developed throughout this chapter.

The remaining is structured as follows: First, we describe in section 5.2 the Oersted field writing technique in more detail. Second, we characterize in section 5.3 the nucleation properties of our nanowire sample, by investigating in particular the critical conditions for a successful DW nucleation as a function of supporting external magnetic field and current pulse parameters, i.e. pulse amplitude (see subsection 5.3.1) and pulse width (subsection 5.3.2).

5.2 Domain wall nucleation technique

In this section, we describe the DW nucleation technique using current-induced Oersted fields in more detail. The method is illustrated in Fig. 5.1 and can be separated into multiple steps. To monitor the success of each step, we measure the EHE of the sample at the Hall cross, by using standard Lock-In equipment. The characteristic Hall-signal is plotted in Fig. 5.2. Here, the red and blue data points show the Hall signal during the nucleation process for a ↓↑- and ↑↓-DW, respectively. The black data points show the standard out-of-plane magnetic hysteresis loop, when no DW is nucleated and the coercive field, $H_c \approx 22$ mT, of the 400 nm wide nanowire can be determined[1]. The individual steps of the nucleation scheme are discussed in the following for the case of a ↓↑-DW nucleation & detection at the Hall cross. For the nucleation of the reversed ↑↓-DW, the nucleation scheme just has to be performed with the reversed field and current pulse polarities, accordingly.

[1] Note, the difference between H_c of the 400 nm wide nanowire in contrast to $H_c^{\text{thin film}} \approx 2$ mT, the coercive field for the unpatterned thin film (see subsection 3.1.2).

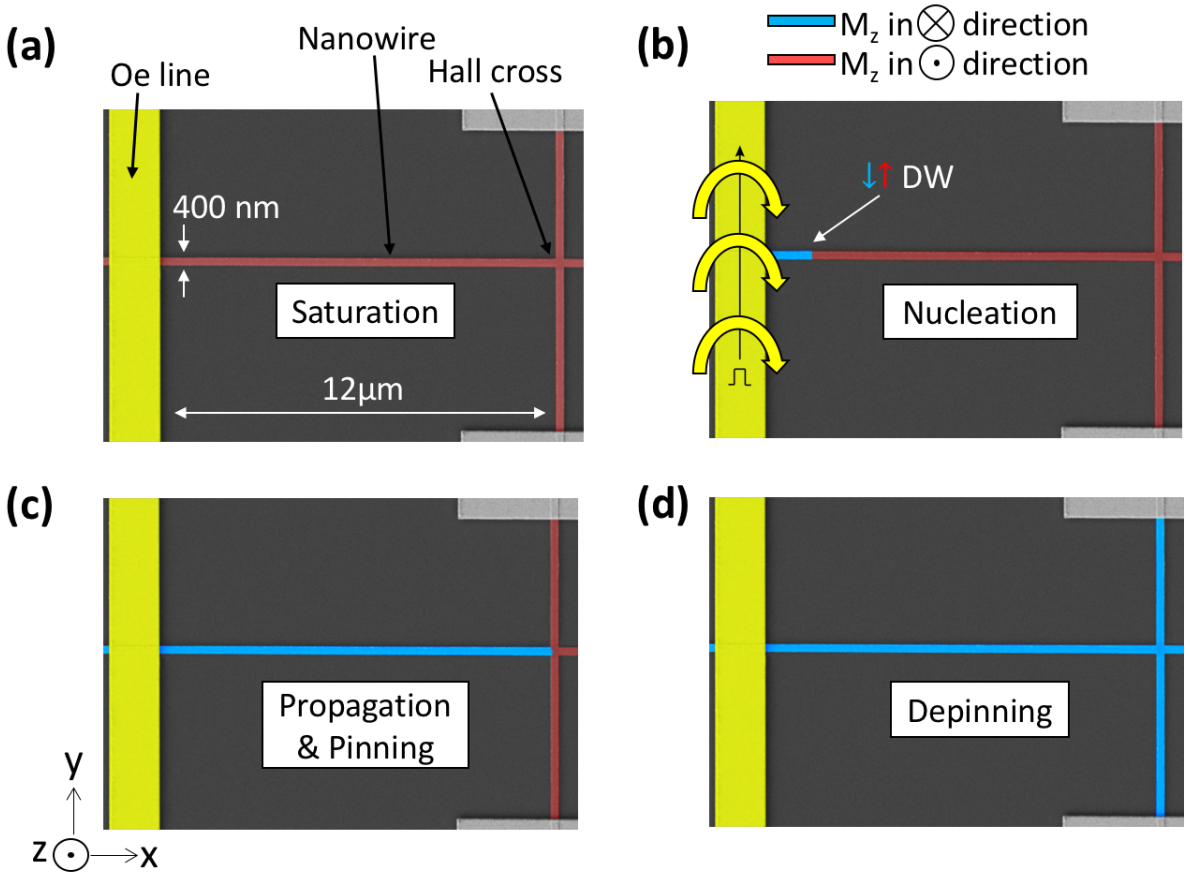

Abbildung 5.1: Illustration of the current-induced DW nucleation scheme. (a) First, the magnetization of the nanowire is saturated in the easy-axis direction by applying an external magnetic out-of-plane field H_z. Here, the initial saturation direction is the positive $\hat{z}$-direction, highlighted by the red color of the nanowire. (b) Next, the field is removed to zero or a small reversed supporting field H_{nuc} is applied into the negative $\hat{z}$-direction and a current pulse is injected into the Oersted (Oe) line. The current pulse generates a coaxial Oe field, H_{Oe}, around the Oe line. If the Oe field is large enough, a new domain will be nucleated pointing in the opposite direction compared to the initial saturation direction (highlighted in blue color). (c) An external magnetic field $|H_z| \geq |H_p|$, pointing in the negative $\hat{z}$-direction is used to expand the new domain. Accordingly, the right DW moves towards the entrance of the Hall cross, where it gets pinned. (d) For $|H_z| \geq |H^{\star}_{c,\downarrow\uparrow}|$ pointing in the negative $\hat{z}$-direction, the DW moves across the Hall cross structure, which we call DW depinning.

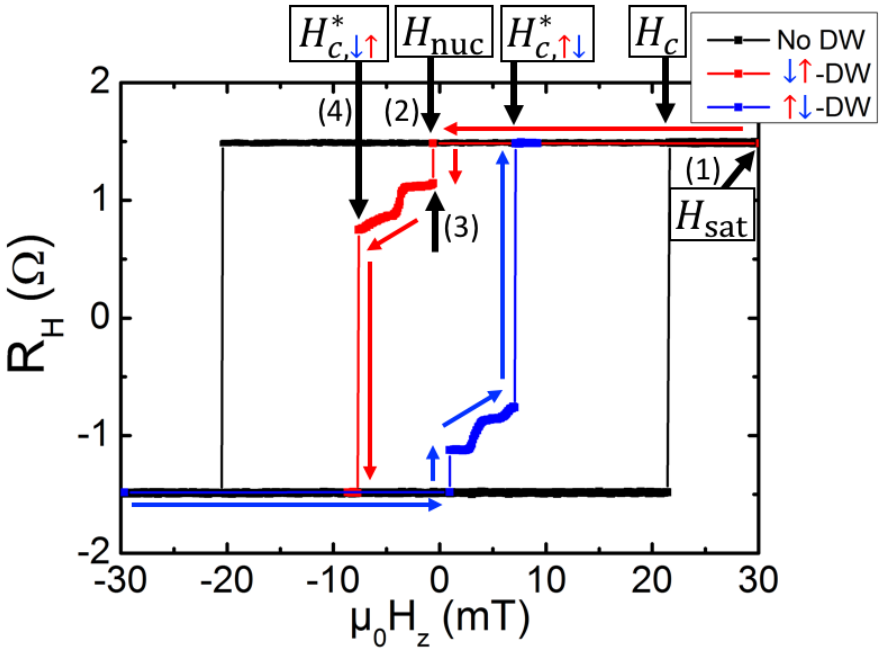

Abbildung 5.2: Hall resistance of a 400 nm wide Ta/CoFeB/MgO nanowire measured at the Hall cross. The black data points show the EHE signal measured during a standard out-of-plane hysteresis loop. The switching occurs at the coercive field $H_c \approx 22$ mT. The red and blue data points show typical Hall signals during the DW nucleation scheme and also the DW depinning from the Hall cross for a ↓↑- and ↑↓-DW, respectively. In case of the ↓↑-DW nucleation, the nanowire is first saturated at $H_z > H_{sat}$ (step (1)). Then a small supporting field for the nucleation H_{nuc} is applied in the opposite direction (step (2)) and a current pulse is injected into the Oersted line. If the DW nucleation was successful, the Hall signal jumps to an intermediate level (step (3)), after the field, H, is systematically increased to $|H_c^\star| > |H| > |H_p|$, where $H_c^\star$ (step (4)) is the reduced coercive field of the Hall cross for which the ↓↑-DW is depinned through the Hall cross and H_p is the propagation field of the DW.

First, the magnetization of the sample is saturated in one of the easy-axis directions under the influence of an external out-of-plane magnetic field, $H_{\mathrm{sat}} > H_c$, indicated by the red highlighting of the nanostructure in Fig. 5.1 (a) and the Hall-signal showing the system being in the magnetization ↑-state (Single red data point at step (1) in Fig. 5.2).

Second, the external magnetic field is removed and eventually a small supporting magnetic field for the nucleation process, H_{nuc}, with $0 \leq |H_{\mathrm{nuc}}| < |H_p| < |H^{\star}_{c,\downarrow\uparrow}| < |H_c|$, in the opposite direction is applied, where H_p is the DW propagation field and $H^{\star}_{c,\downarrow\uparrow}$ is the reduced coercive field in the presence of a ↓↑-DW, which is also the ↓↑-DW depinning field of the Hall cross. Accordingly, we observe the magnetization still remains in the ↑-state (Single red data point at step (2) in Fig. 5.2).

Then, a short current pulse is injected into the nanofabricated Au stripe, which is located on top of and perpendicular to the nanowire, as illustrated in Fig. 5.1 (b). The Au stripe, we call in the following as an Oersted (Oe) line.

For this purpose, we calculate first the theoretically possible Oe fields for a realistic maximum current density, $j^{Oe}_{\mathrm{max}} = 1 \times 10^{12}\mathrm{A/m}^2$, using the COMSOL Multiphysics software package[2]. Fig. 5.3 (a) shows the calculated Oe field generated in the vicinity of the Oe line. We find, that for our Oe line dimensions, 1.4 μm ×150 nm, that we used in the experiment, it should be theoretically possible to generate at maximum an Oe field of $H^{Oe}_{\mathrm{max}} \approx 100$ mT at the boundary of the Oe line, which is larger than the coercive field of the 400 nm wide nanowire and therefore should be enough to locally reverse the magnetization direction by current only.

In our experiments, we typically inject square shaped unipolar voltage pulses (dashed line in Fig. 5.3 (b) & (c), generated by an ultra-fast pulse generator (Picosecond Model 10060A), with a fixed rise/fall time, $t_r = t_f = 55$ ps and a variable pulse width $\Delta t = 1 - 10$ ns, via the impedance matched high frequency lines of our setup.

Due to the flow of current, a concentric magnetic field, the so-called Oe field is generated around Oe line (see Fig. 5.1 (b)). When the Oe field is large enough, i.e. when $i \geq i_c$, where i_c is the critical current necessary to nucleate a new domain with a magnetization direction in the negative $\hat{z}$-direction, the magnetization direction of the ferromagnet can be reversed locally in the vicinity of the Oe line, as indicated by the blue colored area of the nanowire in Fig. 5.1 (b).

After a successful nucleation, the new magnetic domain will remain in the nanowire confined by two DWs. One DW, the ↓↑-DW, is located between the Oe line and the adjacent Hall cross (highlighted in Fig. 5.1 (b)) and the other one, the ↑↓-DW, is directly below the Oe line (not visible in Fig. 5.1 (b)).

In order to detect the success of the DW nucleation, an external magnetic field, $|H_z| \geq |H_p|$, is applied into the negative $\hat{z}$-direction, leading to an expansion of the reversed ↓-domain (Fig. 5.1 (c)). Here, H_p, is the characteristic DW propagation field of the nanowire, where for $|H_z| \geq |H_p|$ the field-induced DW motion is induced, which means, that the DW can overcome all small pinning sides formed by the edge roughness of the nanowire.

For the two DWs described above, two different scenarios can be assumed. Under the influence of H_p, the left ↑↓-DW will move towards the left and eventually gets expelled at the left end of the nanowire. The right ↓↑-DW, in contrast, will move towards the right, approaching the Hall cross.

[2]The COMSOL Multiphysics simulation has been set up by June Seo Kim.

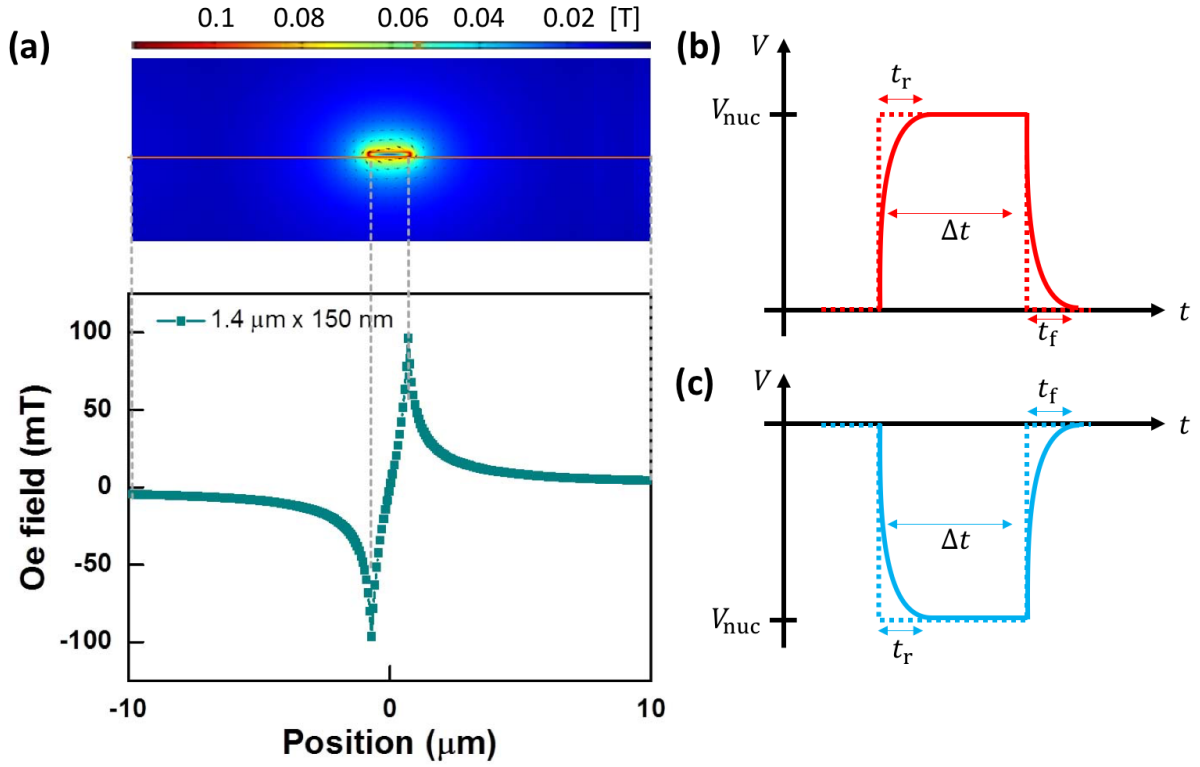

Abbildung 5.3: (a) (Top graph) 2D heat map of the calculated Oe field generated in the vicinity of the Oe line for a fixed current density of $j^{Oe} = 1 \times 10^{12}\text{A/m}^2$ and our real Oe line dimensions using the COMSOL Multiphysics software package. The Bottom graph shows a cross section of the 2D map at the interface between Oe line and nanowire. Close to the edge of the Oe line, magnetic Oe fields of about 100 mT can be theoretically expected. (b) & (c) Illustration of the nucleation pulse, injected into the Oe line. (b) The injected pulse amplitude has either positive polarity for a ↓↑-DW nucleation or (c) negative polarity for a ↑↓-DW nucleation in combination with the appropriate initial saturation direction of the nanowire's magnetization, respectively.

Typically, the Hall cross forms a strong pinning site for DWs with a critical out-of-plane field, $H_c^\star$, necessary to overcome the pinning barrier. For an applied field H, with $|H_p| < |H| < |H^\star_{c,\downarrow\uparrow}|$, the right ↓↑-DW arrives at the entrance of the Hall cross and gets pinned (Fig. 5.1 (c)). This can then be detected in the Hall signal, showing an intermediate level between the ↑- and ↓-saturation states (Step (3) in Fig. 5.2).

Depending on the used supporting nucleation field, H_{nuc}, we observe the Hall signal after the nucleation pulse to be typically somewhere between the markers (2) and (4) in Fig. 5.2. If $|H_{\text{nuc}}| \geq |H^\star_{c,\downarrow\uparrow}|$ the magnetization in the sample would switch completely to the ↓-state (Fig. 5.1 (d) and step (4) in Fig. 5.2). As shown in the Hall-signal in Fig. 5.2, one can nicely observe the incrementally depinning of the ↓↑-DW through the Hall cross geometry by a systematically increase of the out-of-plane field in the negative $\hat{z}$-direction after the nucleation.

As mentioned above, by reversing the initial saturation direction and all applied fields and the Oe pulse direction accordingly, one can reverse the DW nucleation scenario and instead of a ↓↑-DW

shift a ↑↓-DW towards the Hall cross, as illustrated by the blue data points in Fig. 5.2. We will use both DW nucleation scenarios later in chapter 6 as the basis for the depinning measurements.

5.3 Critical conditions for domain wall nucleation

Next, we want to characterize the nucleation properties of our nanowire, by investigating in particular the critical conditions for a successful DW nucleation as a function of supporting magnetic field and current pulse parameters, i.e. pulse amplitude (see subsection 5.3.1) and pulse width (see subsection 5.3.2).

5.3.1 Measurement of the generated Oersted field

First, we want to test the nucleation scheme discussed in section 5.2 for various supporting magnetic field amplitudes in the direction opposite to the initial saturation direction and for various current densities of the nucleation pulse through the Oe line. For that, we fixed the nucleation pulse width to be 10 ns. The success of the nucleation is checked by monitoring the Hall signal at the Hall cross, as described above. For various fixed pulse current densities, we systematically varied the supporting magnetic field, H_{nuc}, until we find the critical condition for a successful DW nucleation.

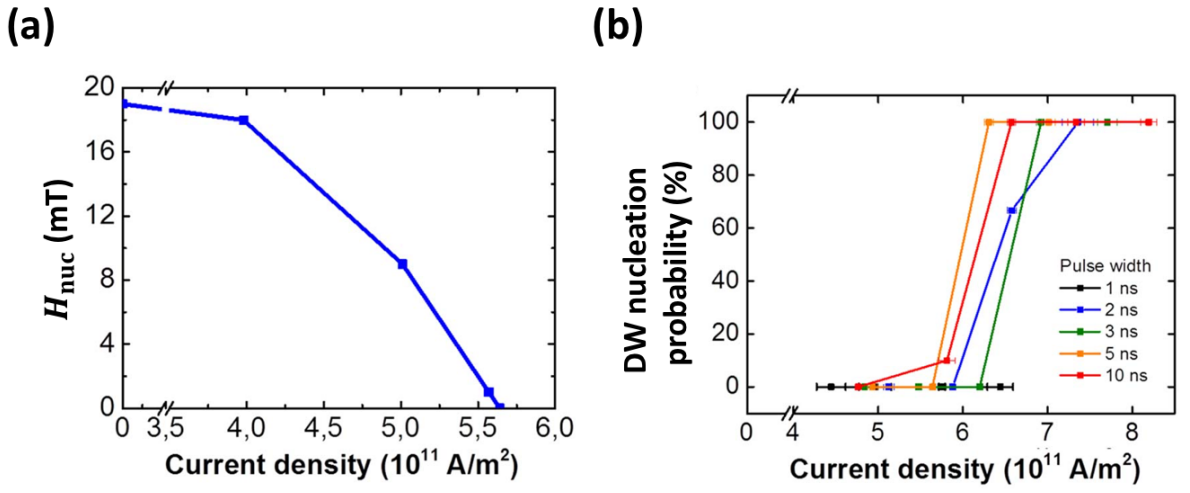

Abbildung 5.4: (a) Decrease of the necessary supporting magnet field, H_{nuc}, for a successful DW nucleation as a function of applied Oe pulse current density through the Oe line. (b) DW Nucleation probability as a function of nucleation pulse current density for various pulse widths between 1-10 ns.

Fig. 5.4 (a) shows the results of this experiment. Without a nucleation pulse, $j^{Oe} = 0$ A/m^2, no DW is nucleated and the Hall cross can only be switched purely field-induced for magnetic fields larger than or equal to the coercive field of the wire[3].

For current densities of the Oe pulse larger than the critical current density $j_c^{Oe} \approx 4 \times 10^{11}$A/m^2 and for supporting magnetic fields about 18 mT, the nucleation starts to be successful. We further increase the current density and can systematically observe how the initial supporting magnetic field can be reduced, while still having successful DW nucleation. Finally, for a current density of $j^{Oe} \gtrsim 5.6 \times 10^{11}$A/m^2, we find, that DW nucleation can also be achieved without any supporting external magnetic field.

5.3.2 Pulse width dependence

Having established a successful DW nucleation scheme without the need of any supporting external magnetic field in the previous section, we study next the effect of the pulse width on the nucleation process. For this the nucleation experiment is performed as a function of pulse width, varying from 1-10 ns. For each pulse width the experiment is repeated 10 times.

Fig. 5.4 (b) shows the DW nucleation probability as a function of applied current density through the Oe line with zero supporting external magnetic field applied. The critical current density for a successful DW nucleation increases for shorter pulse widths from $j_c^{Oe} \approx 5.7 \times 10^{11}$A/m^2 for a pulse width $\Delta t = 10$ ns to $j_c^{Oe} \approx 6.3 \times 10^{11}$A/m^2 for a pulse width $\Delta t = 2$ ns. For a pulse width of 1 ns no successful DW nucleation could be observed in the range of current densities up to 6.5×10^{11}A/m^2, which was the limit of our experimental setup for this pulse width.

One can observe, that the nucleation success depends for such short current pulses only little on the pulse width. This is because the heating effect for 1 ns & 10 ns does not differ so much. For much longer pulses, this might not be the case and the local heating effect of the Oe pulse changes the anisotropy of the material significantly, which makes the domain reversal to happen for much lower pulse amplitudes.

5.4 Summary

In summary, we have established in this chapter the Oe field writing scheme in our 400 nm wide Ta / CoFeB / MgO based nanowire.

Fist, we tested the nucleation scheme for various combinations of supporting magnetic field, H_{nuc} and applied Oe pulse current density, j^{Oe} at a fixed pulse width of 10 ns and found that a successful DW nucleation can be achieved for Oe pulse current densities above $\boldsymbol{j}_c^{\mathrm{nuc}} \approx 4 \times 10^{11}$A/m^2. By further systematic increase of the Oe pulse current amplitude, the necessary supporting field could be lowered. Doing so, we found for a 10 ns long pulse a critical current density of

[3]This dataset has been measured on a different, but identical sample from the same thin film and fabrication batch, exhibiting a slightly different coercive field, $H_c \approx 19$ mT, instead of the otherwise discussed 22 mT. However beside the difference in absolute values, both samples show identical behavior and the discussion does not loose generality.

$j_c^{Oe} \gtrsim 5.6 \times 10^{11}\mathrm{A/m^2}$, for that DW nucleation could be achieved also without any external supporting magnetic field.

Having this, we studied the reliability of the Oe field writing method for various pulse lengths and found an excellent reproducibility of 100 % for current pulses with a pulse width down to 2 ns and current densities of $j_c^{Oe} \approx 5.5 \times 10^{11}\mathrm{A/m^2}$ (Fig. 5.4 (b)).

The results on the DW nucleation experiments show that the Oersted field writing scheme can be considered as reliable enough for scientific applications and can therefore be used in the following of this thesis for the DW depinning experiments, which, given the large amount of repetitions and the time consumption of the experiments, require a very reliable, automatable DW writing process.

6 Domain wall depinning experiments

6.1 Introduction

So far, we have discussed in chapter 4 the angular dependence of the SOTs for a homogeneous magnetization texture in a Ta / CoFeB / MgO multilayer system using the torque magnetometry method. Based on that, we calculated in section 4.5 the expected current-induced depinning fields for more complex magnetic textures, such as a Néel type magnetic DW, where the SOTs are expected to be maximized.

In chapter 5, we have established a reliable nucleation scheme for ↑↓- and ↓↑-DWs, where as a result, the nucleated DWs can be generated and reliably pinned at the entrance of a Hall cross geometry.

In this chapter, we want to measure the action of the current-induced torques on DWs within real DW depinning experiments. This will allow us to compare the results of the predicted depinning fields based on the SOTs magnetometry measurements to real measurements of DW depinning fields, obtained in this chapter.

The remaining of this chapter is structured as follows:
First, in section 6.2, we introduce the experimental technique for DW depinning measurements in more detail.

The discussion of the measurement results for the DW depinning experiments is split into three sections: First, in section 6.3, we investigate the purely field-induced DW depinning process, for the cases without (see subsection 6.3.1) and with an external in-plane magnetic field applied (Subsection 6.3.2). Next, we continue with the current-induced DW depinning experiments. First, in section 6.4, for the case of current injected perpendicular to the DW and second, in section 6.5, for the 90° rotated case of current injected parallel to the DW.

Finally, in chapter 7, we summarize the results for field- and current-induced DW depinning experiments and compare the obtained effective depinning efficiencies to the theoretically calculated values based on the 1D model.

6.2 Measurement technique

After a DW is successfully placed at the entrance of the Hall cross by following the nucleation scheme described in section 5.2, the depinning field, H_{dep}, necessary to push a pinned DW through the Hall cross is measured. This is done by detecting the characteristic change of the EHE signal (Step (4) and (5) in Fig. 6.1), induced by the depinning process. By using the current-field-equivalence[10,49,50], the current-induced STTs acting on the DW can be measured.

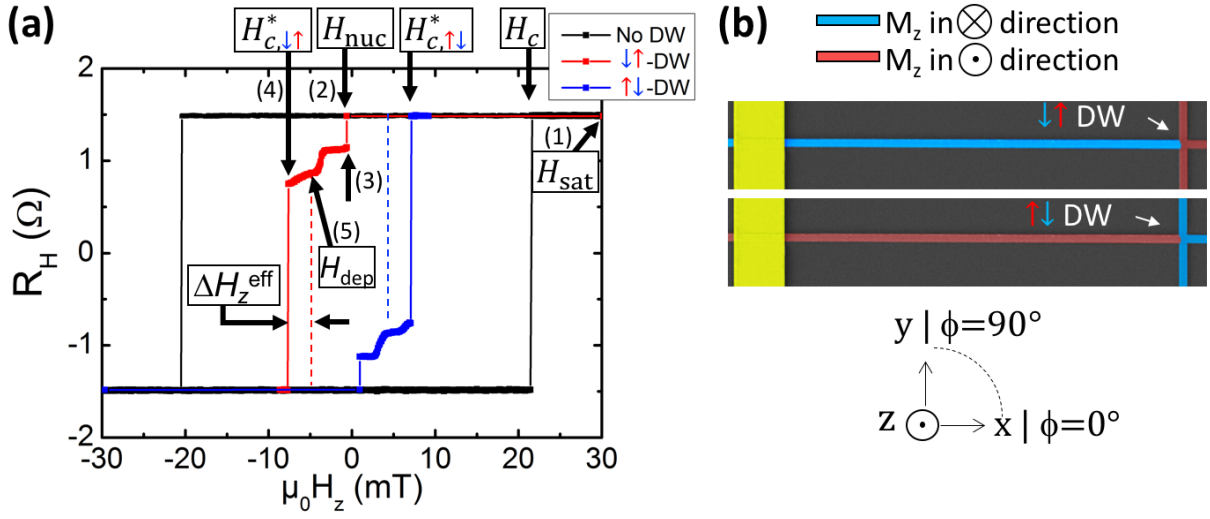

Abbildung 6.1: (a) Hall resistance of a 400 nm wide Ta/CoFeB/MgO nanowire measured at the Hall cross. The black data points show the EHE signal measured during a standard out-of-plane hysteresis loop. The switching occurs at the coercive field, $H_c \approx 22$ mT. The red and blue data points show typical Hall signals during the DW nucleation scheme and the DW depinning through the Hall cross for a ↓↑- and ↑↓-DW, respectively. In the case of a ↓↑-DW nucleation, the nanowire is first saturated at $H_z > H_{sat}$ (Step (1)). Then a small supporting field for the nucleation, H_{nuc}, is applied into the opposite direction (Step (2)) and a current pulse is injected into the Oersted line. If the DW nucleation was successful, the Hall signal jumps to an intermediate level (Step (3)), after the field, H_z, is systematically increased to $|H_c^\star| > |H_z| > |H_p|$, where $H_c^\star$ is the reduced coercive field of the Hall cross for which the ↓↑-DW is depinned through the Hall cross (Step (4)) and H_p is the propagation field along the nanowire. The dashed line (Step (5)), indicates a reduced depinning field of the DW, H_{dep}, which can occur e.g. due to an applied in-plane field or due to an applied current density, $j > j_c$, as explained in more detail in the main text. (b) Illustration of the coordinate system and the two DW scenarios.

Furthermore the current field-equivalence method can be used to study the symmetry of the acting torques by using an additional external magnetic in-plane field to manipulate the DW's internal magnetization direction. This is explained in more detail in subsection 6.2.1.

6.2.1 Strength and symmetry of the spin-orbit torques

First, the DW is depinned simply under the influence of an out-of-plane magnetic field $H \geq H_c^\star$ (Step (4) in Fig. 5.2), which we call in the following purely field-induced depinning. Then the experiment is repeated at $H < H_c^\star$, where a current pulse with the correct polarity and a current density above the critical current density is injected into the sample leading to a current-induced DW depinning at a reduced out-of-plane magnetic field, H_{dep}. The difference in out-of-plane field necessary for the depinning at a certain current density is called the *current equivalent effective out-of-plane field*, $\Delta H_z^{\text{eff}} = H_c^\star - H_{\text{dep}}$. ΔH_z^{eff} is a direct measure of the current-induced DW depinning efficiency and varies for various configurations of DWs. In particular we are interested

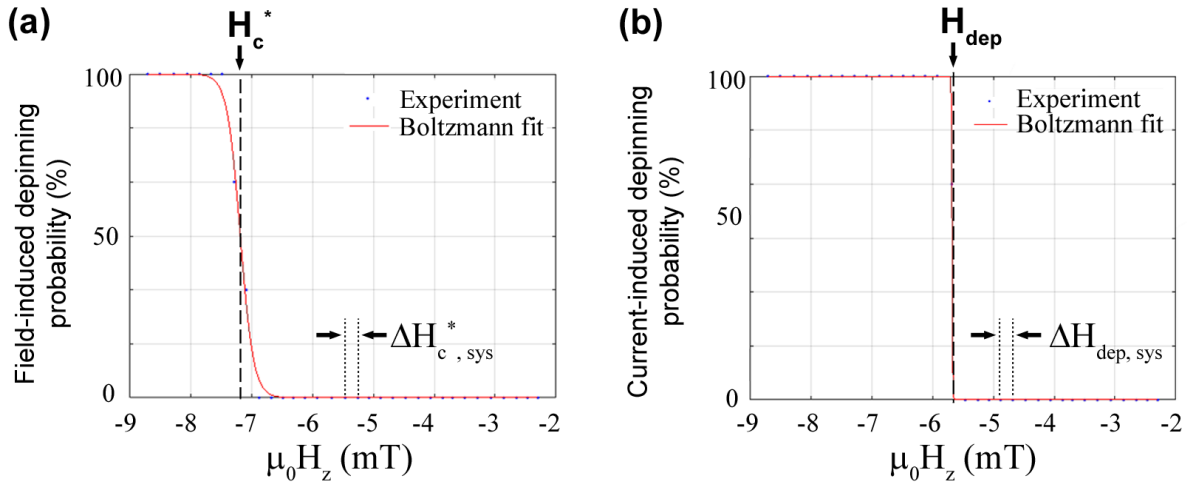

Abbildung 6.2: Depinning probability as function of applied out-of-plane field H_z. (a) shows experimental data for field- and (b) for the current-induced depinning. The experimental data is fitted by a Boltzmann-function, which allows to determine the critical depinning fields $H_c^\star$ and H_{dep}, respectively. Furthermore the evaluation of the the statistical and systematic error is highlighted.

in the changes in the DW depinning efficiency, when the DW's internal magnetic structure is manipulated e.g. by an external in-plane magnetic field (see section 6.3 and 6.4).

6.2.2 Automatized data and error analysis

Since the measurement of the current equivalent effective out-of-plane fields, $\Delta H_z^{\mathrm{eff}}$, implies the determination of the critical condition for each configuration under test, a large dataset (> 30.000 individual measurements) has been measured for this thesis. To analyze the data more effectively an analysis script has been written within the MATLAB software environment. In this section the individual analysis steps, specific considerations and the details of the error analysis will be described in more detail.

As discussed above, the EHE signal can be used to determine $H_c^\star$ and H_{dep}. In the analysis script a threshold value of 50 % of the EHE signal is used to detect the success of the depinning process. In order to obtain the current-field equivalence, the supporting out-of-plane field was scanned across the critical value. All measurements are repeated 3 times for each configuration and the depinning probability is evaluated. Then a Boltzmann-fit $\left(f(x) = 1/\left(1 + exp\left(\frac{x-x_0}{dx}\right)\right)\right)$ is used to determine the critical field- and current-induced depinning fields $H_c^\star$ and H_{dep}, respectively (Fig. 6.2). In the following it is shown how the total error of the current equivalent effective field, $\Delta H_{z,\,\mathrm{err}}^{\mathrm{eff}}$, is determined.

From the slope of the Boltzmann-function, dx, the statistical errors, $\Delta H_{c,\,stat}^\star$ and $\Delta H_{dep,\,stat}$, of the critical fields, $H_c^\star$ and H_{dep}, are evaluated. The systematic errors, $\Delta H_{c,\,\mathrm{sys}}^\star$ and $\Delta H_{\mathrm{dep,\,sys}}$, depend on the step size of the out-of-plane field scan and the accuracy of the magnet. In this thesis the step size has been chosen to be 0.2 mT. The accuracy of the magnet is ≈ 0.01 mT and the related error can therefore be neglected. The total error then is given by the sum of the total statistical

error and the total systematic error, which is included into the data plots in the following of this chapter.

6.3 Field-induced DW depinning

6.3.1 Field-induced depinning without in-plane field

First, we investigate the purely field-induced DW depinning of ↑↓- and ↓↑-DWs with an external magnetic field, H_z, which is applied into the out-of-plane direction, $\hat{z}$. Regardless, whether it is a ↑↓- or ↓↑-DW, we find that the critical field, $H_c^\star$, that is necessary to depin the DW trough the Hall cross has an opposite sign for both DW types, but the same absolute magnitude

$$\left|H^\star_{c,\downarrow\uparrow}\right| = \left|H^\star_{c,\uparrow\downarrow}\right| \approx 7.0 \pm 0.5 \text{ mT}, \tag{6.1}$$

as shown in Fig. 6.1. This result is not surprising since the ↑ and ↓ magnetization direction in a magnetic system is in general degenerated and the action of a positive out-of-plane magnetic field, $+H_z$, which depins an ↑↓-DW through the Hall cross should be the same as its mirrored version, where a negative out-plane magnetic field, $-H_z$, depins a ↓↑-DW.

6.3.2 Field-induced depinning under in-plane field

Next, we investigate the field-induced DW depinning for different in-plane field amplitudes pointing into the longitudinal ($\pm x$) and transverse ($\pm y$) direction.

As discussed in subsection 6.3.1, $|\mu_0 H_c^\star|$ is around 7 mT, if no in-plane field is applied during the depinning process. With an in-plane magnetic field applied, the critical depinning field systematically decreases as a function of the in-plane magnetic field amplitude (see Fig. 6.3 (a)). Additionally, a symmetric behavior can be observed for both, the $\pm H_x$ and $\pm H_y$ field direction, with a slope, $|dH_c^\star / dH_{x,y}| \approx 3\%$ for both, the ↑↓- and ↓↑-DW type.

The offset between the ↑↓- and ↓↑-DW depinning curves of about $\pm(0.5 - 1.0)$ mT can be explained by an offset of the out-of-plane magnetic field around the zero field value during the measurements. Since we are only interested in relative changes of the depinning fields as a function of applied in-plane field within a particular configuration, this offset can be neglected in the following.

The origin of the decrease in $|\mu_0 H_c^\star|$ as a function of the in-plane field can be explained by analyzing the field-induced forces in the Thiele equation. Here, the external magnetic in-plane field stabilizes the internal DW magnetization against rotation/precession. This leads then to an increase of the Walker breakdown field, $H_w(i)$, towards higher values[19,134]. Effectively, this leads to a higher torque-efficiency of the out-of-plane field acting on the DW, which is reflected in a decrease of the depinning field, as the in-plane field is increased.

To understand our experimental data better, numerical simulations based on the 1D-model have been performed by our colleges Oscar Alejos, Simone Moretti and Eduardo Martinez, that

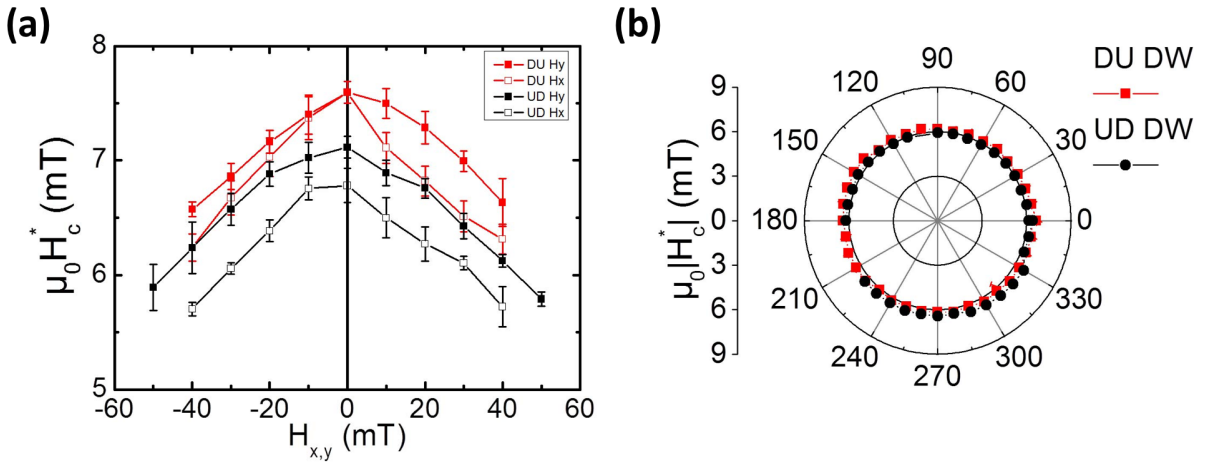

Abbildung 6.3: Field induced depinning results. (a) Critical depinning field, $H_c^\star$, a function of longitudinal and transverse in-plane field amplitude. (b) Angular dependence of the field-induced depinning field at a fixed polar in-plane field amplitude of 40 mT.

model the depinning process. In general a very good agreement between the simulations and the experimental results shown in Fig. 6.3 have been found[132].

Next, we perform an angular scan in which the depinning field is measured for various polar angles, $\phi = 0°$ to $360°$ and at a fixed amplitude of the applied in-plane magnetic field of 40 mT. This angular scan yields the depinning field to be constant, independent of the polar direction or the DW and its type (Fig. 6.3 (b)). This can be explained by the fact that the field-induced depinning in the 1D model does not depend on the internal spin-configuration of the DW, which is changed as the in-plane magnetic field is applied in various polar directions.

This is a key result of the field-induced depinning measurements: Even though there is a dependence on the in-plane field amplitude, it is isotropic in the polar plane and any angular dependence which possibly may occur for current-induced DW depinning can thus directly be attributed to the symmetry of the current-induced torques[132].

6.4 Current-induced DW depinning for current flowing perpendicular to a DW

In the previous section we have established, that field-induced DW depinning is isotropic in terms of an in-plane magnetic field applied within the polar plane. Next, we use this to measure the symmetry of the current-induced effects on a DW during a depinning process. For this, we systematically manipulate the internal magnetization configuration of the pinned DW by applying an additional in-plane magnetic field and then measure the resulting DW depinning efficiency.

For the remaining of this section the current-induced DW depinning measurements are performed with 100 μs long current-pulses with a fixed current density, $j_\perp = 6.4 \times 10^{10}$A/m^2, applied perpendicular to the DW plane. The definition of the current polarity is illustrated in Fig. 6.4. As

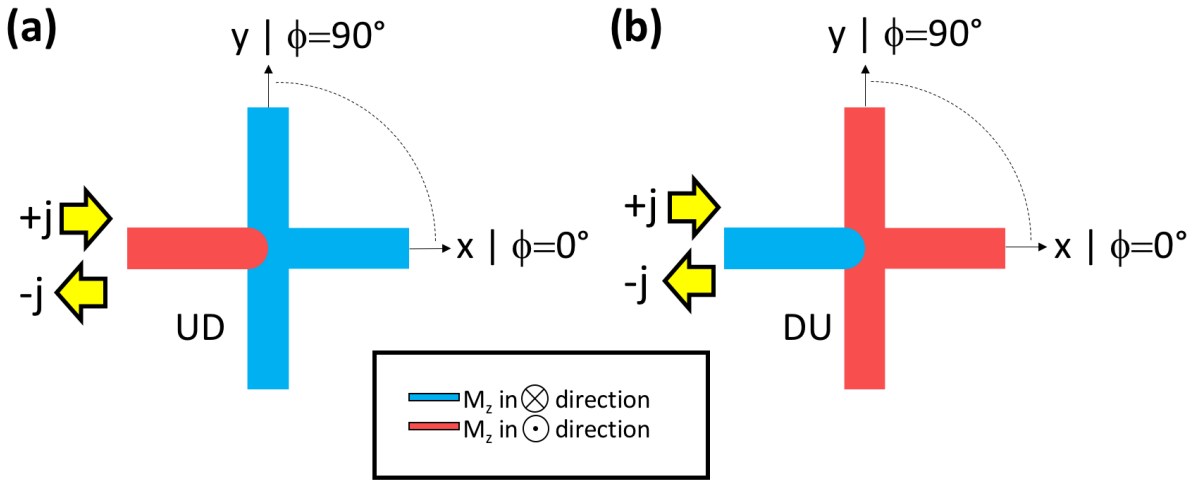

Abbildung 6.4: Sample geometry for the ↑↓- and ↓↑-DW depinning experiments including the definitions of the current directions for current injected perpendicular to the DWs.

introduced in section 6.2, the depinning efficiency is measured in terms of the current-equivalent effective out-of-plane field, ΔH_z^{eff}.

6.4.1 Amplitude dependence of in-plane magnetic fields

In Fig. 6.5 the current-induced DW depinning efficiency is shown for ↑↓- and ↓↑-DWs, for an in-plane magnetic field applied in the longitudinal ((a) & (b)) and transverse direction ((c) & (d)). We discuss the results step by step. First, we analyze the combination of an ↑↓-DW and an in-plane magnetic field applied in the positive longitudinal direction, $+H_x$ (Fig. 6.5 (a)). Here, the DW depinning is only supported by a positive current applied perpendicular to the ↑↓-DW (red dotted line in Fig. 6.5 (a)). This leads to a reduced depinning field, H_{dep}, compared to the purely field-induced depinning field, $H_c^\star$, and therefore to a finite measurable current-induced depinning efficiency, ΔH_z^{eff}, as defined in section 6.2. For a negative current density (blue dotted line in Fig. 6.5 (a)) and a positive longitudinal field, $+H_x$, the DW efficiency remains zero. Here, the depinning field is actually enhanced compared to the purely field-induced depinning field, $H_c^\star$, but generically, this can not be observed using our depinning measurement method. This is because the DW would already depin when an out-of-plane field $H_z = H_c^\star$ is applied, which is before the current pulse is actually applied to the sample. In this case H_{dep} is measured to be equal to $H_c^\star$ and the depinning efficiency, ΔH_z^{eff}, appears to be zero. Small deviations $\Delta H_z^{\text{eff}} \neq 0$ mT can occur when $H_{\text{dep}} \lesssim H_c^\star$, which also reflects the precession of the depinning field measurement.

For the negative longitudinal in-plane field direction, $-H_x$, the situation is reversed and only the negative current density supports the DW depinning process. Accordingly, an increase in the DW depinning efficiency can be observed only for the negative current density (blue dotted line) and the DW depinning efficiency for the positive current density appears to be zero.

For the ↓↑-DW and longitudinal in-plane field (Fig. 6.5 (b)), the scenario is similar, but inverted. Here, negative (positive) current densities lead to an increase of the DW depinning efficiency for positive (negative) longitudinal fields.

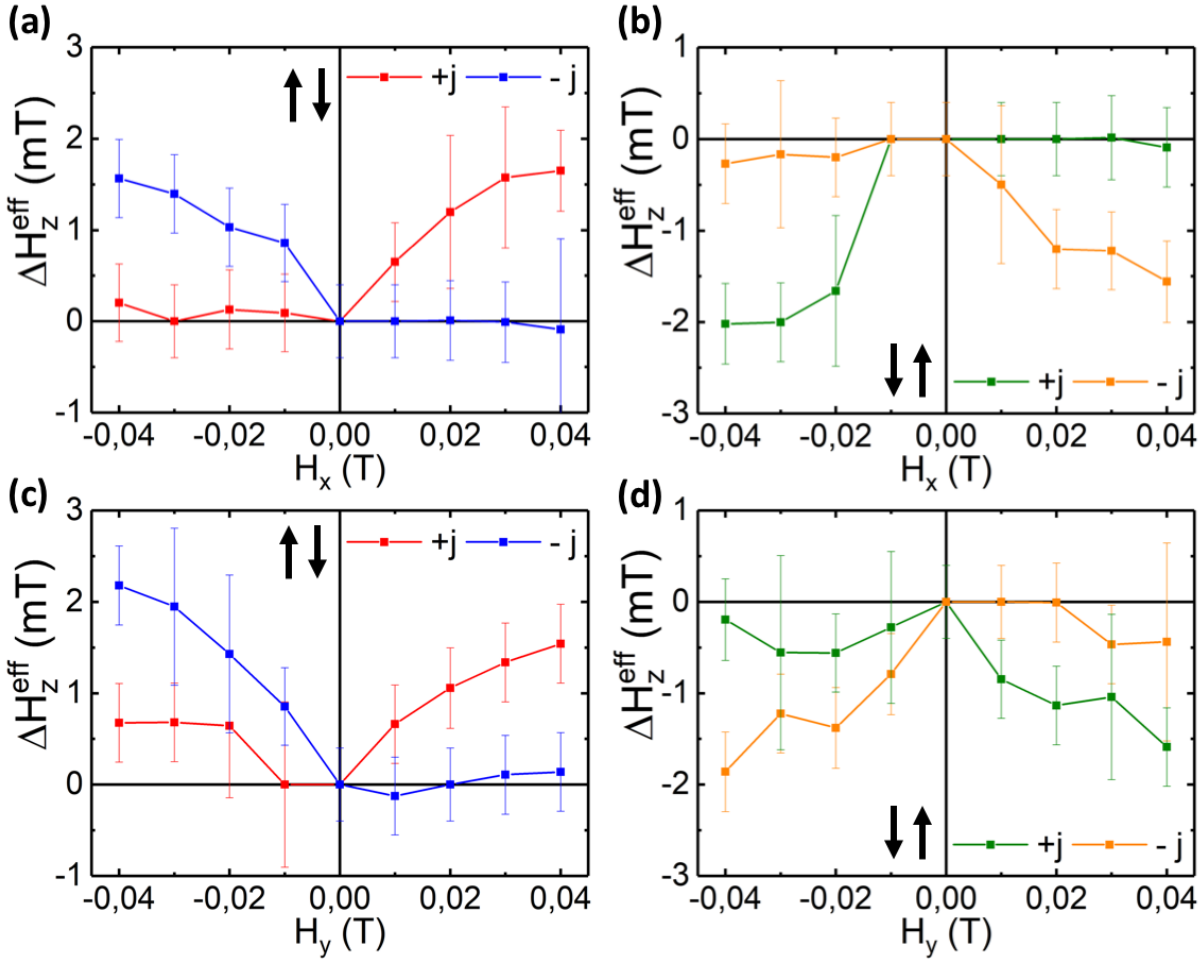

Abbildung 6.5: Results of the current-induced DW depinning measurements for current applied perpendicular to a ↑↓- and ↓↑-DW. The depinning field is measured for both, the longitudinal and transverse direction of the applied in-plane magnetic field.

The increase of the depinning efficiency can be explained by an increasing Néel component of the DW in the $\pm x$-direction, depending on the in-plane field direction. This is in line with the anti-damping-like torque in the SOT-model, where the force on the DW is proportional to the Néel component of the wall, as discussed in subsection 2.6.3. We find for our sample, that for fields, $H_x \geq \pm 40$ mT, the DWs Néel component is maximized in the $+\hat{x}$ or $-\hat{x}$-direction, respectively and the DW depinning efficiency saturates. Consistently, ΔH_z^{eff} saturates at a similar value of $\approx \pm 2$ mT for both, the ↑↓- and ↓↑-DW type. From this, we determine a maximum SOT efficiency, independent of the DW type, of $\chi \approx (3.13 \pm 0.5) \frac{\text{mT}}{10^{11}\text{A/m}^2}$ in our Ta / CoFeB / MgO multilayer system.

Next, we analyze the results for a magnetic field applied in the transverse in-plane direction ($\pm\hat{y}$). Since a transverse field forces the DW to transform into a Bloch wall, the torque originating from the SOTs is expected to vanish for an increasing transverse field (see section 2.6). However, in Fig. 6.5 (c) and (d) we cannot observe this behavior, but instead find a similar behavior as for the case when the field is applied in the longitudinal in-plane direction (Fig. 6.5 (a) and (b)). Moreover the measured effective fields, $\Delta H_z^{\text{eff}} \approx 2$ mT, which is similar to the results found for

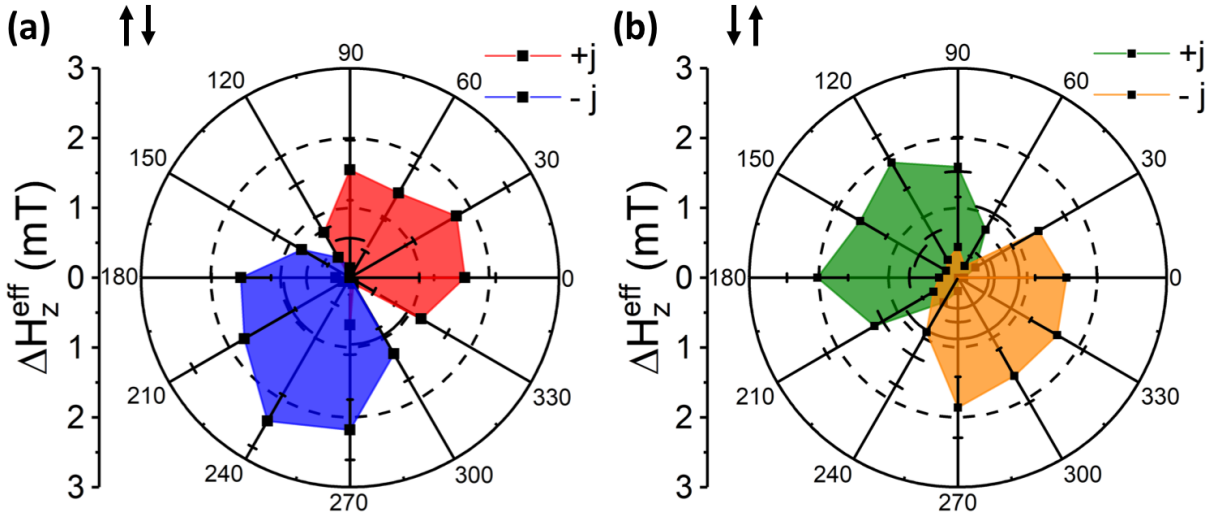

Abbildung 6.6: Polar angle dependent depinning efficiency. (a) & (b) show the depinning efficiency for current injected perpendicular to a ↑↓- & ↓↑-DW, respectively.

the longitudinal field case. This result is in contradiction to what is expected from the simple SOT model, but will be resolved in the following, when we perform full angular scans of the applied in-plane field.

6.4.2 Polar dependence of the in-plane magnetic field

In order to investigate the non-vanishing DW depinning efficiency, even if the DW is tuned into a Bloch wall, we systematically repeat the current-induced depinning measurement for multiple polar angles from $\phi = 0°$ to 360° of the in-plane field at a fixed in-plane field amplitude of $|H_{x,y}| = 40$ mT. We chose this particular field amplitude, since we expect a saturation of the internal magnetization of the DW in the direction of the applied in-plane field from the field-amplitude measurements (Fig. 6.5).

We determine the current equivalent effective out-of-plane field for each polar angle, ϕ, and plot it as a function of ϕ. In Fig. 6.6 (a) & (b) the experimental results are shown for a ↑↓- and ↓↑-DW, respectively. The current has been applied in both cases perpendicular to the DW, i.e. into the $\phi = 0°$ and $\phi = 180°$ direction. The current polarity is highlighted in red for a positive and in blue for a negative current density, j, in the case of a ↑↓-DW and in green and orange in the case of a ↓↑-DW, respectively.

From the simple SOT model one expects in the field-polarized configuration of a straight DW a $\cos^2(\phi - \phi_0^{\pm})$-dependence of the effective out-of-plane field with $\phi_0^+ = 0°$ and $\phi_0^- = 180°$ for $j > 0$ and $j < 0$, respectively.

In general the experimental results confirm the expected $\cos^2(\phi)$-dependence in all four cases of DW type and current polarity. Also the reversal of the current polarity, leads to a rotation of the depinning efficiency by an angle of π. However, an unexpected tilt of the maximum efficiency angle $\phi_0^{\pm} \neq 0°$ or 180° can be observed. For the ↑↓-DW, $\phi_0^+ \approx 45°$ and $\phi_0^- \approx 240°$. For the ↓↑-DW,

$\phi_0^+ \approx 150°$ and $\phi_0^- \approx 330°$. A comparison of the results for the ↑↓- and ↓↑-DW yields roughly a relative tilt, $\Delta\phi \approx 90°$, between the depinning efficiencies.

This result cannot be explained by the simple 1D model of a DW. Instead one has to include further effects to explain the observed angular dependencies. In the following we discuss some of the possible effects leading to a tilted maximum depinning efficiency.

As described in section 2.4, the DW is treated in the 1D model as a quasi-particle and is described by collective coordinates, i.e. the center of mass, x, and the tilting angle of the DW, ψ. Hereby, the actual shape of the DW is assumed to be always straight and all internal spins of the DW are pointing homogeneously in the same direction. In reality however, this might not always be the case and the 1D model is not sufficient anymore to explain the results. In our DW depinning experiments the DW is pushed through a non-trivial Hall cross type geometry, thus the geometry of the pinning site in our experiment can be expected to distort the shape of the DW significantly. Micro-magnetic simulations reveal that the DW is transformed from a ideal straight DW into a half circle structure during the depinning process[135]. This is similar to blowing a soap-bubble from a surface. However, the deviation of the wall shape from a straight wall has dramatic consequences, on the STT and SOT induced DW depinning behavior.

Due to the deformation of the DW shape the current direction is not necessarily perpendicular to the DW everywhere. The combination of the local current distribution and the local DW spin-structure can result in partly varying relative angles between the spin orientation of the conduction electrons and the local magnetization direction, which results in different velocities for different parts of the DW. Recent studies, e.g. by C. K. Safeer et al.[136,137] support this explanation.

The probably most important influence on the depinning process is the arbitrary distribution of the pinning sites in the area of the Hall cross, which can determine locally the spin-structure orientation and as a result the direction of maximum depinning angle.

To support or crosscheck our experimental data, micro-magnetic simulations have been performed by E. Martinez and co-workers. Doing so, they found that another possible effect influencing the DW depinning process can be the nucleation of Bloch lines inside the DW. However since this effect is out of scope, we will not discuss this effect here further.

Lastly, as another possible reason micro magnetic simulations revealed, that if the applied in-plane magnetic field is not strong enough to saturate the DW wall completely e.g. into a perfect Néel type DW in the perpendicular current scenario or perfect Bloch type DW when current is applied parallel to the wall, this can result as well in a tilting of the depinning efficiency. From the amplitude scans (see subsection 6.4.1 or Fig. 6.5) we extracted that the wall is saturated for an in-plane field amplitude of ≈ 40 mT. However, maybe that is not completely the case and a slightly lower field value is already sufficient to change the maximum depinning efficiency direction significantly. Further studies can shine more light on that.

In sum the maximum efficiency angle, $\phi_0^\pm$, depends crucially on the specific local DW configuration at the Hall cross. The internal spin-structure can be expected to deviate from the ideal straight DW, where the internal spin-structure direction is parallel to the externally applied in-plane field. However, from the pure transport measurements performed within this thesis we can not unambiguously identify the mechanism leading to the specific tilting angle of the angular dependence, $\phi_0^\pm$.

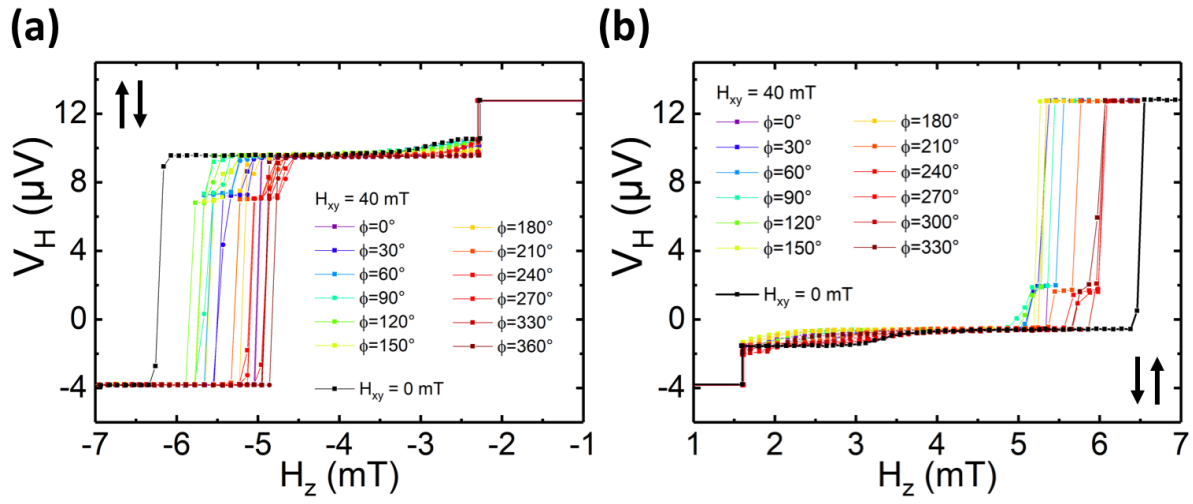

Abbildung 6.7: EHE signature measured during depinning scheme. (a) & (b) show the EHE signature for various polar angles ϕ of the in-plane field for ↑↓- & ↓↑-DW respectively.

By analyzing the individual Hall signals for different polar angles, ϕ, variations in the pinning levels can be observed during the depinning measurement (Fig. 6.7). Since the DW does not follow the same pinning trajectory as ϕ is varied, we conclude that for each ϕ, variations of the material parameters can be expected locally e.g. anisotropy, DMI and demagnetization fields. This means that even if an external in-plane field is applied in a certain direction, not all of the spins inside the DW are necessarily pointing into the field direction, but instead can have a different directions within the x-y-plane. To resolve the origin of the tilting angle of the maximum torque efficiency, we suggest further spin-resolved imaging, e.g. nitrogen-vacancy center microscopy[138], that allows to detect the internal spin-structure of the DW during the depinning process.

However, having found that the angular scans of the depinning fields in the polar plane can result in tilting angles $\phi_0^{\pm} \neq 0°$ or 180°, respectively, we can contribute the non-zero depinning efficiencies found with the depinning experiments, where an in-plane field was applied in the transverse direction in subsection 6.4.1 to a tilt of the $\cos^2(\phi)$-dependence itself by $\phi_0^{\pm}$.

6.5 Current-induced DW depinning for current flowing along a DW

Following the SOT model, a DW depinning process should be possibly also with current applied parallel to the wall. This is allowed from symmetry considerations and has been e.g. theoretically predicted by K. Hals & A. Brataas[139] and numerically studied e.g. by A. V. Khvalkovskiy et al.[140] prior to this work. However, it has not been studied experimentally previously.

Different from the ⊥-case, where the action of the SOTs is maximized for a Néel wall, leading to a $\cos^2(\phi - \phi_0^{\pm})$-dependence of the angular depinning scan, the action of the SOTs in the ||-case is

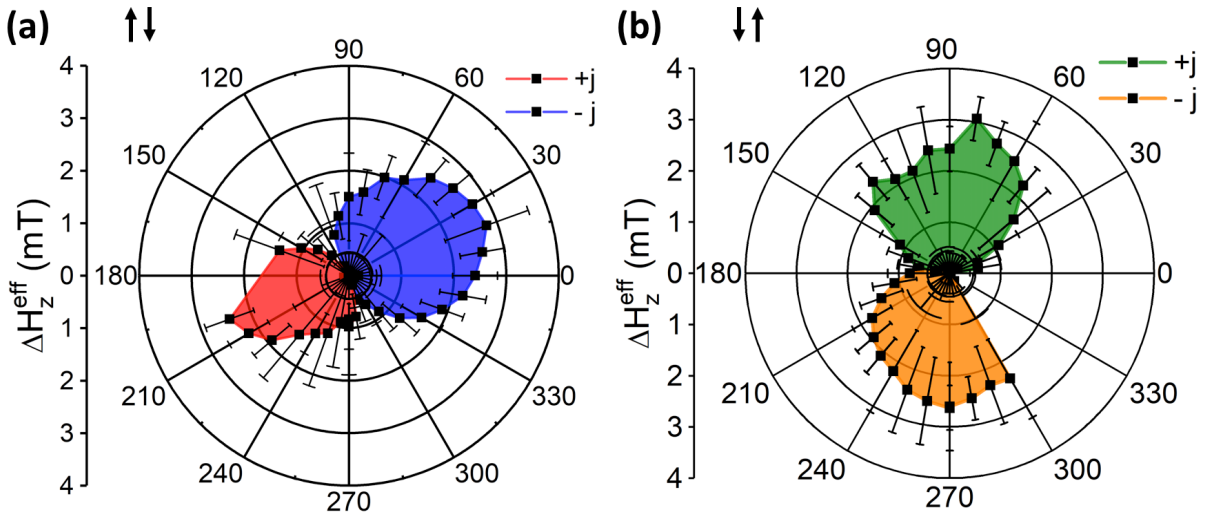

Abbildung 6.8: Angular dependent depinning efficiency for current injected parallel to a ↑↓- (a) & ↓↑-DW (b).

expected to be maximized for a DW being in the Bloch configuration, which leads accordingly to a $\sin^2(\phi - \phi_0^{\pm})$-dependence.

To test this, we measure again the angular dependence of the depinning field, but this time with a current applied along the Hall cross of the sample.

In order to compare the strength of the acting torques for both geometries, we perform the angular scan at the same in-plane field amplitude of $|H_{x,y}| = 40$ mT and at the same current density for the ∥-case as used for the ⊥-case ($j_{\parallel} = j_{\perp} = 6.4 \times 10^{10}\mathrm{A/m^2}$).

Fig. 6.8 (a) & (b) show the results of these measurements for both DW scenarios, the ↑↓ & ↓↑-DW.

First, we analyze the scenario for the ↓↑-DW, Fig. 6.8 (b). Here, the current is applied in the -y (+y) direction, indicated by the green (orange) color coding. As expected from the SOT-model, the depinning efficiency is maximized for a current applied parallel to the field direction, but this time the in-plane field tunes the DW into a Bloch wall configuration. For the ↓↑-DW we find the predicted $\sin^2(\phi - \phi_0^{\pm})$-dependence with $\phi_0^{\pm} \approx 0°$, which, this time, is in line with the simple 1D model.

In contrast, the depinning measurement for a ↑↓-DW and current applied parallel to the DW shows an unexpected large deviation of $\phi_0^{\pm} \neq 0°$. This can be explained in a similar way as for the deviations found in the case, where current has been flowing perpendicular to the DW in section 6.4.

However, comparing only the maximum efficiencies for both current scenarios, current applied perpendicular and parallel to the DW, we find within the error bars similar effective DW depinning fields, $\Delta H_z^{\mathrm{eff}} \approx 2$ mT for $j_{\parallel} = j_{\perp} = 6.4 \times 10^{10}\mathrm{A/m^2}$. This is in line with the SOT model developed from K. Hals et al.[139], where the anti-damping SOT is rotational invariant in the polar plane. Since we find a similar SOT efficiency, we conclude that no other large torques are present in the Ta / CoFeB / MgO multilayer system, e.g. the classical STT or other relativistic dissipative torques, such as also derived by K. Hals et al.[139].

7 Comparison of DW depinning fields calculated from torque magnetometry and real DW depinning experiments

In chapter 4, we performed full angular SOT magnetometry measurements to determine the SOT-efficiency for current acting on a homogeneous spin-texture. Based on that, we calculated in section 4.4 the net SOT efficiency for a Néel type DW and calculated in section 4.5 the corresponding DW depinning fields using the 1D model. As a result, we found a maximal DW depinning efficiency for an ideal Néel type DW of $\approx (2.45 \pm 0.5)\ \mathrm{mT}/10^{11}\mathrm{A/m}^2$.

In section 6.4 and 6.5, we measured the current-induced DW depinning efficiency for real ↑↓- & ↓↑-DWs, experimentally. In order to study the strength of the acting torques and their symmetry, we manipulated the internal magnetic spin-structure with a magnetic field applied within the polar plane. Doing so, we found an unexpected tilt, of the maximum depinning efficiency within the polar plane, which we attributed to the complex internal structure and non-trivial form of a DW depinned through a Hall cross geometry. However, if we neglect this tilting of the maximum depinning efficiency and only extract the maximum torque efficiency, we found a similar maximum efficiency of $\approx (3.13 \pm 0.5)\ \mathrm{mT}/10^{11}\mathrm{A/m}^2$, independent of the DW type and the applied current direction.

The overall goal of this thesis was to study the SOT-model in our Ta/CoFeB/MgO multilayer system and compare the two different experimental measurement methods, the torque magnetometry method based on a higher harmonics analysis of the EHE and real DW depinning experiments. Doing so, we find in general a good overall agreement between these two methods. However, looking in more detail, it is clear, that aspects, such as the internal spin-texture configuration in a real DW depinning experiment can differ significantly from an ideal Néel type DW configuration. In specific the angular dependent depinning measurements showed completely different tilting angles for the ↑↓- & ↓↑-DW depinning measurements as well as for both current direction scenarios. As, already suggested in subsection 6.4.2, only by including the complex internal spin-structure & shape of the DW, as well as the specific pinning landscape inside the Hall cross, one can possibly get a better understanding of the complex depinning process and therefore to a more solid statement on the comparability of the two measurement approaches.

8 Summary, conclusion and outlook

8.1 Recap of the thesis goals

In the perspective of a possible application in a DW-based memory device such as the racetrack memory device, the overall goal of this thesis was to study the acting torques in the high-anisotropy HM/FM/Oxide multilayer system, Ta/CoFeB/MgO.

Recently, before this thesis work, ultra-efficient DW motion has been observed in similar multilayer nano-structures and led to the development of the state-of-the art SOT model in order to explain the observations.

It was found that the torques present in such systems are typically present as a mixture of multiple SOT contributions, originating e.g. from the SHE and from the ISGE.

Following this model, one expects a maximum torque efficiency on the DW, when the SOTs generated in the HM-layer are acting on a Néel type DW, if current is flowing perpendicular to the DW profile. If the current is instead applied parallel to the DW, the SOTs should be maximized for a Bloch type DW configuration and vanish for a Néel wall.

Recently, a novel measurement method, i.e. the torque magnetometry method, has been developed. This promising method allows to measure the SOTs of a system by using a higher harmonics analysis of the AHE. However, the technique allows to measure only the torques acting on homogeneous macro-spin structures.

Before this thesis it has not experimentally been confirmed, that the net action of the SOTs, measured for such a macro spin-structure by using e.g. the torque magnetometry method is actually consistent with the net effective torque acting on complex spin structures such as DWs, which generically consists of spins pointing in various directions. The main goal of this thesis was to verify this connection and to test the predictive power of the spin torque magnetometry method for DW motion properties.

In order to test this assumption, we performed both, torque magnetometry, as well as DW depinning measurements on the same sample and on the same Hall cross geometry. Using the current-field equivalence the net action of the SOTs could then be determined in the form of an effective torque efficiency and both methods could be compared.

Next to this main question we were also interested in the material properties of our multilayer stack itself, in particular in the size of the FL- and AD-like SOTs and the classical STT. Additionally we wanted to test the predicted symmetry of the SOTs according to the SOT and DMI model.

8.2 Summary of this thesis

In order to tackle the main research question we started in chapter 4 to perform torque magnetometry measurements on the Ta/CoFeB/MgO multilayer nano-structure. Here, we first measured the SOTs with the torque magnetometry method for all polar angles in the longitudinal and transverse direction and integrated the results according to a Néel type DW profile. Having the effective torque field calculated, we used it in a DW depinning simulation calculation and determined an expected effective depinning field for a Néel type DW.

The first key observation here was that one has to take into account the geometrical $\pi/2$ factor originating from the integration over the Néel type DW profile. This has been mentioned already by A. Thiaville et al. before[19]. We confirmed this within this thesis experimentally. **The second key observation** was that the FL-torque has only little influence on the DW depinning process. The exact reason is not fully clear and needs further investigations, which was not within scope of this thesis. **The third key observation** was that the AD-like torque for Ta/CoFeB/MgO is only weakly angular dependent. This makes the whole angular dependent measurement scheme more or less negligible in order to determine the effective DW depinning fields for our sample. However, this might not be the case for other material systems.

The next step was to measure the actual effects of the acting spin-torques on real DWs. For this we performed DW depinning experiments. In order to be able to study the DW depinning systematically, we first needed a reliable DW writing scheme. In chapter 5 we characterized our sample and determined the critical parameters for a reliable nucleation scheme for ↑↓- & ↓↑-DWs.

In chapter 6 we finally studied the depinning of DWs using the Hall cross geometry. For this we first performed reference measurements in the form of purely field-induced DW depinning measurements. Later we used those measurements to analyze the current-induced DW depinning.

As a first result we found that the FID depends linearly on the applied in-plane field and decreases with increasing in-plane field amplitude. This was explained by a shift of the Walker breakdown at larger in-plane field. This can be explained by assuming that the DW becomes more rigid and can therefore move more easily across pinning sites. Correspondingly the FID occurs already at smaller out-of-plane magnetic fields. These results were also confirmed by 1D model calculations made by Eduardo Martinez.

Next, we measured the FID for various polar angles at a fixed in-plane magnetic field amplitude. **As a second result** we found that the FID is isotropic. This result is a key requisite in order to analyze the CID measurements, since each angular dependence within the CID measurements will therefore reflect directly the angular dependence of the SOTs. This allowed us to detect the symmetry of the SOTs, which are acting on the DWs and are responsible for the current-induced depinning process.

The CID measurements were split into two parts. First, the measurements for current applied perpendicular to the DW and second, measurements with current applied parallel to the DW.

In order to study the SOT efficiency we first performed an amplitude scan for in-plane magnetic fields applied in the longitudinal and transverse direction. In the longitudinal direction we found

the expected result in line with the SOT model, which describes a systematically increasing DW depinning efficiency for one combination of current polarity and in-plane field direction and zero efficiency for the opposite current polarity. Consequently, if the applied field direction is reversed the non-zero current polarity is also reversed.

For the transverse direction however, we found exactly the same behavior, which was not expected accordingly to the SOT model. The SOT model predicts zero efficiency for all combinations of current polarity and applied field in the transverse direction. We investigated this further and performed a complete polar angular scan. This finally helped us to resolve the issue. As a result we found that the DW depinning efficiency shows indeed the expected $\cos^2$-dependence, as the SOT model predicts, but with an unexpected tilted symmetry. We performed further DW depinning measurements for multiple combinations of ↑↓- & ↓↑-DWs and both current directions and found in sum a seemingly arbitrary tilting angle.

After we found this unexpected tilting behavior of the maximum torque efficiency, we investigated additionally the scenario for current applied parallel to the wall. Here we found that the expected maximal torque efficiency for a Bloch wall only for the ↓↑-DW. For the ↑↓-DW we found again a strongly tilted symmetry of the torque efficiency.

In order to explain all these results we discussed two main reasons:
First, a net non-zero parallel current component, which can be present due to multiple reasons itself, such as impurities or Bloch lines affecting the internal spin-structure of the DW and e.g. can give rise to a non-perfect asymmetric curvature of the pinned DW inside the Hall cross geometry.

As a second possible reason we have discussed that the applied field is maybe not enough to saturate the wall, which can result as well in a tilting of the depinning efficiency.

In sum, we observed that the DW depinning efficiency can be strongly manipulated using in-plane magnetic fields, which we used to determine the symmetry of the acting torques. From the SOT model a maximum torque is predicted for the longitudinal field direction for current applied perpendicular to the wall and for the transverse field direction, if current is applied parallel to the DW. In our experiments we could not confirm this behavior and instead found ambiguous results.

We emphasize that DW depinning through a Hall cross geometry is a extremely complex non-linear process. In order to shine more light into the processes involved we conclude that simultaneous optical measurements, e.g. nitrogen-vacancy center microscopy[138], which allow to determine the exact internal spin-structure of the DW during the depinning process are necessary.

Coming back to our overarching objective this means that we can only argue qualitatively within this thesis. Comparing all cases of ↑↓- & ↓↑-DWs and both polarities of the applied current we recognize that we measured very similar maximum DW depinning efficiencies of $\approx 3.1\mathrm{mT}/10^{11}\mathrm{A/m}^2$. Compared to the calculated maximum depinning efficiency of $\approx 2.5\mathrm{mT}/10^{11}\mathrm{A/m}^2$ based on the SOT effective fields obtained with the torque magnetometry measurements one can indeed find extraordinary good consensus. However a non-ambiguous validation of the predictive power of the novel torque magnetometry method regarding the DW motion properties can not be given with this thesis and requires further investigations.

8.3 Outlook

This thesis gives interesting new insights into the angular dependence of the current-induced SOTs that are acting on DWs. However, in order to be able to make more sophisticated statements concerning the origin of the observed angular dependencies simultaneous optical measurements would be beneficial and are highly recommended.

The comparison of the SOTs acting on a macro-spin structure with the measurements of collective SOTs acting on complex spin-textures can give a new access to study geometrical effects or geometrical defects of the DW, such as defects and Bloch-lines inside the complex spin-texture.

We further recommend to repeat the DW depinning measurement for more samples and also test different material systems in order to study the variation of the angular dependencies and maybe find generic features for different material systems.

A Classical determination method for β

In the classical STT-model all effects of the current acting on a DW and leading to DW depinning can be described with the adiabatic and non-adiabatic STT-terms in the LLG-equation (see section 2.4). The strength of these two terms can be determined within a current-induced DW depinning experiment by using the current-field-equivalence principle[10,49,50].

We start with the already established DW depinning measurement scheme, that we used for the field-induced depinning and support the depinning process with an additionally applied current pulse across the DW.

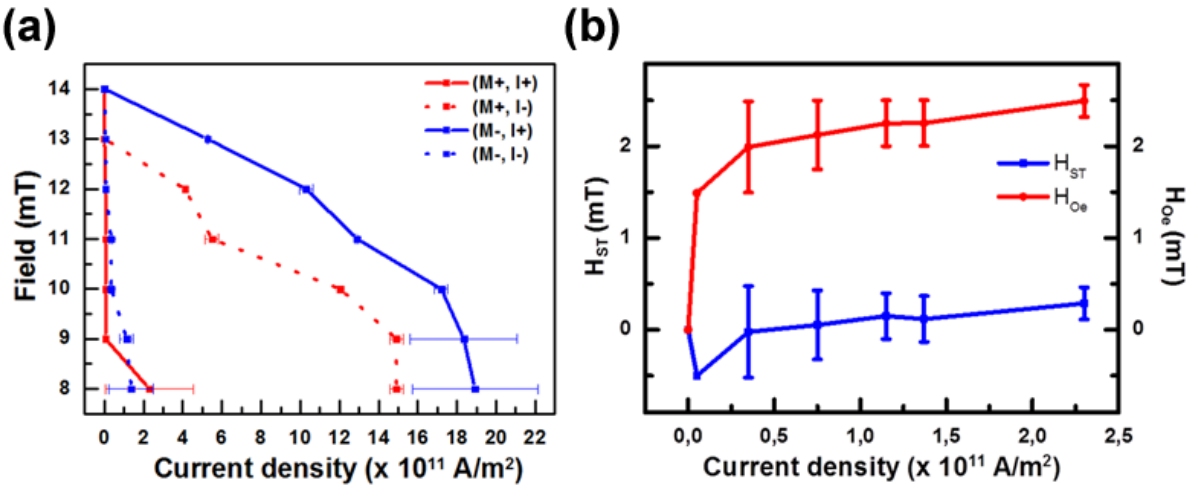

Abbildung A.1: Current induced DW depinning measurement results without in-plane field. (a) Depending on the combination of current direction, $I\pm$, and the type of DW, UD or DU DW, indicated by $M+$, and $M-$, respectively, the critical field decreases differently as a function of applied current density. Using the current-field-equivalence principle and unique symmetry considerations for the Joule heating, the Oersted field, H_{Oe} and the STT effective field, H_{ST} [10,49,50], one can extract the H_{Oe} and H_{ST} as a function of current density, shown in Fig. (b). From the slope of $H_{ST}(j)$ the non-adiabatic β-parameter can be determined.

In Fig. A.1 (a) the experimental results of the current-induced DW depinning fields for a 200 nm wide nanowire are shown. We find a critical out-of-plane field of $\approx$ 14 mT for the purely field-induced depinning. It can be seen, that with increasing current density, j, applied during the depinning process the out-of-plane field necessary to depin a DW is reduced significantly. In order to distinguish between heating, Oersted field effect and the acting effective spin-torque-fields we perfom the measurement for positive and negative current polarity and for both DW configurations (UD and DW DWs, indicated by M+ and M- in Fig. A.1 (a)).

We find that for the combinations M+ with I- and M- with I+ the DW can be successfully pushed through the Hall cross. This odd symmetry reflects the negative sign of the spin-Hall angle of the Ta- bottom layer, in line with other publications[76]. Fig. A.1 (b) shows the resulting effective Oe-field and spin-torque field, H_{Oe}, and H_{ST}, respectively. From the slope of $H_{ST}(j)$ the non-adiabatic β-parameter can be determined. For our test sample, $\beta \approx 0.13$, which is in line with results from other research groups[76].

However, since the discovery that the DW dynamics in HM/FM/Oxide systems is dominated from the acting SOTs in combination with the internal DMI present at the interfaces, it is clear, that the classical STT only cannot describe the systems DW motion properties appropriately.

B Torque magnetometry analysis protocol

In this chapter we report a detailed list of analysis steps that we used to analysis the torque magnetometry measurement data within the intermediate polar angular regime (see subsection 4.3.2).

The raw-datasets for the longitudinal or transverse direction consists both of the following four data columns:

1. The applied magnetic field, $\boldsymbol{H}$,
2. the first harmonics Hall signal, $V_H^{1\omega}$
3. the second harmonics Hall signal, $V_H^{2\omega}$ and
4. the longitudinal voltage drop across the sample, V_{xx}.

The following data analysis can be split into two parts. First a preparation of the datasets, and second an iterative fitting procedure, which allows to disentangle the longitudinal and transverse SOT effective fields H_L & H_T, which are originally mixed in the higher harmonics torque magnetometry.[87,101]

Part I - Preparation of the measurement datasets:

1. First, we calculate the ac-current injected into the nanowire with $i = V_{xx}/50\Omega$ (see Fig. 4.2).
2. With i, we can translate the measured voltage signals, $V_H^{1\omega}$ and $V_H^{2\omega}$, into the corresponding Hall resistances by using $R_H^{1\omega} = V_H^{1\omega}/i$ and $R_H^{2\omega} = V_H^{2\omega}/i$.
3. Having this, we can derive the derivative of the first harmonics resistance $\frac{dR_H^{1\omega}}{dH}$
4. Next, we calculate the equilibrium angle of the magnetization vector, $\theta(\boldsymbol{M}(\boldsymbol{H}))$, which depends on the applied magnetic field vector, $\boldsymbol{H}$. This can be done by first normalizing the first harmonics Hall resistance, $R_H^{1\omega}(H)$, to values between 0 and 1 and then using $R_{H,\,Normalized}^{1\omega}(H)$ to calculate $\theta = \arccos(\frac{R_{H,\,Normalized}^{1\omega} - 0.5}{0.5})\frac{180^\circ}{\pi}$
5. Next, we calculate $\sin^2\theta$ and $\sin(\theta_H - \theta)$, with θ_H being the out-of-plane tilting angle used for the field-scan (in rad).

These steps have to be performed for both, the longitudinal and transverse measurement datasets, individually. Now, we have all ingredients in place to start the iterative fitting procedure to extract H_L & H_T.

Part II - Iterative fitting procedure:

1. First, we calculate an initial estimators for the SOT effective fields in the longitudinal and transverse direction, H_L, H_T, respectively. This can be done by neglecting for a moment the

2nd harmonics Hall signal contribution originating from the PHE ($\Delta_{PHE} = 0$). Following Ref.[87,101] this yields:

$$H_L^{0th} = -R_{H,L}^{2\omega} \cdot \frac{\sin(\theta_H - \theta)}{dR_{H,L}^{1\omega}/dH}. \tag{B.1}$$

$$H_T^{0th} = -R_{H,T}^{2\omega} \cdot \frac{\sin(\theta_H - \theta)}{\cos\theta \cdot dR_{H,L}^{1\omega}/dH}. \tag{B.2}$$

2. Next, we plot H_T^{0th} as a function of $\sin^2\theta$ and use a 2nd order polynomial fit, $y = a_T^{0th} + b_T^{0th} \cdot x + c_T^{0th} \cdot x^2$. a_T^{0th} can now be used to calculate the 1st order estimator for the effective longitudinal field:

$$H_L^{1st} = -\frac{R_{H,L}^{2\omega} - 2 \cdot \Delta_{PHE} \cdot \frac{sin^2(\theta)}{|H(\theta_H,\phi_H)|} \cdot sin(\theta_H) \cdot a_T^{0th}}{dR_{H,L}^{1\omega}/dH} \cdot sin(\theta_H - \theta). \tag{B.3}$$

Here, Δ_{PHE} is the PHE ratio, which has been experimentally determined for the Ta/CoFeB/MgO multilayer sample used in this thesis to $\Delta_{PHE} \approx 0.054 \approx 5\ \%$.

3. Next, we plot H_L^{1st} vs. $\sin^2(\theta)$ and use again a 2nd order polynomial fit, $y = a_L^{1th} + b_L^{1th} \cdot x + c_L^{1th} \cdot x^2$. Now, a_L^{1st} can be used to calculate the 2nd order estimator, but for the transverse effective field, H_T with

$$H_T^{2nd} = \frac{R_{H,T}^{2\omega} + 2 \cdot \Delta_{PHE} \cdot \frac{sin^2(\theta)}{|H(\theta_H,\phi_H)|} \cdot \frac{\cos(\theta)}{\sin(\theta_H)} \cdot a_L^{1st}}{dR_{H,T}^{1\omega}/dH} \cdot \frac{\sin(\theta_H - \theta)}{-\cos(\theta)} \tag{B.4}$$

4. Next, we plot H_T^{2nd} vs. $\sin^2(\theta)$ and fit again a 2nd order polynomial, $y = a_T^{2nd} + b_T^{2nd} \cdot x + c_T^{2nd} \cdot x^2$ and determine a_T^{2nd}. a_T^{2nd} can now be used to calculate the next higher order estimator for the longitudinal effective field, H_L^{3rd}, by using Eq. B.3, where a_L^{0th} is replaced with a_T^{2nd}
5. In an analog way, with a_L^{3rd} from another 2nd order fit to the H_L^{3rd} curve, we can calculate H_T^{4th} and so forth.

This iterative fitting approach can then be repeated until the estimators, H_L^{Nth} & H_T^{Nth} converge for the N-th order (see Fig. 4.6). Those values represent the terminal estimates for the SOT effective fields H_L & H_T.

Acknowledgments have been removed for data privacy protection reasons.

Acknowledgments have been removed for data privacy protection reasons.

CV has been removed for data privacy protection reasons.

CV has been removed for data privacy protection reasons.

Publication List

1. **Modification of Dzyaloshinskii-Moriya interaction stabilized domain wall chirality by driving currents**, G.V. Karnad, F. Freimuth, E. Martinez, R. Lo Conte, G. Gubbiotti, **T. Schulz**, S. Senz, B. Ocker, Y. Mokrousov, and M. Kläui. Phys. Rev. Lett. 121, 147203 (2018).
2. **Study of energetics of 360° domain walls through annihilation**, G. V. Karnad, E. Martinez, M. Voto, **T. Schulz,** B. Ocker, D. Ravelosona, and M. Kläui. Under review.
3. **Role of phonon skew scattering in the spin Hall effect of platinum**, G. V. Karnad, C. Gorini, K. Lee, **T. Schulz**, R. Lo Conte, A. W. J. Wells, D.-S. Han, K. Shahbazi, J.-S. Kim, T. A. Moore, H. J. M. Swagten, U. Eckern, R. Raimondi, and M. Kläui. Phys. Rev. B 97, 100405(R) (2018).
4. **Effective field analysis using the full angular spin-orbit torque magnetometry dependence**, **T. Schulz**, K. Lee, B. Krüger, R. Lo Conte, G. V. Karnad, K. Garcia, L. Vila, B. Ocker, D. Ravelosona and M. Kläui. Phys. Rev. B 95, 224409 (2017).
5. **Ferromagnetic layer thickness dependence of the Dzyaloshinskii-Moriya interaction and spin-orbit torques in Pt\Co\AlOx**, R. Lo Conte, G. V. Karnad, E. Martinez, K. Lee, N.-H. Kim, D.-S. Han, J.-S. Kim, S. Prenzel, **T. Schulz**, C.-Y. You, H. J. M. Swagten and M. Kläui. AIP Advances 7, 065317 (2017).
6. **Origin of the spin Seebeck effect in compensated ferrimagnets**, S. Geprägs, A. Kehlberger, F. Della Coletta, Z. Qiu, E.-J. Guo, **T. Schulz**, C. Mix, S. Meyer, A. Kamra, M. Althammer, H. Huebl, G. Jakob, Y. Ohnuma, H. Adachi, J. Barker, S. Maekawa, G. E. W. Bauer, E. Saitoh, R. Gross, S. T. B. Goennenwein and M. Kläui. Nature Communications 7, 10452 (2016).
7. **Spin-orbit torques for current parallel and perpendicular to a domain wall**, **T. Schulz**, O. Alejos, E. Martinez, K. M. D. Hals, K. Garcia, L. Vila, K. Lee, R. Lo Conte, G. V. Karnad, S. Moretti, B. Ocker, D. Ravelosona, A. Brataas and M. Kläui. Appl. Phys. Lett. 107, 122405 (2015).
8. **Role of B diffusion in the interfacial Dzyaloshinskii-Moriya interaction in Ta / $Co_{20}Fe_{60}B_{20}$ / MgO nanowires**, R. Lo Conte, E. Martinez, A. Hrabec, A. Lamperti, **T. Schulz**, L. Nasi, L. Lazzarini, R. Mantovan, F. Maccherozzi, S. S. Dhesi, B. Ocker, C. H. Marrows, T. A. Moore, and M. Kläui. Phys. Rev. B 91, 014433 (2015).
9. **Dynamics and inertia of skyrmionic spin structures**, F. Büttner, C. Moutafis, M. Schneider, B. Krüger, C. M. Günther, J. Geilhufe, C. v. Korff Schmising, J. Mohanty, B. Pfau, S. Schaffert, M. Foerster, **T. Schulz**, C. A. F. Vaz, J. Franken, H. J. M. Swagten, M. Kläui, and S. Eisebitt. Nature Physics 11, 225-228 (2015).
10. **Synchronous precessional motion of multiple domain walls in a ferromagnetic nanowire by perpendicular field pulses**, J.-S. Kim, M.-A. Mawass, A. Bisig, B. Krüger, R. M.

Reeve, **T. Schulz**, F. Büttner, J. Yoon, C.-Y. You, M. Weigand, H. Stoll, G. Schütz, H. J. M. Swagten, B. Koopmans, S. Eisebitt and M. Kläui. Nature Communications 5, 3429 (2014).

11. **Spin-orbit torque-driven magnetization switching and thermal effects studied in Ta \ CoFeB \ MgO nanowires**, R. Lo Conte, A. Hrabec, A. P. Mihai, **T. Schulz**, S.-J. Noh, C. H. Marrows, T. A. Moore, and M. Kläui. Applied Physics Letters 105, 122404 (2014).

12. **Efficient spin transfer torque in $La_{2/3}Sr_{1/3}MnO_3$ nanostructures**, M. Foerster, L. Peña, C. A. F. Vaz, J. Heinen, S. Finizio, **T. Schulz**, A. Bisig, F. Büttner, S. Eisebitt, L. Méchin, S. Hühn, V. Moshnyaga, and M. Kläui. Applied Physics Letters 104, 072410 (2014).

13. **Extraordinary Hall effect in Pt- or Ni-based multilayer stacks with strong perpendicular magnetic anisotropy**, J. Heinen, **T. Schulz**, J. Gerhard, O. Boulle, G. Malinowski, H. Swagten, B. Koopmans, C. Ulysse, G. Faini, B. Ocker, J. Wron, S.-M. Ahn, N.-M. Nguyen, D. Ravelosona and M. Kläui. Journal of the Korean Physical Society, Volume 62, Issue 10, 1399-1403 (2013).

References

[1] M. N. Baibich, J. M. Broto, A. Fert, F. N. Van Dau, F. Petroff, P. Etienne, G. Creuzet, A. Friederich, and J. Chazelas. Giant Magnetoresistance of (001)Fe/(001)Cr Magnetic Superlattices. *Phys. Rev. Lett.*, **61**(21):2472–2475, 1988.

[2] T. Coughlin. 20 TB Hard Disk Drives, The Future Of HDDS, 2017. URL: https://www.forbes.com/sites/tomcoughlin/2017/01/28/20-tb-hard-disk-drives-the-future-of-hdds/.

[3] White paper - Digital data storage outlook 2017, 2017. URL: https://www.spectralogic.com/wp-content/uploads/white-paper-digital-data-storage-outlook-2017-v3.pdf.

[4] M. V. Fischetti, B. Fu, and W. G. Vandenberghe. Theoretical Study of the Gate Leakage Current in Sub-10-nm Field-Effect Transistors. *IEEE Trans. Electron Devices*, **60**(11): 3862–3869, 2013.

[5] J. S. Meena, S. M. Sze, U. Chand, and T.-Y. Tseng. Overview of emerging nonvolatile memory technologies. *Nanoscale Res. Lett.*, **9**:526, 2014.

[6] S. S. P. Parkin, M. Hayashi, and L. Thomas. Magnetic domain-wall racetrack memory. *Science*, **320**(5873):190–194, 2008.

[7] J.-S. Kim, M.-A. Mawass, A. Bisig, B. Krüger, R. M. Reeve, T. Schulz, F. Büttner, J. Yoon, C.-Y. You, M. Weigand, H. Stoll, G. Schütz, H. J. M. Swagten, B. Koopmans, S. Eisebitt, and M. Kläui. Synchronous precessional motion of multiple domain walls in a ferromagnetic nanowire by perpendicular field pulses. *Nat. Commun.*, **5**, 2014.

[8] J. C. Slonczewski. Current-driven excitation of magnetic multilayers. *J. Magn. Magn. Mater.*, **159**(1):L1–L7, 1996.

[9] L. Berger. Emission of spin waves by a magnetic multilayer traversed by a current. *Phys. Rev. B*, **54**(13):9353–9358, 1996.

[10] J. Heinen. Current-induced Domain Wall Dynamics Probed by Electrical Transport Measurements. Dissertation, Universität Konstanz, 2012. URL: https://kops.uni-konstanz.de/handle/123456789/19846.

[11] K. Seshan. Handbook of thin-film deposition processes and techniques: principles, methods, equipment, and applications. Noyes Publications, Norwich, N.Y, 2nd ed edition, 2002. ISBN 978-0-8155-1442-8. URL: http://www.sciencedirect.com/science/book/9780815514428.

[12] S. Blundell. Magnetism in Condensed Matter. OUP Oxford, 2001. ISBN 978-0-19-850591-4. URL: http://www.oupcanada.com/catalog/9780198505914.html.

[13] J. M. D. Coey. Magnetism and Magnetic Materials. Cambridge University Press, 2010. ISBN 978-0-521-81614-4. URL: https://doi.org/10.1017/CBO9780511845000.

[14] N. W. Ashcroft and N. D. Mermin. Festkörperphysik. De Gruyter, Berlin, Boston, reprint 2014 edition, 2001. ISBN 978-3-486-24834-0. URL: https://www.degruyter.com/view/product/214257.

[15] G. Bihlmayer. Density-functional Theory of Magnetism. In *Handbook of Magnetism and Advanced Magnetic Materials*. John Wiley & Sons, Ltd, 2007. ISBN 978-0-470-02218-4. URL: https://doi.org/10.1002/9780470022184.hmm101.

[16] I. Dzyaloshinsky. A thermodynamic theory of "weak" ferromagnetism of antiferromagnetics. *J. Phys. Chem. Solids*, **4**(4):241–255, 1958.

[17] T. Moriya. Anisotropic superexchange interaction and weak ferromagnetism. *Phys. Rev.*, **120**(1):91, 1960.

[18] S. Emori, U. Bauer, S.-M. Ahn, E. Martinez, and G. S. D. Beach. Current-driven dynamics of chiral ferromagnetic domain walls. *Nat. Mater.*, **12**(7):611–616, 2013.

[19] A. Thiaville, S. Rohart, Jué, V. Cros, and A. Fert. Dynamics of Dzyaloshinskii domain walls in ultrathin magnetic films. *EPL*, **100**(5):57002, 2012.

[20] K.-S. Ryu, L. Thomas, S.-H. Yang, and S. Parkin. Chiral spin torque at magnetic domain walls. *Nat. Nanotechnol.*, **8**(7):527–533, 2013.

[21] K.-S. Ryu, S.-H. Yang, L. Thomas, and S. S. P. Parkin. Chiral spin torque arising from proximity-induced magnetization. *Nat. Commun.*, **5**:3910, 2014.

[22] S.-G. Je, D.-H. Kim, S.-C. Yoo, B.-C. Min, K.-J. Lee, and S.-B. Choe. Asymmetric magnetic domain-wall motion by the Dzyaloshinskii-Moriya interaction. *Phys. Rev. B*, **88**(21):214401, 2013.

[23] R. Lo Conte, E. Martinez, A. Hrabec, A. Lamperti, T. Schulz, L. Nasi, L. Lazzarini, R. Mantovan, F. Maccherozzi, S. S. Dhesi, B. Ocker, C. H. Marrows, T. A. Moore, and M. Kläui. Role of B diffusion in the interfacial Dzyaloshinskii-Moriya interaction in Ta / Co 20 F e 60 B 20 / MgO nanowires. *Phys. Rev. B*, **91**(1):014433, 2015.

[24] T. l. A. Aharoni. Introduction to the Theory of Ferromagnetism. International Series of Monographs on Physics. Oxford University Press, Oxford, New York, second edition edition, 2001. ISBN 978-0-19-850809-0. URL: https://global.oup.com/academic/product/introduction-to-the-theory-of-ferromagnetism-9780198508090.

[25] T. W. McDaniel. Ultimate limits to thermally assisted magnetic recording. *J. Phys.: Condens. Matter*, **17**(7):R315, 2005.

[26] M. Kryder, E. Gage, T. McDaniel, W. Challener, R. Rottmayer, Ganping Ju, Yiao-Tee Hsia, and M. Erden. Heat Assisted Magnetic Recording. *Proc. IEEE*, **96**(11):1810–1835, 2008.

[27] F. Bloch. Zur Theorie des Austauschproblems und der Remanenzerscheinung der Ferromagnetika. *Z. Physik*, **74**(5-6):295–335, 1932.

[28] L. Néel. Anisotropie magnétique superficielle et surstructures d'orientation. *J. Phys. Radium*, **15**(4):225–239, 1954.

[29] M. J. Benitez, A. Hrabec, A. P. Mihai, T. A. Moore, G. Burnell, D. McGrouther, C. H. Marrows, and S. McVitie. Magnetic microscopy and topological stability of homochiral Néel domain walls in a Pt/Co/AlOx trilayer. *Nat. Commun.*, **6**:8957, 2015.

[30] A. Fert, V. Cros, and J. Sampaio. Skyrmions on the track. *Nat. Nanotechnol.*, **8**(3): 152–156, 2013.

[31] M. Bode, M. Heide, K. von Bergmann, P. Ferriani, S. Heinze, G. Bihlmayer, A. Kubetzka, O. Pietzsch, S. Blügel, and R. Wiesendanger. Chiral magnetic order at surfaces driven by inversion asymmetry. *Nature*, **447**(7141):190–193, 2007.

[32] O. Boulle, G. Malinowski, and M. Kläui. Current-induced domain wall motion in nanoscale ferromagnetic elements. *Mater. Sci. Eng. R Rep.*, **72**(9):159–187, 2011.

[33] A. Thiaville, Y. Nakatani, J. Miltat, and Y. Suzuki. Micromagnetic understanding of current-driven domain wall motion in patterned nanowires. *EPL*, **69**(6):990–996, 2005.

[34] L. D. Landau and J. M. Lifshitz. On the theory of the dispersion of magnetic permeability in ferromagnetic bodies. *Phys. Z. Sowjetunion*, **8**(153):101–114, 1935.

[35] T. L. Gilbert. A phenomenological theory of damping in ferromagnetic materials. *IEEE Trans. Magn.*, **40**(6):3443–3449, 2004.

[36] D. Ralph and M. Stiles. Spin transfer torques. *J. Magn. Magn. Mater.*, **320**(7):1190–1216, 2008.

[37] X. Waintal and M. Viret. Current-induced distortion of a magnetic domain wall. *EPL*, **65** (3):427, 2004.

[38] M. Kläui, C. a. F. Vaz, J. a. C. Bland, W. Wernsdorfer, G. Faini, E. Cambril, and L. J. Heyderman. Domain wall motion induced by spin polarized currents in ferromagnetic ring structures. *Appl. Phys. Lett.*, **83**(1):105–107, 2003.

[39] J. Grollier, P. Boulenc, V. Cros, A. Hamzić, A. Vaurès, A. Fert, and G. Faini. Switching a spin valve back and forth by current-induced domain wall motion. *Appl. Phys. Lett.*, **83** (3):509–511, 2003.

[40] N. Vernier, D. A. Allwood, D. Atkinson, M. D. Cooke, and R. P. Cowburn. Domain wall propagation in magnetic nanowires by spin-polarized current injection. *EPL*, **65**(4): 526–532, 2004.

[41] A. Yamaguchi, T. Ono, S. Nasu, K. Miyake, K. Mibu, and T. Shinjo. Real-Space Observation of Current-Driven Domain Wall Motion in Submicron Magnetic Wires. *Phys. Rev. Lett.*, **92**(7):077205, 2004.

[42] C. K. Lim, T. Devolder, C. Chappert, J. Grollier, V. Cros, A. Vaurès, A. Fert, and G. Faini. Domain wall displacement induced by subnanosecond pulsed current. *Appl. Phys. Lett.*, **84**(15):2820–2822, 2004.

[43] S. Zhang and Z. Li. Roles of Nonequilibrium Conduction Electrons on the Magnetization Dynamics of Ferromagnets. *Phys. Rev. Lett.*, **93**(12):127204, 2004.

[44] Y. Tserkovnyak, H. J. Skadsem, A. Brataas, and G. E. W. Bauer. Current-induced magnetization dynamics in disordered itinerant ferromagnets. *Phys. Rev. B*, **74**(14), 2006.

[45] G. Tatara and H. Kohno. Theory of Current-Driven Domain Wall Motion: Spin Transfer versus Momentum Transfer. *Phys. Rev. Lett.*, **92**(8):086601, 2004.

[46] T. Shinjo, T. Okuno, R. Hassdorf, K. Shigeto, and T. Ono. Magnetic Vortex Core Observation in Circular Dots of Permalloy. *Science*, **289**(5481):930–932, 2000.

[47] S. Mühlbauer, B. Binz, F. Jonietz, C. Pfleiderer, A. Rosch, A. Neubauer, R. Georgii, and P. Böni. Skyrmion Lattice in a Chiral Magnet. *Science*, **323**(5916):915–919, 2009.

[48] P. Bruno. Geometrically Constrained Magnetic Wall. *Phys. Rev. Lett.*, **83**(12):2425–2428, 1999.

[49] O. Boulle, J. Kimling, P. Warnicke, M. Kläui, M., U. Rüdiger, U., G. Malinowski, H. J. M. Swagten, B. Koopmans, C. Ulysse, and G. Faini. Nonadiabatic Spin Transfer Torque in High Anisotropy Magnetic Nanowires with Narrow Domain Walls. *Phys. Rev. Lett.*, **101** (21):216601, 2008.

[50] J. Heinen, O. Boulle, K. Rousseau, G. Malinowski, M. Kläui, H. J. M. Swagten, B. Koopmans, C. Ulysse, and G. Faini. Current-induced domain wall motion in Co/Pt nanowires: Separating spin torque and Oersted-field effects. *Appl. Phys. Lett.*, **96**(20):202510, 2010.

[51] A. Mougin, M. Cormier, J. P. Adam, P. J. Metaxas, and J. Ferré. Domain wall mobility, stability and Walker breakdown in magnetic nanowires. *EPL*, **78**(5):57007, 2007.

[52] E. Martinez, L. Lopez-Diaz, O. Alejos, L. Torres, and C. Tristan. Thermal Effects on Domain Wall Depinning from a Single Notch. *Phys. Rev. Lett.*, **98**(26):267202, 2007.

[53] O. Boulle, L. D. Buda-Prejbeanu, M. Miron, and G. Gaudin. Current induced domain wall dynamics in the presence of a transverse magnetic field in out-of-plane magnetized materials. *J. Appl. Phys.*, **112**(5):053901, 2012.

[54] B. Dieny and M. Chshiev. Perpendicular magnetic anisotropy at transition metal/oxide interfaces and applications. *Rev. Mod. Phys.*, **89**(2):025008, 2017.

[55] R. Shimabukuro, K. Nakamura, T. Akiyama, and T. Ito. Electric field effects on magnetocrystalline anisotropy in ferromagnetic Fe monolayers. *Physica E: Low Dimens. Syst. Nanostruct.*, **42**(4):1014–1017, 2010.

[56] D. Wu, Z. Zhang, L. Li, Z. Zhang, H. B. Zhao, J. Wang, B. Ma, and Q. Y. Jin. Perpendicular magnetic anisotropy and magnetization dynamics in oxidized CoFeAl films. *Sci. Rep.*, **5**: 12352, 2015.

[57] S. Monso, B. Rodmacq, S. Auffret, G. Casali, F. Fettar, B. Gilles, B. Dieny, and P. Boyer. Crossover from in-plane to perpendicular anisotropy in Pt/CoFe/AlOx sandwiches as a function of Al oxidation: A very accurate control of the oxidation of tunnel barriers. *Appl. Phys. Lett.*, **80**(22):4157–4159, 2002.

[58] A. Manchon, C. Ducruet, L. Lombard, S. Auffret, B. Rodmacq, B. Dieny, S. Pizzini, J. Vogel, V. Uhlíř, M. Hochstrasser, and G. Panaccione. Analysis of oxygen induced anisotropy crossover in Pt/Co/MOx trilayers. *J. Appl. Phys.*, **104**(4):043914, 2008.

[59] L. E. Nistor, B. Rodmacq, S. Auffret, and B. Dieny. Pt/Co/oxide and oxide/Co/Pt electrodes for perpendicular magnetic tunnel junctions. *Appl. Phys. Lett.*, **94**(1):012512, 2009.

[60] S. Ikeda, K. Miura, H. Yamamoto, K. Mizunuma, H. D. Gan, M. Endo, S. Kanai, J. Hayakawa, F. Matsukura, and H. Ohno. A perpendicular-anisotropy CoFeB–MgO magnetic tunnel junction. *Nat. Mater.*, **9**(9):2804, 2010.

[61] S. Mangin, D. Ravelosona, J. A. Katine, M. J. Carey, B. D. Terris, and E. E. Fullerton. Current-induced magnetization reversal in nanopillars with perpendicular anisotropy. *Nat. Mater.*, **5**(3):210–215, 2006.

[62] T. Miyazaki and N. Tezuka. Giant magnetic tunneling effect in Fe/Al2o3/Fe junction. *J. Magn. Magn. Mater.*, **139**(3):L231–L234, 1995.

[63] J. S. Moodera, L. R. Kinder, T. M. Wong, and R. Meservey. Large Magnetoresistance at Room Temperature in Ferromagnetic Thin Film Tunnel Junctions. *Phys. Rev. Lett.*, **74** (16):3273–3276, 1995.

[64] H. Itoh and J. Inoue. Theory of Tunnel Magnetoresistance. *J. Magn. Soc. Jpn.*, **30**(1): 1–37, 2006.

[65] L. Liu, C.-F. Pai, Y. Li, H. W. Tseng, D. C. Ralph, and R. A. Buhrman. Spin-torque switching with the giant spin Hall effect of tantalum. *Science*, **336**(6081):555–558, 2012.

[66] S. Ikeda, J. Hayakawa, Y. Ashizawa, Y. M. Lee, K. Miura, H. Hasegawa, M. Tsunoda, F. Matsukura, and H. Ohno. Tunnel magnetoresistance of 604% at 300k by suppression of Ta diffusion in CoFeBMgOCoFeB pseudo-spin-valves annealed at high temperature. *Appl. Phys. Lett.*, **93**(8):082508, 2008.

[67] N. Miyakawa, D. C. Worledge, and K. Kita. Impact of Ta Diffusion on the Perpendicular Magnetic Anisotropy of Ta/CoFeB/MgO. *IEEE Magn. Lett.*, **4**:1000104–1000104, 2013.

[68] K. Watanabe, S. Fukami, H. Sato, S. Ikeda, F. Matsukura, and H. Ohno. Annealing temperature dependence of magnetic properties of CoFeB/MgO stacks on different buffer layers. *Jpn. J. Appl. Phys.*, **56**(8):0802B2, 2017.

[69] I. M. Miron, T. Moore, H. Szambolics, L. D. Buda-Prejbeanu, S. Auffret, B. Rodmacq, S. Pizzini, J. Vogel, M. Bonfim, A. Schuhl, and G. Gaudin. Fast current-induced domain-wall motion controlled by the Rashba effect. *Nat. Mater.*, **10**(6):419–423, 2011.

[70] Y. A. Bychkov and E. I. Rashba. Oscillatory effects and the magnetic susceptibility of carriers in inversion layers. *J. Phys. C: Solid State Phys.*, **17**(33):6039, 1984.

[71] V. M. Edelstein. Spin polarization of conduction electrons induced by electric current in two-dimensional asymmetric electron systems. *Solid State Commun.*, **73**(3):233–235, 1990.

[72] S. D. Ganichev, E. L. Ivchenko, V. V. Bel'kov, S. A. Tarasenko, M. Sollinger, D. Weiss, W. Wegscheider, and W. Prettl. Spin-galvanic effect. *Nature*, **417**(6885):153–156, 2002.

[73] P. Gambardella and I. M. Miron. Current-induced spin-orbit torques. *Philos. Trans. Royal Soc. A*, **369**(1948):3175–3197, 2011.

[74] M. I. D'Yakonov and V. I. Perel'. Spin Orientation of Electrons Associated with the Interband Absorption of Light in Semiconductors. *JETP*, **33**(5):1053, 1971.

[75] J. E. Hirsch. Spin hall effect. *Phys. Rev. Lett.*, **83**(9):1834, 1999.

[76] J. Sinova, S. O. Valenzuela, J. Wunderlich, C. Back, and T. Jungwirth. Spin Hall effects. *Rev. Mod. Phys.*, **87**(4):1213–1260, 2015.

[77] I. M. Miron, K. Garello, G. Gaudin, P.-J. Zermatten, M. V. Costache, S. Auffret, S. Bandiera, B. Rodmacq, A. Schuhl, and P. Gambardella. Perpendicular switching of a single ferromagnetic layer induced by in-plane current injection. *Nature*, **476**(7359):189–193, 2011.

[78] T. A. Moore, I. M. Miron, G. Gaudin, G. Serret, S. Auffret, B. Rodmacq, A. Schuhl, S. Pizzini, J. Vogel, and M. Bonfim. Erratum: "High domain wall velocities induced by current in ultrathin Pt/Co/AlOx wires with perpendicular magnetic anisotropy" [Appl. Phys. Lett. 93, 262504 (2008)]. *Appl. Phys. Lett.*, **95**(17):179902, 2009.

[79] I. M. Miron, G. Gaudin, S. Auffret, B. Rodmacq, A. Schuhl, S. Pizzini, J. Vogel, and P. Gambardella. Current-driven spin torque induced by the Rashba effect in a ferromagnetic metal layer. *Nat. Mater.*, **9**(3):230–234, 2010.

[80] T. D. Skinner, K. Olejník, L. K. Cunningham, H. Kurebayashi, R. P. Campion, B. L. Gallagher, T. Jungwirth, and A. J. Ferguson. Complementary spin-Hall and inverse spin-galvanic effect torques in a ferromagnet/semiconductor bilayer. *Nat. Commun.*, **6**:6730, 2015.

[81] R. Lo Conte. Magnetic nanostructures with structural inversion asymmetry. Dissertation, Johannes Gutenberg–Universität Mainz, Mainz, 2015. URL: `http://nbn-resolving.de/urn:nbn:de:hebis:77-diss-1000002289`.

[82] H. Li, H. Gao, L. P. Zârbo, K. Výborný, X. Wang, I. Garate, F. Doan, A. Čejchan, J. Sinova, T. Jungwirth, and A. Manchon. Intraband and interband spin-orbit torques in noncentrosymmetric ferromagnets. *Phys. Rev. B*, **91**(13):134402, 2015.

[83] H. Kurebayashi, J. Sinova, D. Fang, A. C. Irvine, T. D. Skinner, J. Wunderlich, V. Novák, R. P. Campion, B. L. Gallagher, E. K. Vehstedt, L. P. Zârbo, K. Výborný, A. J. Ferguson, and T. Jungwirth. An antidamping spin–orbit torque originating from the Berry curvature. *Nat. Nanotechnol.*, **9**(3):211–217, 2014.

[84] M. V. Berry and F. R. S. Quantal phase factors accompanying adiabatic changes. *Proc. R. Soc. Lond. A*, **392**(1802):45–57, 1984.

[85] N. Nagaosa, J. Sinova, S. Onoda, A. H. MacDonald, and N. P. Ong. Anomalous Hall effect. *Rev. Mod. Phys.*, **82**(2):1539–1592, 2010.

[86] F. Freimuth, S. Blügel, and Y. Mokrousov. Spin-orbit torques in Co/Pt(111) and Mn/W(001) magnetic bilayers from first principles. *Phys. Rev. B*, **90**(17):174423, 2014.

[87] C. O. Avci. Current-induced effects in ferromagnetic heterostructures due to spin-orbit coupling. Doctoral Thesis, ETH ZURICH, 2015. URL: `https://www.research-collection.ethz.ch/handle/20.500.11850/111775`.

[88] Y. K. Kato, R. C. Myers, A. C. Gossard, and D. D. Awschalom. Observation of the Spin Hall Effect in Semiconductors. *Science*, **306**(5703):1910–1913, 2004.

[89] J. Wunderlich, B. Kaestner, J. Sinova, and T. Jungwirth. Experimental Observation of the Spin-Hall Effect in a Two-Dimensional Spin-Orbit Coupled Semiconductor System. *Phys. Rev. Lett.*, **94**(4):047204, 2005.

[90] S. O. Valenzuela and M. Tinkham. Direct electronic measurement of the spin Hall effect. *Nature*, **442**(7099):04937, 2006.

[91] T. Tanaka, H. Kontani, M. Naito, T. Naito, D. S. Hirashima, K. Yamada, and J. Inoue. Intrinsic spin Hall effect and orbital Hall effect in $4d$ and $5d$ transition metals. *Phys. Rev. B*, **77**(16):165117, 2008.

[92] P. Braganca, J. Katine, N. Emley, D. Mauri, J. Childress, P. Rice, E. Delenia, D. Ralph, and R. Buhrman. A Three-Terminal Approach to Developing Spin-Torque Written Magnetic Random Access Memory Cells. *IEEE T. on Nanotechnol.*, **8**(2):190–195, 2009.

[93] S. Fukami, M. Yamanouchi, S. Ikeda, and H. Ohno. Domain Wall Motion Device for Nonvolatile Memory and Logic - Size Dependence of Device Properties. *IEEE Trans. Magn.*, **50**(11):1–6, 2014.

[94] S. Zhang, P. M. Levy, and A. Fert. Mechanisms of Spin-Polarized Current-Driven Magnetization Switching. *Phys. Rev. Lett.*, **88**(23), 2002.

[95] A. Shpiro, P. M. Levy, and S. Zhang. Self-consistent treatment of nonequilibrium spin torques in magnetic multilayers. *Phys. Rev. B*, **67**(10), 2003.

[96] K. Xia, P. J. Kelly, G. E. W. Bauer, A. Brataas, and I. Turek. Spin torques in ferromagnetic/normal-metal structures. *Phys. Rev. B*, **65**(22), 2002.

[97] O. Mosendz, J. E. Pearson, F. Y. Fradin, G. E. W. Bauer, S. D. Bader, and A. Hoffmann. Quantifying Spin Hall Angles from Spin Pumping: Experiments and Theory. *Phys. Rev. Lett.*, **104**(4), 2010.

[98] I. M. Miron, P.-J. Zermatten, G. Gaudin, S. Auffret, B. Rodmacq, and A. Schuhl. Domain Wall Spin Torquemeter. *Phys. Rev. Lett.*, **102**(13):137202, 2009.

[99] A. Manchon. Spin Hall effect versus Rashba torque: a Diffusive Approach. *arXiv:1204.4869 [cond-mat]*,

[100] A. Brataas, A. D. Kent, and H. Ohno. Current-induced torques in magnetic materials. *Nat. Mater.*, **11**(5):372–381, 2012.

[101] K. Garello, I. M. Miron, C. O. Avci, F. Freimuth, Y. Mokrousov, S. Blügel, S. Auffret, O. Boulle, G. Gaudin, and P. Gambardella. Symmetry and magnitude of spin-orbit torques in ferromagnetic heterostructures. *Nat. Nanotechnol.*, **8**(8):587–593, 2013.

[102] Y. Ou, C.-F. Pai, S. Shi, D. C. Ralph, and R. A. Buhrman. Origin of fieldlike spin-orbit torques in heavy metal/ferromagnet/oxide thin film heterostructures. *Phys. Rev. B*, **94** (14):140414, 2016.

[103] J. Kim, J. Sinha, M. Hayashi, M. Yamanouchi, S. Fukami, T. Suzuki, S. Mitani, and H. Ohno. Layer thickness dependence of the current-induced effective field vector in Ta|CoFeB|MgO. *Nat. Mater.*, **12**(3):240–245, 2013.

[104] X. Wang and A. Manchon. Diffusive Spin Dynamics in Ferromagnetic Thin Films with a Rashba Interaction. *Phys. Rev. Lett.*, **108**(11):117201, 2012.

[105] P. P. J. Haazen, E. Murè, J. H. Franken, R. Lavrijsen, H. J. M. Swagten, and B. Koopmans. Domain wall depinning governed by the spin Hall effect. *Nat. Mater.*, **12**(4):299–303, 2013.

[106] P. M. Haney, H.-W. Lee, K.-J. Lee, A. Manchon, and M. D. Stiles. Current-induced torques and interfacial spin-orbit coupling. *Phys. Rev. B*, **88**(21), 2013.

[107] P. M. Haney. Current induced torques and interfacial spin-orbit coupling: semiclassical modeling. *Phys. Rev. B*, **87**:174411, 2013.

[108] U. H. Pi, K. Won Kim, J. Y. Bae, S. C. Lee, Y. J. Cho, K. S. Kim, and S. Seo. Tilting of the spin orientation induced by Rashba effect in ferromagnetic metal layer. *Appl. Phys. Lett.*, **97**(16):162507, 2010.

[109] C. O. Avci, K. Garello, C. Nistor, S. Godey, B. Ballesteros, A. Mugarza, A. Barla, M. Valvidares, E. Pellegrin, A. Ghosh, I. M. Miron, O. Boulle, S. Auffret, G. Gaudin, and P. Gambardella. Fieldlike and antidamping spin-orbit torques in as-grown and annealed Ta/CoFeB/MgO layers. *Phys. Rev. B*, **89**(21):214419, 2014.

[110] M. Hayashi, J. Kim, M. Yamanouchi, and H. Ohno. Quantitative characterization of the spin-orbit torque using harmonic Hall voltage measurements. *Phys. Rev. B*, **89**(14): 144425, 2014.

[111] X. Qiu, P. Deorani, K. Narayanapillai, K.-S. Lee, K.-J. Lee, H.-W. Lee, and H. Yang. Angular and temperature dependence of current induced spin-orbit effective fields in Ta/CoFeB/MgO nanowires. *Sci. Rep.*, **4**:4491, 2014.

[112] Y. Fan, P. Upadhyaya, X. Kou, M. Lang, S. Takei, Z. Wang, J. Tang, L. He, L.-T. Chang, M. Montazeri, G. Yu, W. Jiang, T. Nie, R. N. Schwartz, Y. Tserkovnyak, and K. L. Wang. Magnetization switching through giant spin–orbit torque in a magnetically doped topological insulator heterostructure. *Nat. Mater.*, **13**(7):699–704, 2014.

[113] Y. Chen, H. Celik, T. Wang, H. Kannan, I. N. Krivorotov, and J. Q. Xiao. Quantifying angular dependence of spin-orbit torques in Ta/CoFeB/MgO trilayers with perpendicular magnetic anisotropy. *Phys. Rev. B*, **95**(14):144405, 2017.

[114] K.-S. Lee, D. Go, A. Manchon, P. M. Haney, M. D. Stiles, H.-W. Lee, and K.-J. Lee. Angular dependence of spin-orbit spin-transfer torques. *Phys. Rev. B*, **91**(14), 2015.

[115] C. Ortiz Pauyac, X. Wang, M. Chshiev, and A. Manchon. Angular dependence and symmetry of Rashba spin torque in ferromagnetic heterostructures. *Appl. Phys. Lett.*, **102** (25):252403, 2013.

[116] A. Hrabec, N. A. Porter, A. Wells, M. J. Benitez, G. Burnell, S. McVitie, D. McGrouther, T. A. Moore, and C. H. Marrows. Measuring and tailoring the Dzyaloshinskii-Moriya interaction in perpendicularly magnetized thin films. *Phys. Rev. B*, **90**(2):020402, 2014.

[117] O. Boulle, L. D. Buda-Prejbeanu, E. Jué, I. M. Miron, and G. Gaudin. Current induced domain wall dynamics in the presence of spin orbit torques. *J. Appl. Phys.*, **115**(17): 17D502, 2014.

[118] E. H. Hall. On a New Action of the Magnet on Electric Currents. *Am. J. Math.*, **2**(3): 287–292, 1879.

[119] R. Karplus and J. M. Luttinger. Hall Effect in Ferromagnetics. *Phys. Rev.*, **95**(5): 1154–1160, 1954.

[120] M. Onoda and N. Nagaosa. Topological Nature of Anomalous Hall Effect in Ferromagnets. *J. Phys. Soc. Jpn.*, **71**(1):19–22, 2002.

[121] N. F. Mott and B. A. The scattering of fast electrons by atomic nuclei. *Proc. R. Soc. Lond. A*, **124**(794):425–442, 1929.

[122] L. Berger. Side-jump mechanism for the Hall effect of ferromagnets. *Phys. Rev. B*, **2**(11): 4559, 1970.

[123] M. Walter. The tunnel magneto-Seebeck effect in magnetic tunnel junctions. Dissertation, Göttingen, 2013. URL: `https://ediss.uni-goettingen.de/handle/11858/00-1735-0000-0022-5E09-E`.

[124] A. Lamperti, E. Cianci, O. Salicio, L. Lamagna, S. Spiga, and M. Fanciulli. Thermal stability of high-kappa oxides on SiO2/Si or SixNy/SiO2/Si for charge-trapping nonvolatile memories. *Surf. Interface Anal.*, **45**(1):390–393, 2013.

[125] T. N. Zacke. Spin-transfer torque in high anisotropy nanostructures. Diploma thesis, Johannes Gutenberg–Universität Mainz, Mainz, Germany, 2013.

[126] K. Shigeto, T. Shinjo, and T. Ono. Injection of a magnetic domain wall into a submicron magnetic wire. *Appl. Phys. Lett.*, **75**(18):2815–2817, 1999.

[127] R. P. Cowburn, D. A. Allwood, G. Xiong, and M. D. Cooke. Domain wall injection and propagation in planar Permalloy nanowires. *J. Appl. Phys.*, **91**(10):6949–6951, 2002.

[128] PMMA resist. URL: `http://www.allresist.de/produkte/produkte-e-beam-resists/`.

[129] C. O. Avci, K. Garello, A. Ghosh, M. Gabureac, S. F. Alvarado, and P. Gambardella. Unidirectional spin Hall magnetoresistance in ferromagnet/normal metal bilayers. *Nat. Phys.*, **11**(7):570–575, 2015.

[130] T. Schulz, K. Lee, B. Krüger, R. Lo Conte, G. V. Karnad, K. Garcia, L. Vila, B. Ocker, D. Ravelosona, and M. Kläui. Effective field analysis using the full angular spin-orbit torque magnetometry dependence. *Phys. Rev. B*, **95**(22), 2017.

[131] H.-R. Lee, K. Lee, J. Cho, Y.-H. Choi, C.-Y. You, M.-H. Jung, F. Bonell, Y. Shiota, S. Miwa, and Y. Suzuki. Spin-orbit torque in a bulk perpendicular magnetic anisotropy Pd/FePd/MgO system. *Sci. Rep.*, **4**:6548, 2014.

[132] T. Schulz, O. Alejos, E. Martinez, K. M. D. Hals, K. Garcia, L. Vila, K. Lee, R. Lo Conte, G. V. Karnad, S. Moretti, B. Ocker, D. Ravelosona, A. Brataas, and M. Kläui. Spin-orbit torques for current parallel and perpendicular to a domain wall. *Appl. Phys. Lett.*, **107** (12):122405, 2015.

[133] J. Heinen, D. Hinzke, O. Boulle, G. Malinowski, H. J. M. Swagten, B. Koopmans, C. Ulysse, G. Faini, B. Ocker, J. Wrona, and M. Kläui. Determination of the spin torque non-adiabaticity in perpendicularly magnetized nanowires. *J. Phys. Condens. Matter*, **24** (2):024220, 2012.

[134] O. Boulle, S. Rohart, L. D. Buda-Prejbeanu, E. Jué, I. M. Miron, S. Pizzini, J. Vogel, G. Gaudin, and A. Thiaville. Domain Wall Tilting in the Presence of the Dzyaloshinskii-Moriya Interaction in Out-of-Plane Magnetized Magnetic Nanotracks. *Phys. Rev. Lett.*,

111(21), 2013.

[135] G. V. Karnad, E. Martinez, M. Voto, T. Schulz, B. Ocker, D. Ravelosona, and M. Kläui. Study of energetics of 360° domain walls through annihilation. *arXiv:1806.00294 [cond-mat]*,

[136] C. Safeer. Study of domain wall dynamics in the presence of large spin-orbit coupling: chiral damping and magnetic origami. Dissertation, Universite Grenoble Alpes, Grenoble, 2015. URL: `https://tel.archives-ouvertes.fr/tel-01274057/document`.

[137] C. K. Safeer, E. Jué, A. Lopez, L. Buda-Prejbeanu, S. Auffret, S. Pizzini, O. Boulle, I. M. Miron, and G. Gaudin. Spin–orbit torque magnetization switching controlled by geometry. *Nat. Nanotechnol.*, **11**(2):143–146, 2016.

[138] J.-P. Tetienne, T. Hingant, J.-V. Kim, L. H. Diez, J.-P. Adam, K. Garcia, J.-F. Roch, S. Rohart, A. Thiaville, D. Ravelosona, and V. Jacques. Nanoscale imaging and control of domain-wall hopping with a nitrogen-vacancy center microscope. *Science*, **344**(6190): 1366–1369, 2014.

[139] K. M. D. Hals and A. Brataas. Phenomenology of current-induced spin-orbit torques. *Phys. Rev. B*, **88**(8):085423, 2013.

[140] A. V. Khvalkovskiy, V. Cros, D. Apalkov, V. Nikitin, M. Krounbi, K. A. Zvezdin, A. Anane, J. Grollier, and A. Fert. Matching domain-wall configuration and spin-orbit torques for efficient domain-wall motion. *Phys. Rev. B*, **87**(2):020402(R), 2013.